Graphene Oxide / Titanium Dioxide Membranes

Chemical Engineering

Master Thesis, June 2016

Morten Lykke Krogh Pedersen Thomas Reinhald Jensen

Frontpage picture: SEM image of GO/TiO_2 membrane.

Graphene Oxide/Titanium Dioxide Membranes

Development and characterization

K10 2016

Morten Lykke Krogh Pedersen

Thomas Reinhald Jensen

Supervisor: Morten Enggrob Simonsen

Aalborg Universitet Esbjerg

2. September 2015 - 9. June 2016

Abstract

During recent years, graphene has been studied intensively because of its unique characteristics, making it usable for a variety of applications. In order to produce graphene, it is first necessary to oxidize graphite to graphene oxide and then reduce it to graphene. Tests have shown that graphene oxide could possibly be used as a membrane material for water treatment, as its oxygen-rich functional groups provide high hydrophilicity, while the graphene structure ensures excellent selectivity. A major limitation in membrane filtration is the fouling phenomena, which is why TiO_2 could be of interest in membrane usage. TiO_2 is used to clean surfaces via its photocatalytic properties.

The purpose of this project was therefore to investigate graphene oxide as a membrane material and incorporate TiO_2. Different graphene oxide syntheses were tested and different GO/TiO_2 ratios were also tested. The thermal treatment process for reducing graphene oxide was also tested in order to find optimal reduction time and temperature for stable membranes. The thermal reduction was evaluated using X-ray diffraction (XRD), differential scanning calorimetry (DSC), thermogravimetric analysis (TGA) and Fourier transform infrared spectroscopy (FT-IR). The surface characteristics were examined before and after UV-C irradiation, in order to see if the TiO_2 provided significant changes. Surface characteristics were analyzed using drop shape analysis (DSA), zeta potential measurements and FT-IR. The vapor permeance of the membranes produced was tested with water, ethanol and hexane. Scanning electron microscopy (SEM) was also done in order to see any potential membrane damage as a result of UV-C irradiation. The membrane surface characteristics and permeance were compared to that of two commercial membranes; Alfa Laval NF99HF and NFT50.

By comparing the different syntheses via XRD and FT-IR, it was concluded that the Tour's method was best suited for further experiments. From the reduction experiments done, it was found that reduction at $140°C$ for one hour produced the most stable and hydrophilic membranes. The optimal GO/TiO_2 ratio was found to be in the range of 15:1 - 30:1. The TiO_2 added to the graphene oxide membranes was found to significantly enhance hydrophilicity and anti-fouling properties, caused by the formation of hydroxyl groups at the surface. SEM tests were inconclusive as to whether the membrane is damaged by the photocatalytic activity of TiO_2. The water vapor permeance was found to be close to unimpeded and at least 55% higher than the commercial membranes tested.

Preface

This masters thesis is the product of a project made by two chemical engineering students on their 10th semester at Aalborg Universitet Esbjerg.

The purpose of this project is to investigate graphene oxide as a potential membrane material for water treatment. These membranes were modified by adding TiO_2 in hopes of creating membranes with anti-fouling properties. The membranes were characterized using the laboratories in Aalborg University Esbjerg and Aalborg University.

Source references are marked with [ ], optionally with indication of pagenumbers (fx [3, pagenumber] with reference to source number 3). Sources are located in the bibliography at the back of the report. For websources the date of visit is noted in the bibliography.

The figures and tables in the report are denoted with two numbers (fx Fig.1.1), the first number indicates the chapter it belongs to, and the second number is figure number in the chapter. Figures that aren't selfproduced are marked with [ ], just like the sources.

Despite many struggles and frustrations developing these membranes, we are excited about the results and knowledge gained from our research. We consider the results worthy of being published and we intend to formulate an article based on this project. It is our hope that our thesis will be used as a source for further research.

June - 2016
Morten Lykke Krogh Pedersen
Thomas Reinhald Jensen

Contents

1 Introduction

One of the big challenges in urban societies is to secure access to safe and clean water for people, along with treating the wastewater produced without threatening the water resources and the environment. Membrane technology for water treatment has shown great potential as a solution to solve this problem, researching new materials for this use is therefore of upmost importance. In the quest to develop new materials many options have been sought out, one of these new materials is graphene.

Graphene has been an interesting material to study in the recent years, this is because of its unique characteristics which can be used for a variety of applications. In order to synthesize graphene, a common stepping stone is creating graphene oxide and reducing it. Instead of using graphene oxide as a stepping stone to graphene, it is of interest to investigate possible applications for graphene oxide, because it has some unique characteristics which graphene does not.
The oxidation of graphite to graphene oxide creates a material with excellent selectivity and high hydrophilicity. These characteristics have made graphene oxide an interesting material to study for use as a membrane, where it could be of use in water treatment as a high-flux selective membrane.

One of the major limitations of membrane usage is the fouling phenomena, where the permeate being filtered causes changes on the membrane surface and decreases flux. It has therefore been of great interest to test additives like TiO_2 in membranes in order to reduce fouling. TiO_2 is used in a variety of applications for its ability to clean surfaces with its photocatalytic properties. This ability to clean surfaces could be significant in terms of reducing fouling in membranes. In this project, graphene oxide and TiO_2 were synthesized and membranes with varying TiO_2 content were produced. The membranes produced were characterized and irradiated with UV-light in order to test whether this changed the surface characteristics of the membranes.

The project will start by describing the synthesis of graphene oxide and the material itself. This is followed by a section describing membranes, in order to gain a general understanding of membranes and relate it to graphene oxide. The final theory section describes TiO_2 and is followed by the project thesis. The characterization methods and experiment design will be described, followed by a presentation of the results.

2 Graphene Oxide

This chapter will describe graphite and describe how it is synthesized into graphene oxide, and describe the possibility of using graphene oxide as a membrane material. The development in methods for producing graphene oxide will be described and compared, the effects of reducing graphene oxide is shown. Graphene oxide is commonly used a precursor for creating graphene, which is regarded as a super star in carbon nanomaterial science. Research in graphene oxide has revealed promising qualities for use as a membrane material. These promising qualities is of interest for use in water filtration.

2.1 Graphite

Graphite is a crystalline form of carbon. Crystalline forms of carbon at ambient conditions are primarily as graphite or diamond, the structure of these crystalline forms are vital to their properties. The carbon atoms in the diamond structure are in sp^3 configuration with sigma bonds, the bonds are arranged in a tetrahedral lattice with all covalent bond lengths of 1,54Å. This rigid structure is the reason diamond is the hardest of all natural materials. Graphite is a very soft material compared to diamond, its structure is found in layers of sp^2 hybridized carbon atoms in planar hexagonal rings, these layers are 3,35Å apart and the carbon-carbon covalent sigma-type bond length in the layer is 1,42Å. The remaining p orbitals in graphite are delocalized π-bonds that extend perpendicular to the planes which causes weak van der Wahls attractions between the planes. The structural difference can be see on figure 2.1 [1]

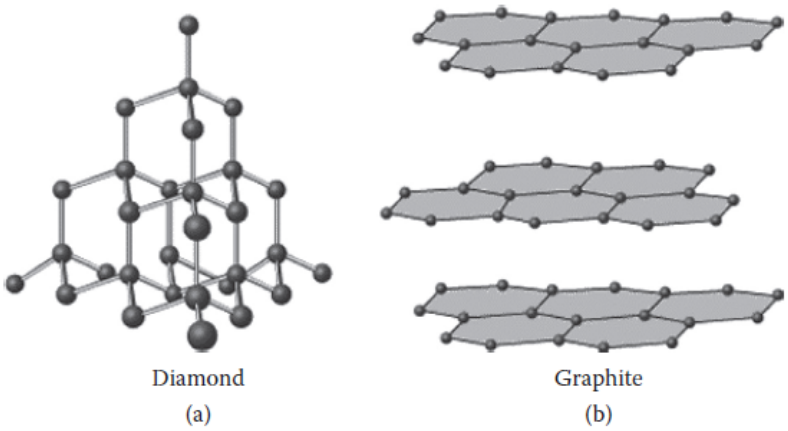

Figure 2.1: *Structural comparison between diamond (a) and graphite (b), both crystalline structures are formed with carbon, but they differ in structure.*[1]

Both crystalline forms of carbon have interesting properties, which originates from the bonding structure, this report will focus on graphite and how it can be used for producing graphene oxide.

2.2 Graphene Oxide

The natural form of graphite contains localized material defects in the π-structure, these material defects makes the material ideal for chemical modifications through chemical reactions. One of these modifications are oxidation, the oxidized form of graphite is called graphene oxide. When oxidizing graphite the basal planes will obtain hydroxyl and epoxide groups, the edges will obtain carbonyl and carboxyl groups see figure 2.2. Graphene oxide is easily dispersed in water or other polar solvents, where it forms a colloid suspension. [2] In order to use it for membranes in water treatment it is important to limit the dispersability in water, this can be done by reducing the graphene oxide. When reduced the graphene oxide loses some of its oxygen-containing functional groups, making the material less hydrophilic and insoluble in water. [3]

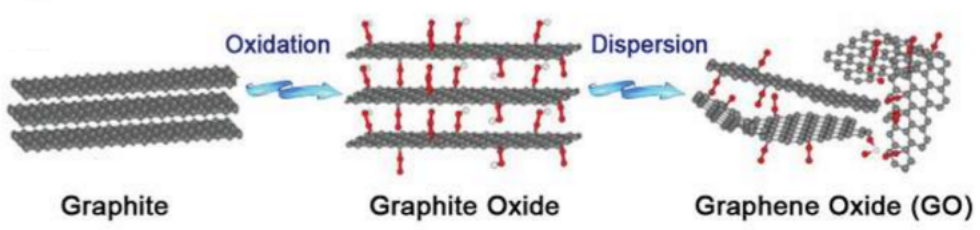

Figure 2.2: *Illustration showing graphite oxidized to graphene oxide (GO).*[4]

In order to oxidize graphite, a suitable oxidizing agent needs to be selected, the following subsections will cover the history and developments in methods

for creating graphene oxide, with emphasis on Tour's method since it was used for creating the graphene oxide used for the experimental part of this thesis.

2.2.1 Brodie's and Staudenmaiers method

Graphene oxide was discovered in 1859, when the British chemist by the name Benjamin C. Brodie chemically treated graphite in fuming nitric acid with a potassium chlorate solution. Brodie named the compound he had created graphitic acid or graphite oxide, however after graphene research emerged in 2004, it is known as graphene oxide.

Brodie's method was improved upon by Staudenmaier in 1898, where concentrated sulphuric acid and additional amount of potassium chlorate solution was added. These changes led to a more oxidized product, but the method was hazardous and very time consuming (adding the potassium chlorate lasted about a week, and the chlorine dioxide produced was required to be removed with an inert gas), leaving development in the oxidation process worthwhile to investigate further. [4]

2.2.2 Hummers and Tours method

In 1958 a new method for oxidizing graphite was developed by William S. Hummers and Richard E. Offeman, this method is known as Hummer's method. Their recipe was based on a water free mixture of concentrated sulfuric acid, sodium nitrate and potassium permanganate. Hummer's method has been a key point of interest when creating graphene oxide, because large quantities can be made fairly easy. Modifications to Hummer's method has been made, both to reduce the time it takes and to make it more environment friendly. [4]

With the discovery of graphene in 2004, graphene oxide was once again in the center of carbon nanomaterial research. In 2010 a modification to Hummer's method was developed by Tour's group known as Tour's method. This new method eliminated the use of sodium nitrate, increased the amount of potassium permanganate and added phosphoric acid. They reported a higher degree of oxidation and one of the biggest advantages of this method is the elimination of sodium nitrate, which stops the generation of toxic gases like NO_2 and N_2O_4, making the method more environmental friendly.

The addition of phosphoric acid in Tour's method is believed to offer more intact sp^2 carbon domains in the basal planes of the final product. This is done by protecting the basal planes from over oxidation, after the initial oxidation vicinal diols are formed, if oxidized further these vicinal diols will result in holes in the basal plane. With the presence of phosphoric acid, the vicinal diols instead form a cyclic structure, protecting it from further oxidation, figure 2.3 shows a possible explanation for this effect. [4]

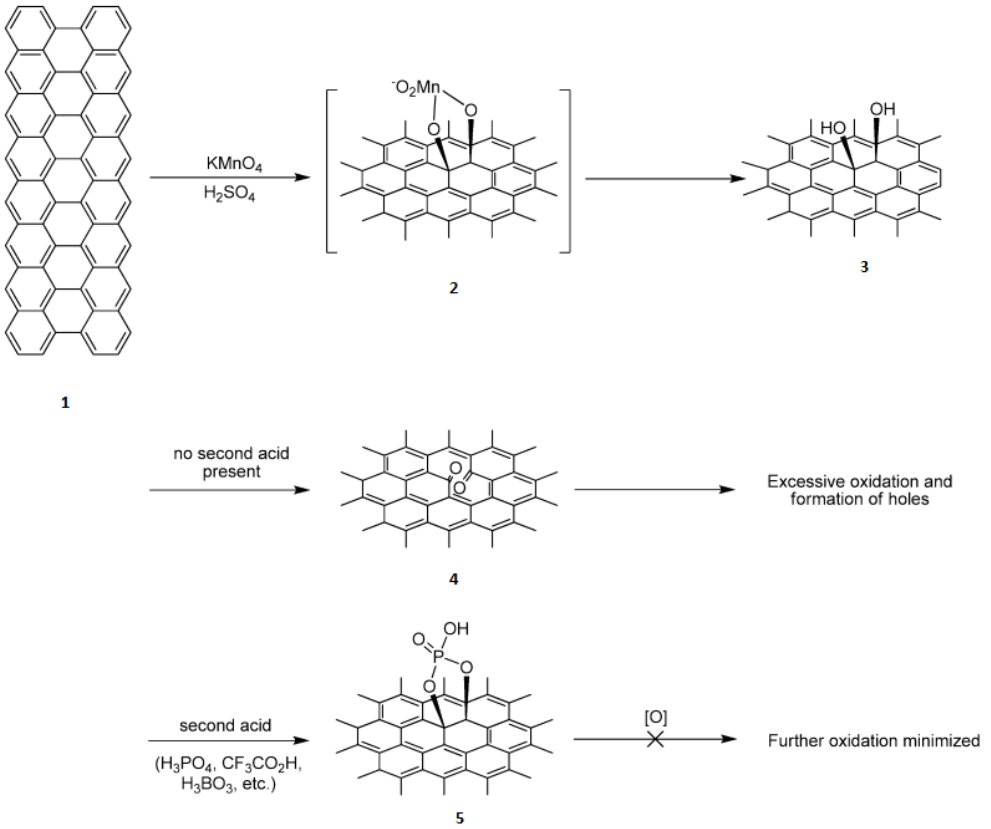

Figure 2.3: *Proposed mechanism showing the effects of adding phosphoric acid, preventing the over oxidation of the sp^2 carbon network once they have formed the vicinal diols. After the manganate ester formation (2), the vicinal diols (3) formed will cleave at the carbon-carbon bond, resulting in a dione (4) and a new hole in the structure, leading to destructive oxidation of the structure causing more defects in the basal planes. With the addition of H_3PO_4 the diols (3) will be protected by forming a cyclic structure (5) effectively preventing overoxidation of the diones.*[5]

Tour's method also produce a higher yield, by leaving a smaller amount of hydrophobic carbon material behind after the initial reaction. A comparison of the yield from the original Hummer, the modified Hummer and the improved Hummer (Tour) can be seen on figure 2.4.

Two different combinations of oxidizing reagents has been used for these methods to produce graphene oxide, the first one being potassium chlorate and nitric acid and the second one with potassium permanganate and sulfuric acid. The Brodie and Staudemaier method both used the first combination, back then these chemicals were believed to be the strongest oxidizers available. The second combination uses the permanganate ion as oxidizing reagent. The permanganate ion can only be activitated in acidic environment, where the potassium permanganate in the presence of a strong acid forms dimanganese heptoxide (Mn_2O_7), which is a more reactive oxidizer.[4]

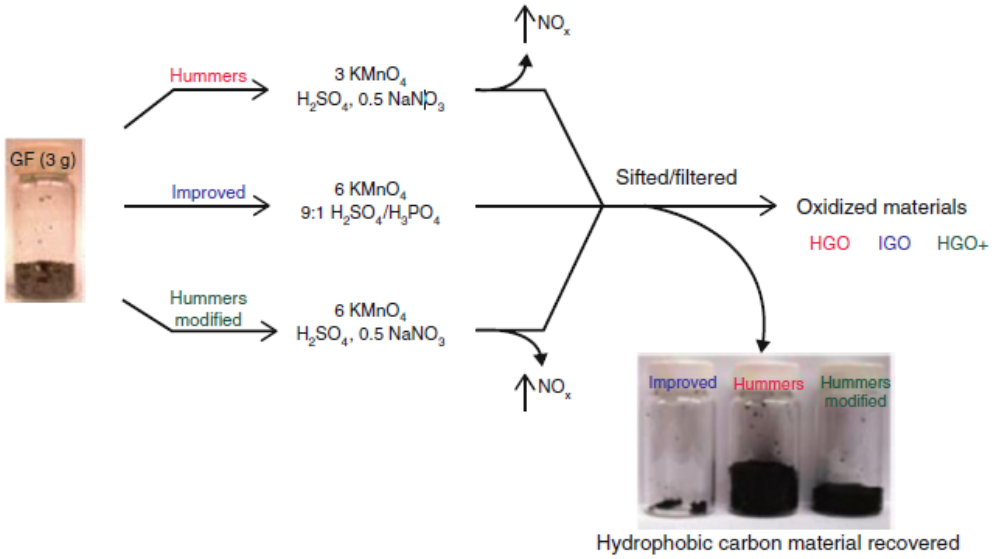

Figure 2.4: *Comparison of methods starting out with graphite flakes (GF). Under-oxidized hydrophobic carbon material recovered during purification is shown. The increased effiency of the improved method (Tour) is indicated by the small amount of hydrophobic carbon material recovered.*[6]

2.2.3 Green approach method

The use of $KMnO_4$ as oxidant can cause environmental problems with heavy metal pollution from Mn^2+ ions and also the explosive risks associated with dimanganese heptoxide. These issues has recently lead to the development of a new approach for preparing graphene oxide using K_2FeO_4 as oxidant. This new method also has a shorter reaction time.
The green approach method uses sulfuric acid to create the acid environment needed for the oxidant to oxidize graphite, the reaction is stirred for 1 hour at room temperature, it requires no heating or cooling which makes it ideal to scale up. The graphene oxide obtained from this method has been compared with the methods using $KMnO_4$ as oxidant. The comparison is based on the characteristics of the produced material.
Raman spectroscopy and Fourier transform infrared spectroscopy (FT-IR) which both compliment each other, the Raman spectra both have the D peak $(1,353cm^{-1})$, G peak$(1,600cm^{-1})$, 2D peak $(2,698cm^{-1})$ and the D+G peak $(2,945cm^{-1})$ (figure 2.5a). The FT-IR spectras indicate the same functional groups for both methods, O-H stretching vibrations $(3,414cm^{-1})$, C=O stretching vibrations $(1,726cm^{-1})$, C=C from sp^2 bonds $(1,624cm^{-1})$, O-C-O vibrations $(1,260cm^{-1})$, C-O vibrations $(1,087cm^{-1})$ (figure 2.5e)
X-Ray diffraction (XRD) indicate the interlayer spacing of GO^{Fe} to be around 9.0 which is comparable to the 8.7 of GO^{Mn} (figure 2.5b).
Ultraviolet-visible spectrophotometry (UV-Vis) in water shows a strong absorption peak at $230nm$ and a weaker peak at around $300nm$ (figure 2.5c). Thermogravimetric analysis (TGA) shows similar weightloss plots, $48-50\%$

at 800°C (figure 2.5d). X-ray photoelectron spectroscopy (XPS) shows the presence of similar chemical bonds, $C = C$ (284,86eV), epoxy/hydroxyl $C - O$ (287,0eV), $C = O$ (288,0eV) and $O - C = O$ (289,2eV) (figure 2.5f-h). [7]

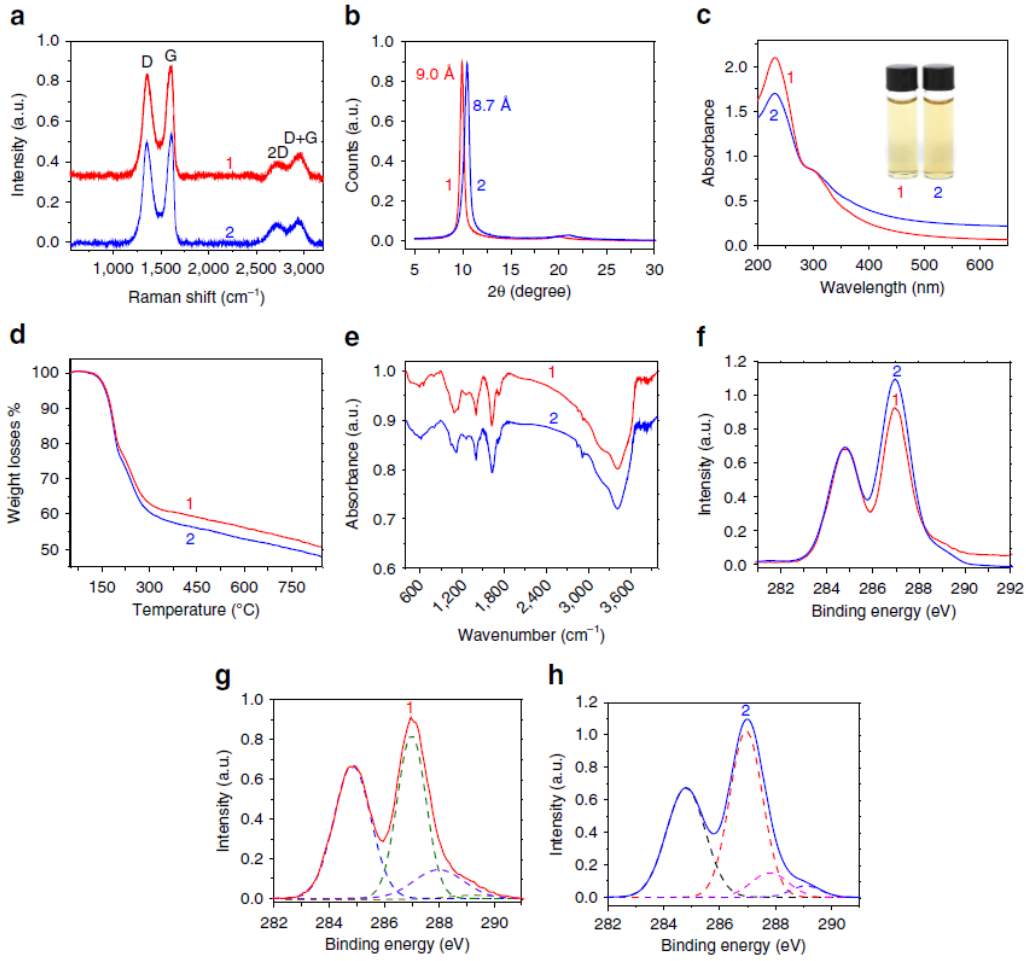

Figure 2.5: *Comparison of* GO^{Fe} *(1) and* GO^{Mn} *(2). (a) shows raman spectra using 514nm laser excitation, (b) XRD spectra, (c) UV-Vis spectra in aqueous solution at* $0,05mgml^{-1}$*, (d) TGA plots, (e) FTIR spectra, (f-h) XPS spectra and C1s XPS spectra.*[7]

This new method for producing graphene oxide using K_2FeO_4 as oxidant, is a possible candidate for replacing Hummer's Method/Tour's method for producing graphene oxide on a large scale, since it has a shorter reaction time and does not use polluting heavy metals.

2.3 Reduced graphene oxide

The main goal when reducing graphene oxide is to create a graphene like material which is insoluble in water, this reduction can be accomplished by chemical,

thermal, photothermal and laser-induced reduction methods. All these methods remove oxygen containing functionalities of graphene oxide along with converting the bindings in the basal plane to sp^2 from sp^3 hybridization, restoring the aromaticity to an extent, see figure 2.6 [4]

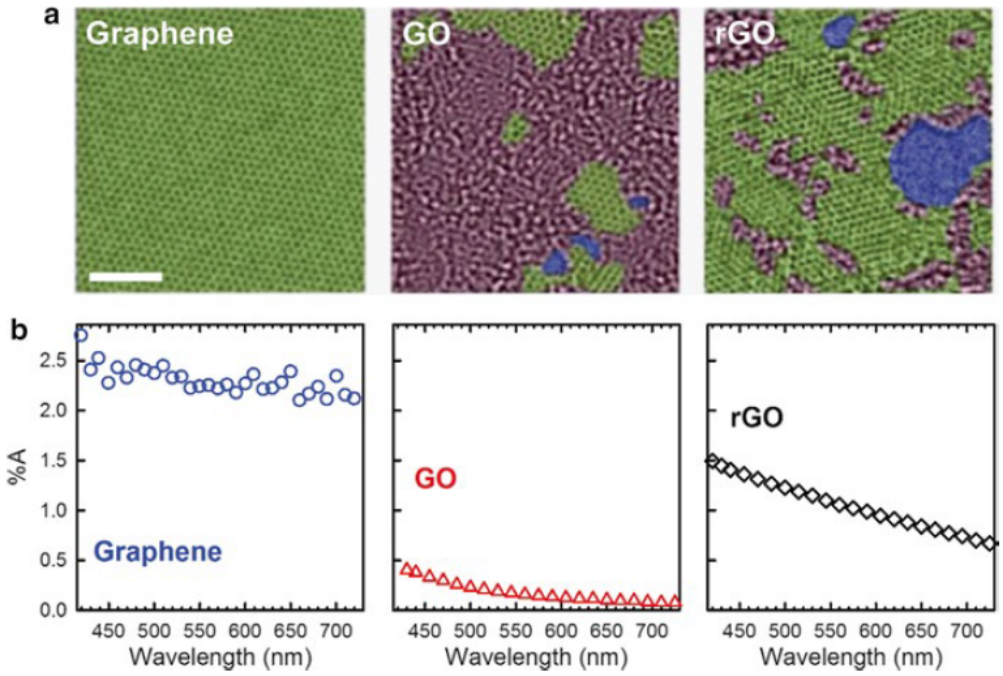

Figure 2.6: *(a) Aberration corrected TEM images of graphene, GO and rGO. The green regions indicate perfect sp^2 character, the red regions indicate disorganized oxidized portions and the blue regions indicate defects/holes. Bar scale: 2nm. (b) Visible absorption spectra of single layer graphene, GO and rGO.*[4]

Figure 2.6 shows high contrast aberration corrected transmission electron microscopy (TEM) images of graphene, graphene oxide (GO) and reduced graphene oxide (rGO). The scans shows sp^2 regions as green, oxidized regions sp^3 as red and holes/defects as blue. From these scans it becomes clear that graphene oxide gains a significant amount of sp^2 characteristics when reduced, which makes it resemble graphene but with oxidized regions, holes and defects.[4]

2.4 Thermal Reduction of Graphene Oxide

For investigating the thermal reduction of graphene oxide, the researchers of this paper decided to use modified Hummer's method to prepare graphene oxide, the results were analyzed using X-ray diffraction (XRD), (a description of how XRD works, can be found in the Characterization chapter section 6.2) in short the sample diffracts x-rays and from the results gathered, the distance

between layers (d_{002}) can be calculated and also the thickness of the layers. Figure 2.7 shows interlayer distances for different kinds of graphene(GP) and graphene oxide(GO), GP layers have intrinsic nanocurvature distortions (Fig 2.7b) causing the interlayer distance to be slightly larger than bulk graphite, interlayer distances for GP has been reported to be 3.348-3.360Å. Thermally reduced GP (Fig 2.7c) has defects which causes it to gain a larger interlayer distance compared to GP. Oxidized GP (Fig 2.7d) have oxide groups within the layers, causing it gain a larger interlayer distance. GO has the largest interlayer distance (Fig 2.7e), due to the intercalated H_2O molecules and various oxide groups, the reported distances for GO is in the range of 5-9Å. It is therefore safe to assume the order of interlayer distance is $d_{GO} > d_{Ox} > d_{Df} > dGp > graphite$.[8]

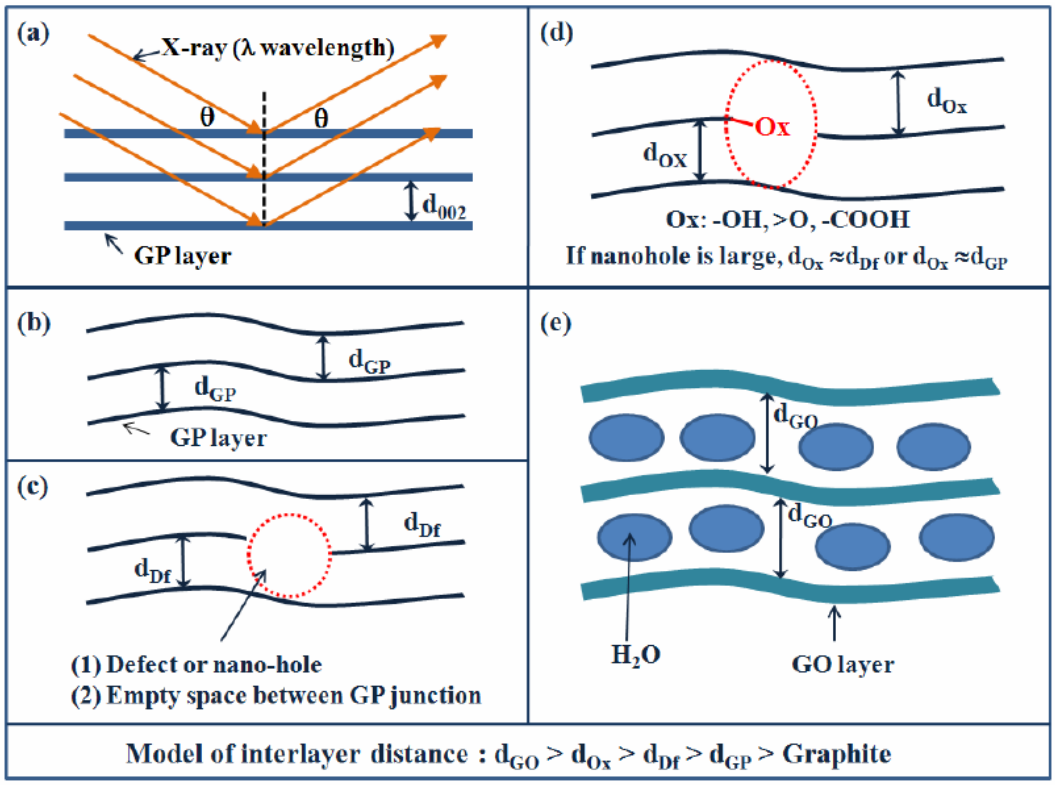

Figure 2.7: *Bragg's law for graphene or graphite (002) planes (a), and models for d_{002} and graphene oxide (e) and thermally reduced graphene (b-d). With this model the order of interlayer distance is: graphite $< dGP < d_{Df} < d_{Ox} < d_{GO}$[8]*

The graphene oxide slurry obtained was spin-coated upon a flat Pt XRD holder and dried at room temperature, the thickness of the GO film was approximately $300 - 500nm$. The GO film mounted on the XRD holder was measured in situ in vacuum at room temperature up to $1000°C$ with a heating rate of $5°C/minute$.

The XRD pattern for GO film shows a typical XRD pattern with a sharp strong peak (002) peak at $2\theta \approx 11°$, when thermally reducing GO this peak

gradually moves to the right and produces three types of (002) peaks series. The first peak series (Peak 1) is the main change during the thermal reduction, the d values for unreduced GO (Fig 2.9a) is 8.071Å and for GO reduced at 1000°C (Fig 2.9t) it is 3.453Å.

The second peak (Peak 2) appears at $2\theta \approx 24°$ at around $140°C$ reduction (Fig 2.9d), the peak shifts slightly to the right in the temperature range: $140 - 600°C$, at $600°C$ Peak 1 and 2 are combined. The d values obtained for GO reduced at $140°C$ is 4.034Å and for reduction at $600°C$ it is 3.593ÅİIts worth noticing that Peak 2 has a broad peak resulting in higher FWHM values, this is because of vaporization of intercalated H_2O molecules.

The third peak (Peak 3) is a small shift to the right from Peak 2, the d values are far from those of graphite, and the intensity of the peak is lower than those of Peak 1 and 2, the material at Peak 3 is assumed to be amorphous-like carbon with many defects, impurities and folding structures. [8]

The combined XRD results of the annealed GO film can be seen on figure 2.8 and the individual XRD measurements can be seen on figure 2.9

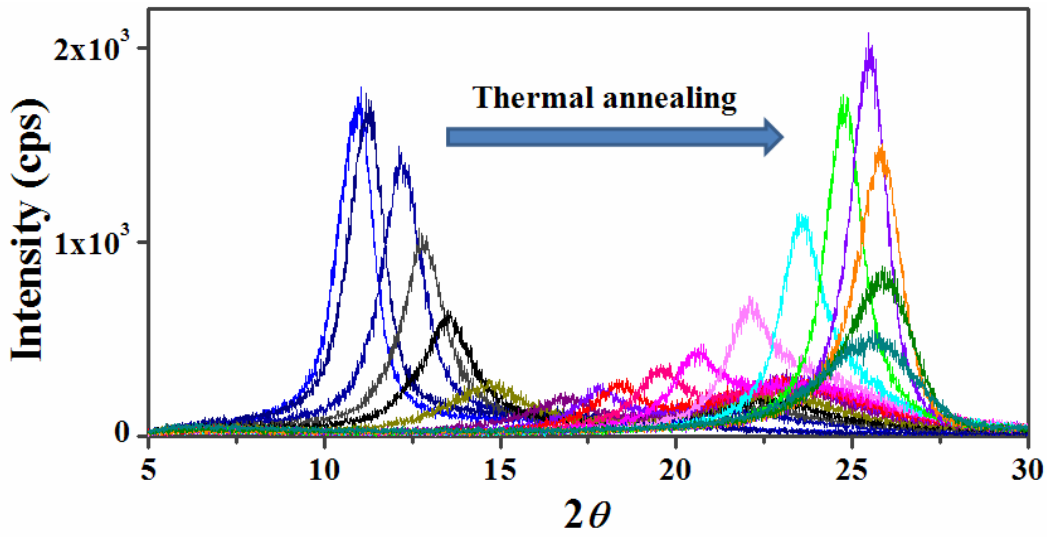

Figure 2.8: *Combined XRD patterns of GO film obtained from room temperature to* $1000°C$ [8]

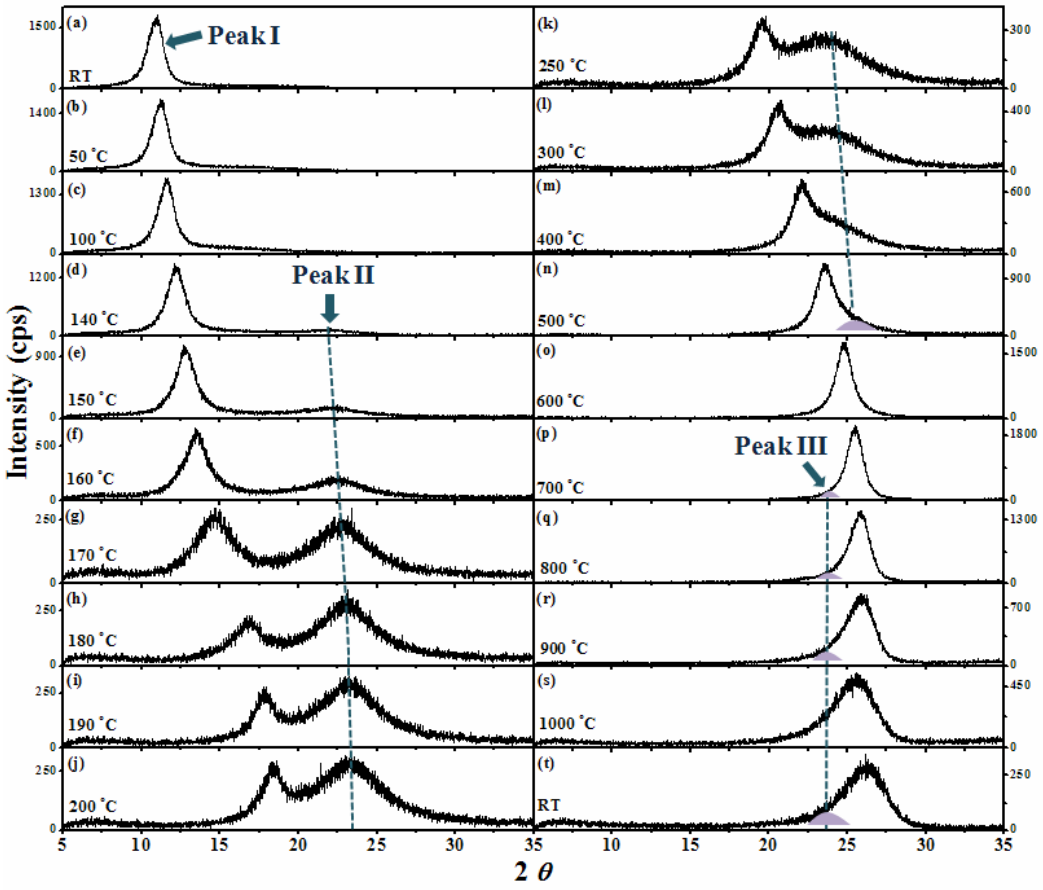

Figure 2.9: *Individual XRD patterns, used to used for creating figure 2.8*[8]

From the XRD spectra obtained, the d and FWHM values from Peak 1 and Peak 2, were plotted to show the change with temperature (figure 2.10), its clear that the d_{002} decreases with the increase in temperature, getting close to the that of pure graphite. The FWHM plot shows that Peak 2 has higher values compared to the other peaks. The plots show four temperature-dependant tendencies: 1. $RT - 130°C$, 2. $140 - 180°C$, 3. $180 - 600°C$, 4. $600 - 1000°C$. From RT to $130°C$ only Peak 1 appears, the mild reduction in d_{002} and unchanged FWHM are the cause of mild vaporization of intercalated H_2O molecules. From $140 - 180°C$ both Peak 1 and 2 appears, for Peak 1 the d_{002} values are heavily reduced and the FWHM values are broadened. This is caused by the drastic vaporization of H_2O molecules. In this process the size of the GO crystals are reduced as they are exfoliated with the drastic escape of H_2O gas molecules, resulting in Peak 2 with a very broad FWHM. Peak 2 shows the same d_{002} and FWHM tendencies as Peak 1. In the $180 - 600°C$ area the d_{002} and FWHM values for both Peak 1 and 2 and still being reduced, this is caused by the removal of main oxide groups of COOH. Above $600°C$ the d_{002} values are still being reduced approaching graphite and the FWHM values are broadening. [8]

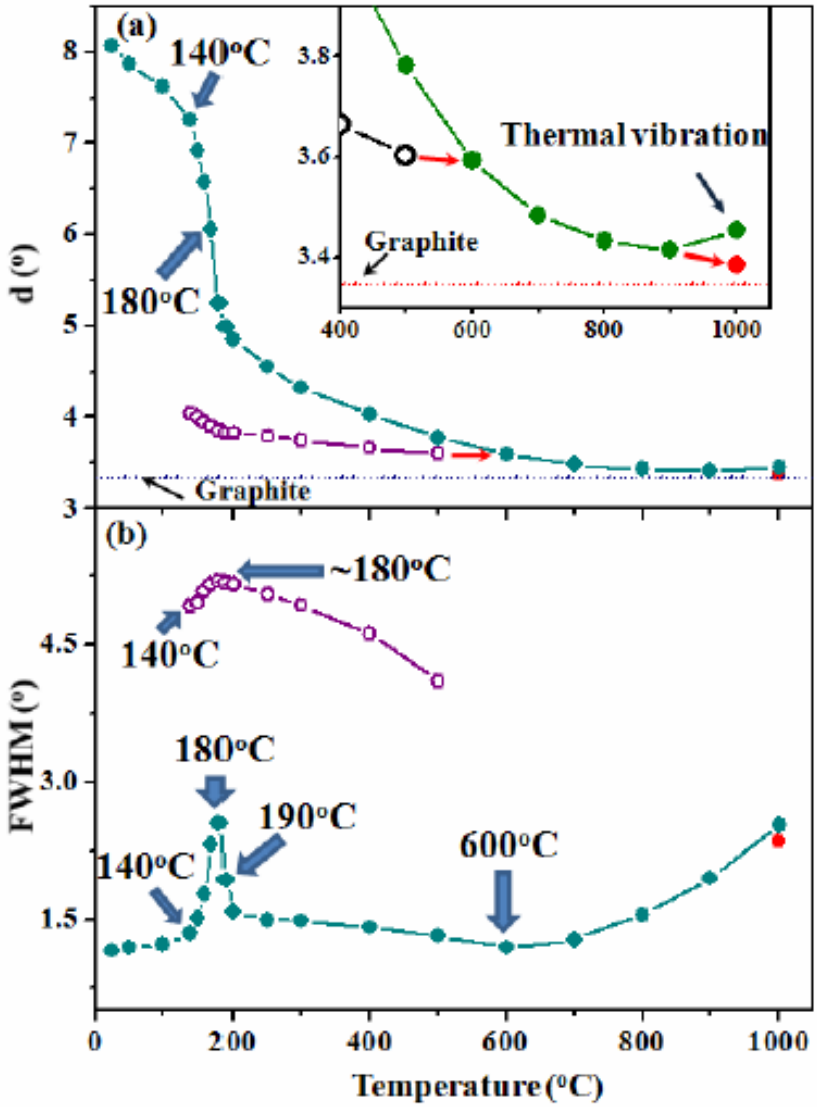

Figure 2.10: *d_{002}(a) and FWHM(b) plots for Peak 1 (solid blue circles) and Peak 2 (hollow red circles) obtained from the XRD spectra, the inset is a magnification of (a)*[8]

Based on the results from the research, a model for thermal reduction of GO was developed (figure 2.11). The model shows different states, S1 which occurs from $RT - 130°C$ where the mild vaporization of intercalated H_2O molecules happens. S2 and S7 happens at $140 - 180°C$, which is the drastic vaporization of intercalated H_2O molecules, and partial exfoliation of graphene oxide. S3 happens at $180 - 600°C$, where the lattice space is reduced caused by the removal of main carboxyl groups. S4 occurs at $600 - 800°C$ where a partial lattice relaxtion happens along with the broadening FWHM, caused by the outgassing formed from residual carboxyl and partial hydroxyl groups. S5 occurs at $800 - 1000°C$ where large defects are produced during removal of the epoxide group, along with in-plane C=C cracking. S6 occurs from $1000 - 2000°C$, where the lattice space is contracted and material defects are reduced. S8 occurs from $140 - 2000°C$ where small amounts of amorphous-

like structures are formed, this is explained by the complex folding structures, defects, impurities and the sp^1, sp^2 and sp^3 hybridization.[8]

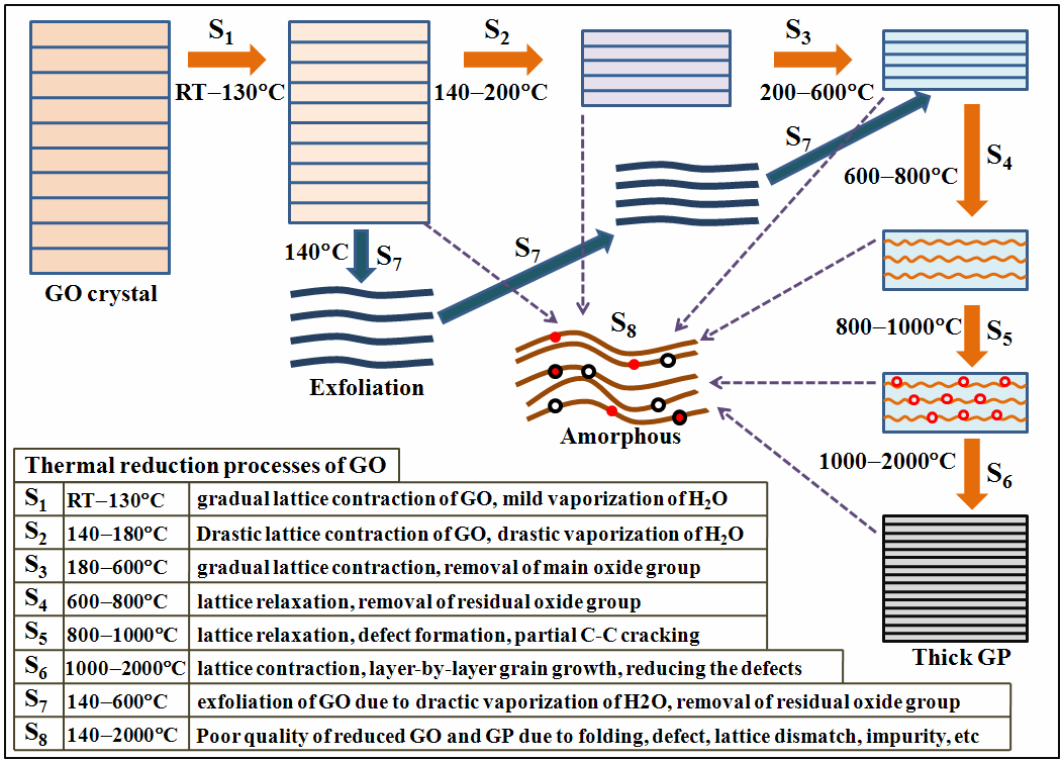

Figure 2.11: *Schematic diagram of thermal reduction process of GO from room temperature to* 2000°*C 2.8*[8]

2.5 Explosive thermal reduction of graphene oxide-based materials

Thermal reduction of graphene oxide is an important step in processing graphene oxide, it can however undergo explosive decomposition, which can cause problems during production. Studies have shown that this explosive mode is caused by exothermicity of graphene oxide reduction coupled with a threshold of sample size/mass, which causes heat and mass transfer limitations leading to a thermal runaway reaction. [9]

For these studies the research group used a modified Hummer's method for preparing the graphene oxide, the prepared solution was then pipetted onto a clean polystyrene substrate and left to dry overnight at room temperature. Next day the same amount of the graphene oxide solution was added to the previous layer, and left to dry overnight, several cycles like this was performed in order to create graphene oxide sheets of various thickness. The samples prepared were analyzed used TGA (thermogravimetric analysis) and DSC (differential scanning calorimetry).[9]

During the experiments they sometimes observed violent decomposition events in the TGA during the $10\frac{K}{min}$ heating in inert gas, failing the experiment and covering the interior of the device with a fine powder product. They also observed explosive decomposition when using DSC, tearing apart the sample pan and spreading fine powder throughout the cell, see figure 2.12.[9]

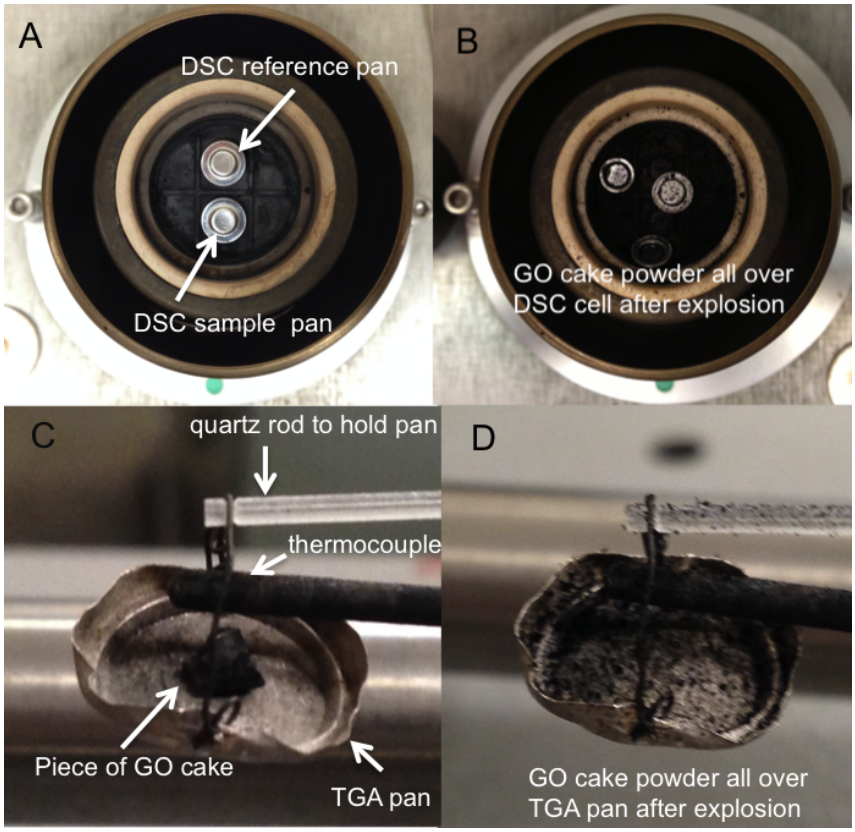

Figure 2.12: *Images of the result of exploding GO in DSC and TGA, (A) shows DSC before, (B) shows DSC after, (C) shows TGA before and (D) shows TGA after.*[9]

Then testing was done to the 15-cycle drop cast film, the thermal reduction lead to a large exothermic peak in DSC with a decomposition ΔH of approximately $1680\frac{J}{g}$, this corresponds to an estimated adiabatic final temperature of $1240°C$, calculated for the case where the onset temperature is $150°C$ (figure 2.13A). The reduction creates a porous rGO product and does not explode, the weight loss from the decomposition is approximately 40wt.% The experiments of the 15-cycle drop cast film showed a continuous and smooth heat evolution and it did not produce an explosion. They attribute this to the thin film structure which allows sufficient fast heat transfer to prevent local temperature rise causing thermal runaway. Similar behavior was observed when testing the 15-cycle film in TGA in inert environment (figure 2.13B+C). The reduction produces a porous rGO film but does not explode. Additional adsorption analysis for BET surface area were made, showing that low temperature, low heating rate atmospheric pressure thermal reduction of GO film

produce relatively non porous rGO. Thicker GO films (SEM image on figure 2.13E)reduced in DSC obtain much higher higher area values, N_2 surface area of $171\frac{m^2}{g}$ and CO_2 BET area as large as $1471\frac{m^2}{g}$, with a small pore size of approximately $0.35nm$ (figure 2.13F), this micro pore size range is the range that shows molecular sieving behavior. [9]

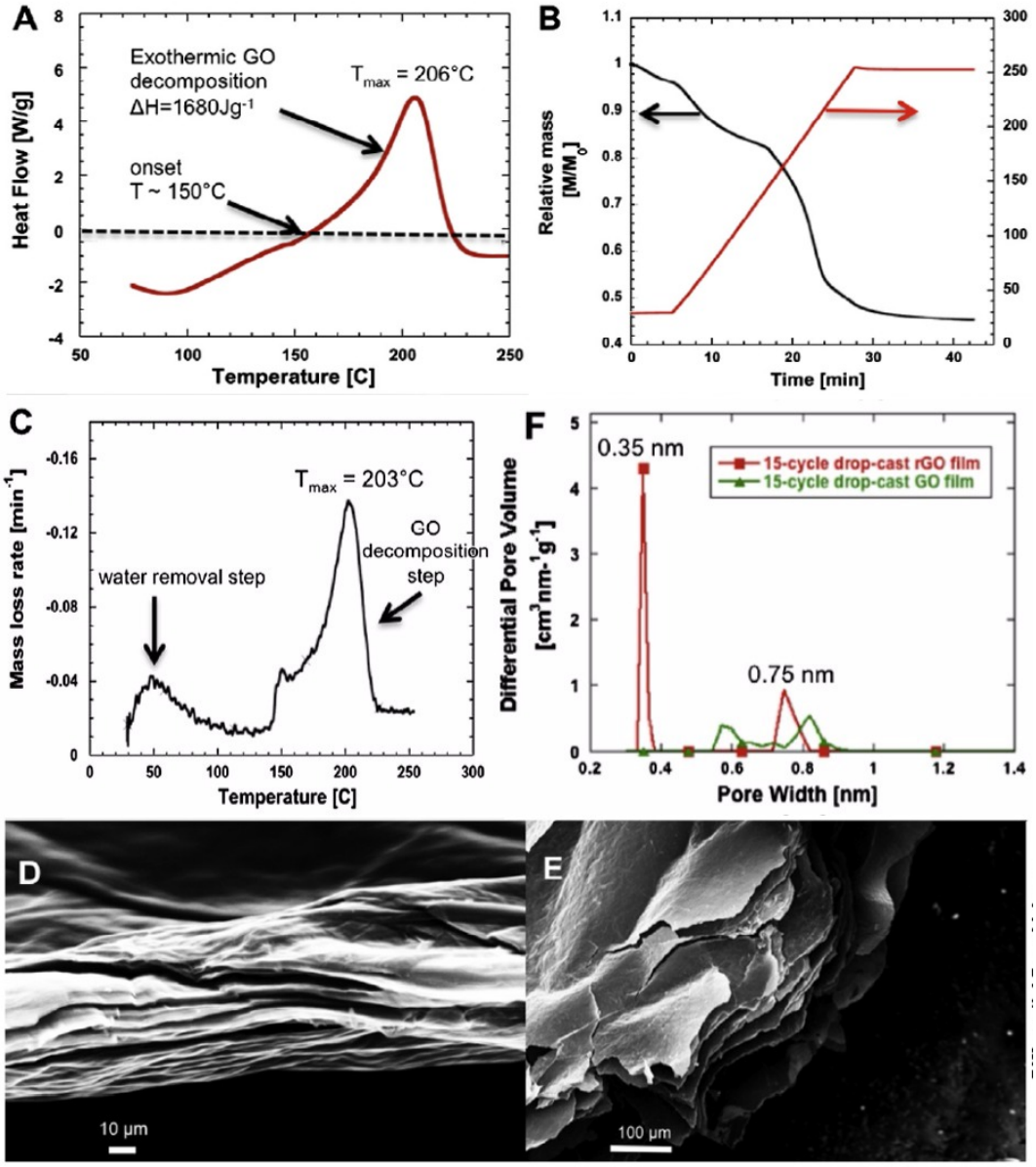

Figure 2.13: *Thermal analysis of the GO reduction process and pore structure of the rGO product. (A) DSC thermogram of 15-cycle GO in* $50\frac{ml}{min}N_2$ *flow with a heating rate of* $10\frac{K}{min}$*, (B) TGA curve of 15-cycle GO in* $100\frac{ml}{min}N_2$ *flow with a heating rate of* $10\frac{K}{min}$*, (C) Differential TGA curve of 15-cycle GO, (D) SEM image of 9-cycle dropcast GO film, (E) SEM image of 15-cycle dropcast GO film, (F) 15-cycle GO and rGO* CO_2 *isotherm NLDFT pore size distribution applying slitpore model.*[9]

Additional tests with the GO cake showing explosive behavior was made,

to determine if the interstitial water was the cause of the explosions. The normal GO cake exploded when heated in DSC (figure 2.14A), it had a very clear endotherm curve when the water evaporated with a peak at $126°C$, following this peak is the exotherm GO reduction peak. The exothermic peak is asymmetric, it rises smoothly and then drops suddenly, indicating that the material exploded. To test if the interstitial water was the cause of the explosion, a piece of the GO cake was taken and ovendried at $80°C$ overnight before testing it in DSC (figure 2.14B). The DSC results did not have the endotherm curve for water removal, the testing still ended with the GO cake exploding, noticeable by the asymmetric exothermic peak dropping abruptly. With the water missing from the sample, the onset temperature for the GO thermal reduction could be determined at $140°C$. The final test made was with a GO cake that did not show explosive behavior, a piece of this sample was humidified in a saturated water vapor environment overnight before analyzed in DSC (figure 2.14C). The humidified GO cake did not explode, the results from the humidified GO cake shows a very large endotherm curve when removing the water, the onset temperature for the GO thermal reduction is shifted to 160°, the exothermic curve is very smooth and doesnt drop abruptly. The experiments clearly shows that water is not the cause of the explosive thermal reduction of GO. [9]

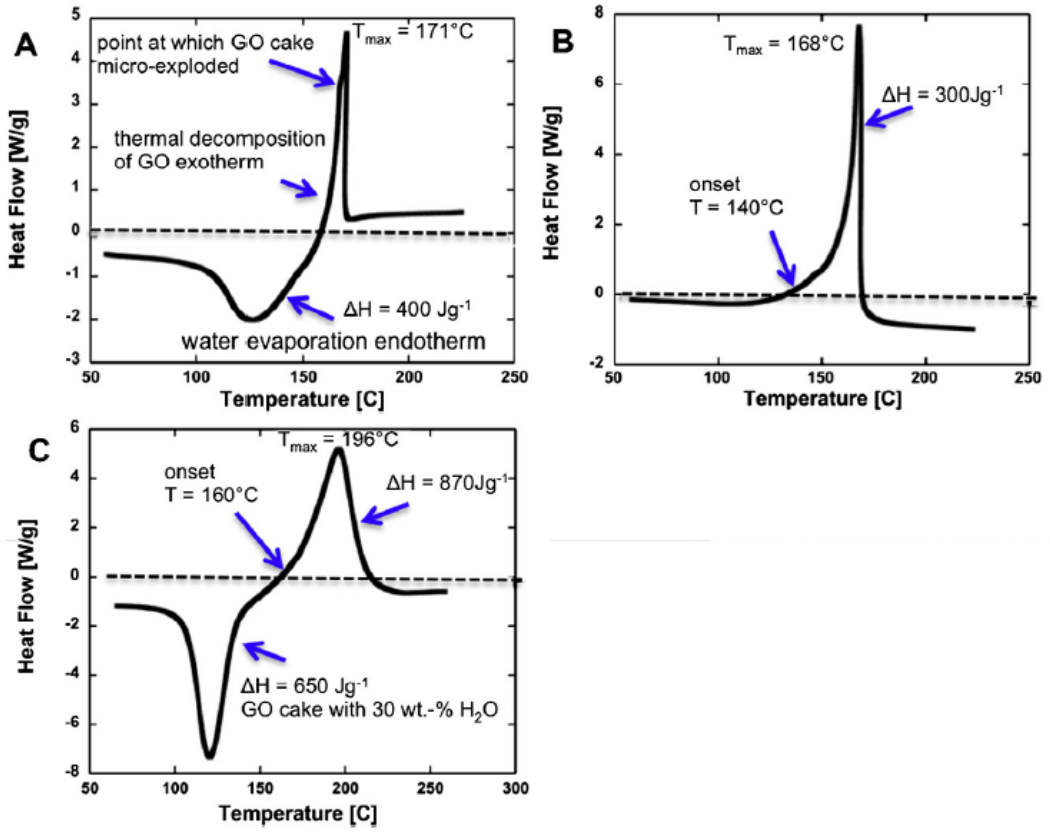

Figure 2.14: *Effect of interstitial water on the mode of GO thermal reduction (explosive vs. non-explosive). (A) GO cake which exploded during thermal reduction in N_2 gas. (B) GO cake oven dried for 24-hours at low temperature which exploded, noticeable by the truncated asymetric exotherm. (C) Humidified GO cake which didnt explode, note the large water endotherm and the smooth exotherm indicating no explosion.* [9]

Since water did not promote the explosive behavior, further testing with potassium was done, since potassium permanganate is commonly used for synthesizing GO, potassium residues would be a possibility. For testing this hypothesis a GO cake without explosive behavior (figure 2.15A) was selected. A piece of the GO cake was immersed in a KOH solution prior to DSC testing (figure 2.15B), the sample exploded indicating that potassium or hydroxide promotes the explosive behavior, the onset temperature for the thermal reduction was lowered by approximately $50°C$. Potassium has been known to increase CO and CO_2 yields, lowering the pyrolysis activation energy by $50\frac{kJ}{mol}$ and lowering the main pyrolysis temperature by approximately $50°C$, which corresponds to the difference in onset temperature observed in the tests. Potassium hydroxide promotes the GO explosion, further testing to see if it is needed for the explosion was done. TGA experiments with varying GO cake mass was conducted. A GO cake known to explode in DSC and a low potassium GO cake which did not explode in DSC, was tested with the same heating conditions in TGA (figure 2.15C+D), both samples exploded during testing, the low potassium cake exploded at $196°C$ and the one with higher potassium

content exploded at $167°C$, therefore the potassium content is not required for the explosive behavior. Testing with different GO cake mass showed that by increasing the mass, the explosive behavior was initiated (figure 2.15E). For other energetic materials thermal runaway reactions have been known to occur, when the heat from the decomposition reaction cannot dissipate to the surroundings fast enough, leading to localized temperature rises.[9]

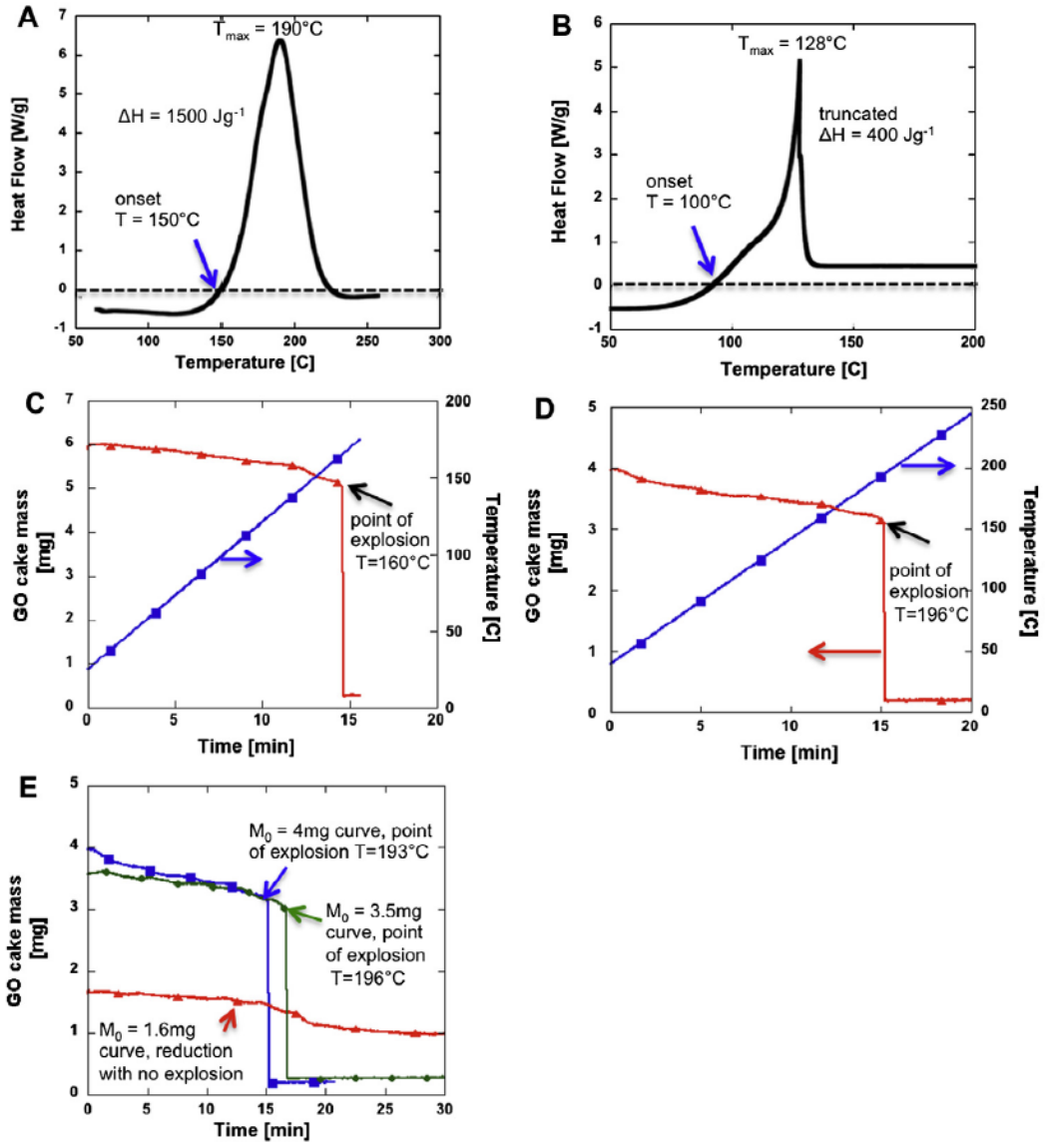

Figure 2.15: *Effects of potassium in GO and total sample mass. (A) DSC graph for a GO cake without explosion. (B) DSC graph of the same sample as (A), this time immersed in KOH solution and dried, this time showing explosive behavior. (C+D) TGA graphs from 2 different GO cakes, (C) has a 33-fold higher K content than (D), notice the change the temperature needed for the material to explode. (E) TGA curves for samples with low K content and varying sample mass, notice how the small mass sample does not explode, while the higher mass ones do.*[9]

2.6 Graphene oxide: the new membrane material

In the recent years, graphene oxide has emerged as a material that can be used to filter ions and molecules. Nair et al. demonstrated in 2012 that graphene oxide membranes allows un-impeded permeation of water and blocking everything else in vapor form. For the experiment they set up a glove box on a weight, with a graphene oxide membrane sealing the opening. When ethanol was put in the box, there was no noticeable weight change, when water was put in the box, the weightloss observed was close to that of an open box. When the box was filled with gasses (He, H_2, N_2 and Ar) with a slight overpressure, there was no variation in weight. The conclusion was that no gas could pass through the membrane. They also proposed a model of the possible water transport mechanism through the membrane. Furthermore a membrane thermally reduced at $250°C$ was tested, blocked the water vapor, the main reason for this was believed to be because of the removal of oxygen containing functional groups, effectively reducing hydrophilicity and the distance between the layers, see figure 2.16[10].

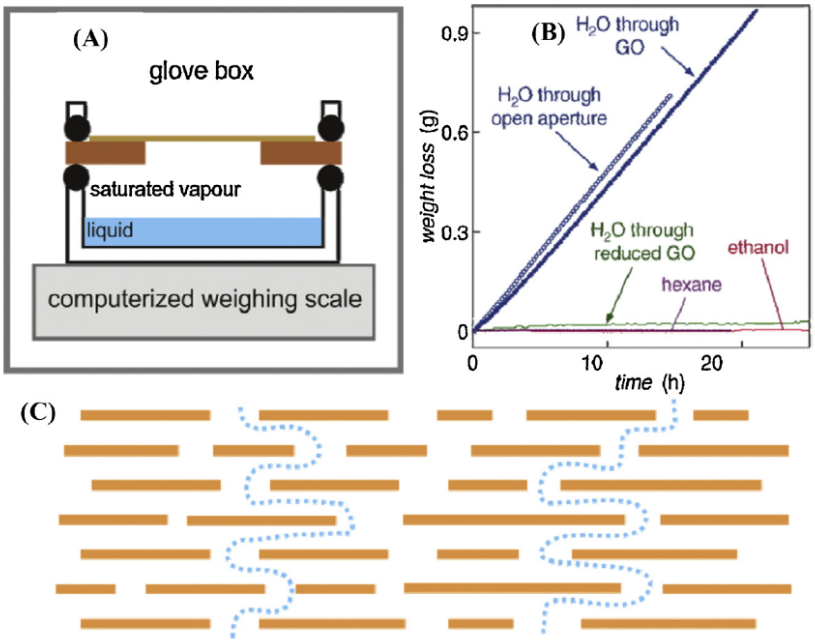

Figure 2.16: *(A) Schematic of the experiment setup used to assess the permeation of GO layers. (B) Plot showing the results of the vapour permeation, weight loss of the container filled with the target solution over a period of time. (C) Schematic representing the possible water transport mechanism.*[10]

Nair et al. explained that the GO laminate created was made up of crystallites stacked on top of each other, with hydroxyl and epoxy groups attached to the sheets, which provided spacing between the membranes. According to this model, the pristine graphene capillaries are wide open and allows water

molecules to pass, in low humidity the distance is lower and hinders the water molecules, this mechanism can seen in figure 2.17[10]

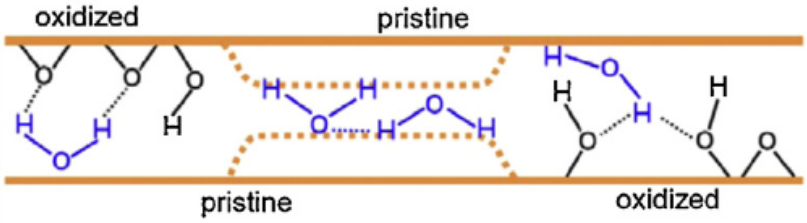

Figure 2.17: *Model of the nanocapillaries in graphene oxide films. Monolayer water can move through the capillaries, however in low humidity the capillaries becomes narrower (indicated by dashed lines), as a result there is not enough space for the water molecules to pass.*[10]

2.7 Summary

Graphene oxide is made from oxidizing graphite, which adds oxygen-functional groups to the basal planes of the graphite, effective making it hydrophilic and soluble in water. If it is to be used for filtering in water treatment, the material needs to be reduced in order to make it insoluble in water, this can be done using thermal treatment. When thermally treating GO, oxygen containing functional groups are removed, making it less hydrophilic. Caution should however be taken, as it can show explosive behavior with a onset temperature around $150°C$. Pure GO membranes allow unimpeded permeation of water vapor, while GO membranes reduced at $250°C$ blocks it. Information regarding membrane technology will be covered in the next chapter.

3 Membranes

A membrane is defined as a selective barrier that allows the passage of some particles, while blocking others. They are widely used for industrial purposes, with the focus in this project being on water treatment. This section will give a brief historical introduction to membrane development followed by explanation of basic membrane concepts.

3.1 Historical development of membranes

The history of membranes dates back to 1748 when Abbé Nollet conducted an experiment using wine, an animal bladder and water. The wine was placed in a vessel, and the mouth of the vessel was then closed with an animal bladder, followed by the submersion of the vessel in water. Nollet then observed how the animal bladder would swell up because it was more permeable to water than wine, thus demonstrating semipermeability for the first time. This phenomena was named "osmosis" by Dutrechet in the 1820s in order to characterize the spontaneous flow of liquid across a permeable barrier. The use of membranes continued to be used in laboratory experiments, but it would take until after World War II before membranes became commonplace, see table 3.1.[11]

Table 3.1: Milestones in membrane technology.[11]

Event	Scientist	Year
Osmosis	Abbe Nollet	1748
Laws of diffusion	Fick	1855
Dialysis, gas permeation	Graham	1861, 1866
Osmotic pressure	Traube, Pfeffer, Van't Hoff	1860-1887
Microporous membranes	Zsigmondy	1907-1918
Distribution law	Donnan	1911
Membrane potential	Teorell, Meyer, Sievers	1930s
Hemodialysis	Kolff	1944
Skinned membrane	Sourirajan and Loeb	1959
Membrane transport models	Kedem, Katachalsky, Lonsdale, Merten, Pusch, Sourirajan	1960-1970
Spiral-wound membrane element	Westmoreland, Bray	1965-1970
Hollow-fibre RO membrane	Mahon, Hoehn and Milford	1965-1970
Thin-film composite membrane	Cadotte and Rozelle	1972

The use of membranes beyond laboratories started when it became necessary to test drinking water by the end of World War II. The water supplies in Germany and other European countries had broken down, which meant that filters were needed to test drinking water. The research for these filters was done by Millipore Corporation which is still the largest producer of membranes for microfiltration in the US. Membranes did not become industrial until the early 1960's because of they were too unreliable, slow, unselective, and too expensive. This changed with the work of Loeb-Souriajan, as they were able to develop a process for creating anisotropic reverse osmosis membranes with no defects and a high flux. These membranes were made of a selective ultrathin film on the surface of a thick microporous support. This microporous support yields a greater mechanical strength while also allowing for a water flux 10 times higher than any other membrane available at that time. The work therefore resulted in a membrane with improved reliability, flux, and selectivity, which would pave the way for commercialization of reverse osmosis and help develop ultrafiltration and microfiltration, see figure 3.1. [12][11]

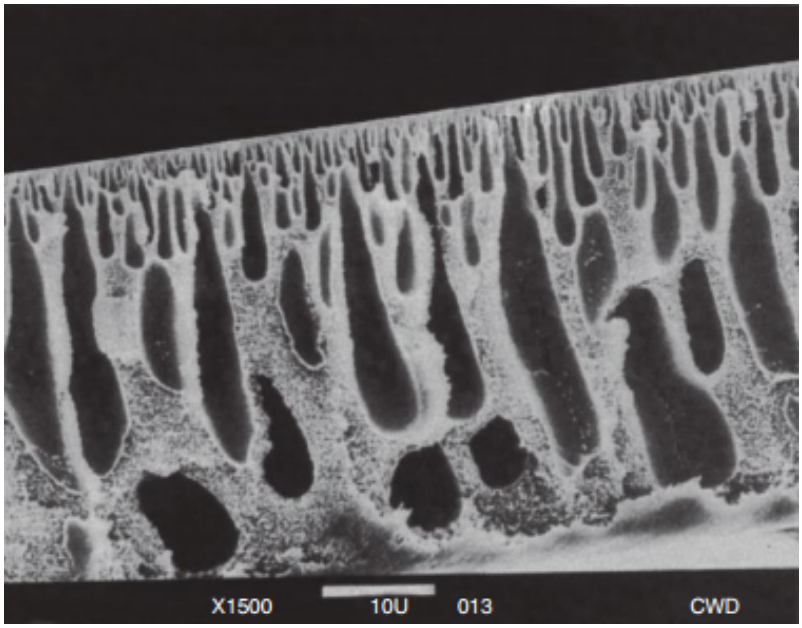

Figure 3.1: *An electron micrograph of an asymmetric ultrafiltration membrane* [11]

As seen in figure 3.1, the membrane allows for high flux due to the thin selective skin layer, supported by a much more porous layer. These membranes, called skinned membranes, have a thickness of about 0.1 mm, with the selective layer being 30-100 nm. Various technical milestones for membrane processes can be seen in table 3.2. The important milestones concerning water treatment are Microfiltration (MF), Ultrafiltration (UF), Nanofiltration (NF), and Reverse osmosis (RO).[11]

Table 3.2: Development of commercial membrane processes. [11]

Membrane process	Country	Year	Application
Microfiltration	Germany	1920	Laboratory use
Ultrafiltration	Germany	1930	Laboratory use
Hemodialysis	Holland	1950	Artificial kidney
Electrodialysis	USA	1955	Desalination
Reverse osmosis	USA	1965	Desalination
X-flow ultrafiltration	USA	1971	Concentration of macromolecules
Gas separation	USA	1979	Hydrogen recovery
X-flow micro filtration	Australia, USA	1980	Water treatment
Pervaporation	Germany, Holland	1982	Dehrydration of organic solvents
Nanofiltration	USA	1986	Water softening
Electrodeionisation	USA	1987	Demineralisation
Submerged membrane filtration/ bioreactor	Japan	1987	Water reclamation/ sewage water treatment

3.2 Membrane types

This section will give a brief introduction to the two types of membranes; isotropic (symmetrical) and anisotropic (asymmetrical) membranes.

3.2.1 Isotropic membranes

Isotropic membranes are defined as dense or porous membranes with a uniform composition structure. The thickness of these membranes determines the resistance mass transfer rate, so thin membranes are preferred for a higher permeation rate. Isotropic membranes can be microporous, nonporous and dense, and electrically charged, see figure 3.2. [13]

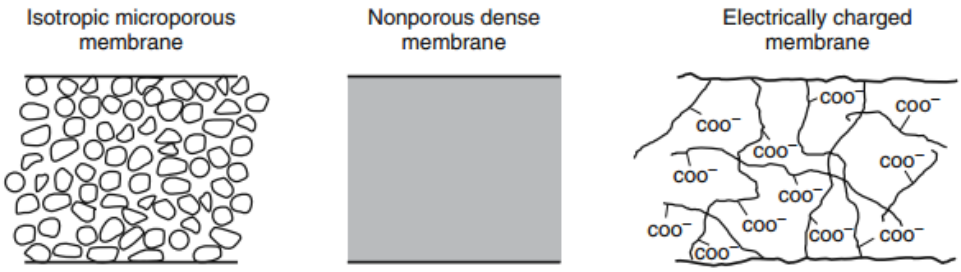

Figure 3.2: *The three types of isotropic membranes.*[12]

The microporous membrane has a structure similar in structure to conventional filters, with a voided structure of interconnected pores, randomly distributed. However, these pores are very small ($0.01 - 10\mu m$) in diameter. Generally, only molecules with a significant size difference can be separated by microporous membranes (ultrafiltration and microfiltration).

Nonporous, dense membranes are membranes consisting of a dense film, where the permeants are transported via diffusion by pressure, concentration,

or electrical potential gradient. The separation of components in the membrane depends on the diffusivity and solubility of the components in the membrane material. It is therefore possible to separate particles of similar size if their solubility is significantly different. These membranes are mostly used for gas separation, pervaporation, and reverse osmosis, where they often have an anisotropic structure in order to improve flux.

Electrically charged membranes can be either dense or microporous, but are often fine microporous membranes with positive or negative ions at the pore walls. A membrane with positively charged ions will bind anions from the fluid and is therefore called an anion exchange membrane. If the membrane is negatively charged it is called a cation exchange membrane. The separation in this type of membrane is mostly dependent on the charge of the ions being filtered, so a cation exchange membrane will exclude anions and vice versa. These membranes are used for electrodialysis. [12][13]

3.2.2 Anisotropic membranes

Anisotropic membranes have a number of layers with different structures and permeabilities. The membranes typically have a dense and extremely thin surface layer, called the skin layer, as seen in figure 3.1. This skin layer is supported by a thick porous substructure, yielding mechanical support without influencing the flux. The flux in this type of membrane is therefore determined by the skin layer.

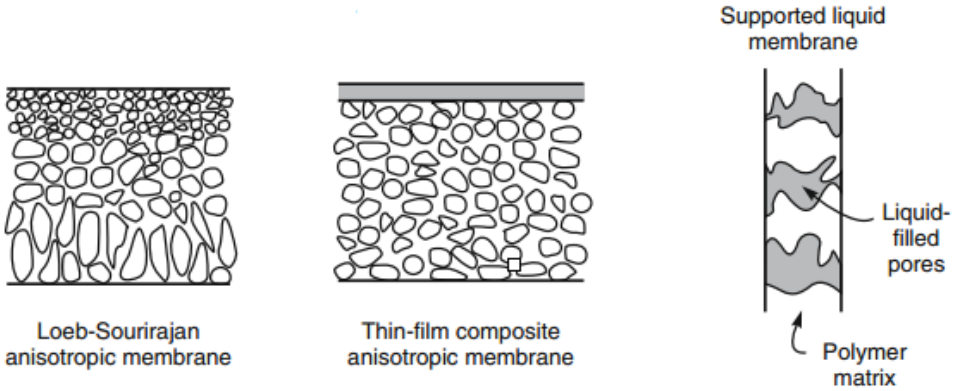

Figure 3.3: *The three types of anisotropic membranes.*[12]

As previously mentioned, the Loeb-Souriajan membrane can be seen in figure 3.1 and is also called a skinned membrane. While it consists of a single membrane material, the porosity and pore size vary significantly in different layers in membranes made by the Loeb-Souriajan process, which can also be seen in figure 3.1 and 3.3. Anisotropic membranes often consist of different layers with different functions when made by other processes. [13]

The thin-film composite membrane consists of a thin and dense film of a highly cross-linked polymer which is mounted on the surface of a thicker microporous support. This dense film is very thin (0,1 mm or less), so the membrane has high permeability, while the cross-linking provides high selectivity. These membranes are often used in reverse osmosis and nanofiltration, this is the membrane catagory graphene oxide falls under. [13] Liquid membranes are used for facilitated support, where carriers can selectively transport components at a high rate across the membrane interface. They are mostly used on pilot scale for removal of heavy-metal ions and organic solvents from industrial waste streams. [13]

3.3 Membrane Processes

There are several different membrane processes, but this section will focus on the ones important for water treatment. The relevant membrane processes in water treatment are Microfiltration (MF), Ultrafiltration (UF), Nanofiltration (NF), and Reverse Osmosis (RO), see figure 3.4.

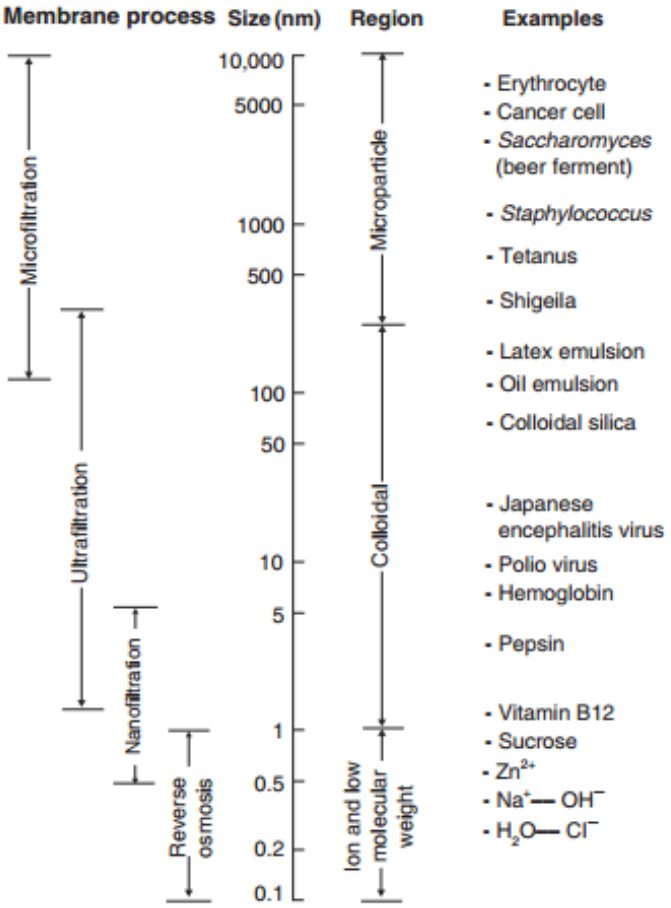

Figure 3.4: *MF, UF, NF and RO membrane processes and their range of operation.* [12]

When using membranes for water treatment the feed water is therefore run through membrane systems as listed in figure 3.4. The big particles are mainly removed in MF followed by further purification of the water in UF and then NF and/or RO is used to filtrate the remaining small particles. GO membranes will have different pore sizes, depending on whether the membranes are fully wetted or dry. According to H. Huang et al. [14], the typical pore size in dry go membranes is expected to be 0.7 nm. The hydrophilic groups in the membrane (hydroxyl, carboxyl and epoxy) are able to absorb water molecules and wetting the membrane. This results in an expansion between the layers in the membrane to more than 1 nm, which results in a pore size ranging from 3 to 5 nm in a fully wetted membrane. The GO membranes in this project will therefore mainly lie in the range of NF and RO, as can be seen in figure 3.4. The classification of the four membranes processes can be seen in table 3.3.

Table 3.3: Classification of MF, UF, NF, and RO membranes according to pore size and operating conditions.[11]

Process	Pore size	Driving force	Transport mechanism
Microfiltration	$0.05 - 10\mu m$	Pressure, 1-2 bar	Sieving
Ultrafiltration	$0.001 - 0.05\mu m$	Pressure, 2-5 bar	Sieving
Nanofiltration	$< 2.0nm$	Pressure, 5-15 bar	Donnan exclusion/ sorption-cappilary flow
Reverse osmosis	~0.6nm	Pressure, 15-100 bar	Preferential sorption-capillary flow

As can be seen in table 3.3, the operating pressure increases with decreasing pore size. With the GO membranes expected to lie in the range of NF and RO, it can be seen from table 3.3 that these processes operate under significant pressure. The GO membranes therefore have to possess enough strength to withstand these operating conditions. If the GO membrane in itself is not strong enough for these conditions, a microporous support can be used to provide the needed mechanical support. Since GO membranes will fall somewhere in the range between NF and RO, the next section will describe these processes further.

3.3.1 Reverse Osmosis and Nanofiltration

RO is a process used for removing solutes, for example dissolved ions, from a solution using a semipermeable barrier under hydraulic pressure. When using a semipermeable membrane as a barrier to separate water from a concentrated solution of ions, the water will permeate the membrane into the concentrated solution to even out the water concentration or equilibrate (osmosis). The water will continue to move through to the concentrated solution until the osmotic pressure reaches a point where further flow up the concentration gradient is prevented. If a pressure greater than the osmotic pressure is applied, the flow will be reversed, as seen in figure 3.5. [11]

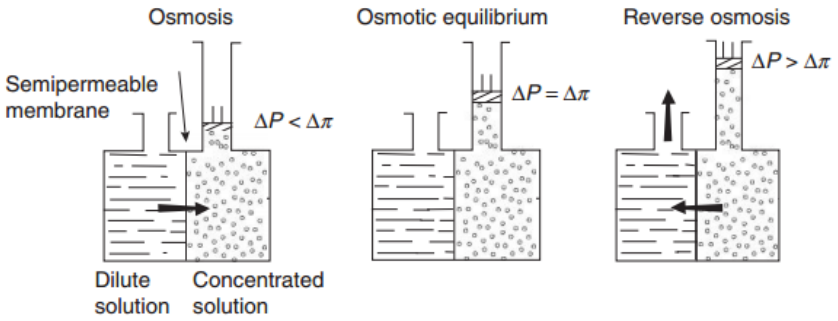

Figure 3.5: *Illustration of the osmotic phenomena.*[11]

This process is called reverse osmosis and results in a highly concentrated salt solution on the feed side, while the solution on the other side is close to pure. In this process, water practically gets squeezed out through the membrane when applying pressure. The effective water flow through a RO membrane at constant temperature is described by the following equation:

$$J_W = A(\Delta P - \Delta\pi)$$

Where J_W is the water flux of the membrane, A is the membrane permeability coefficient for water, ΔP is the hydraulic pressure differential across the membrane, and $\Delta\pi$ is the osmotic pressure differential across the membrane.

NF is very similar to RO and is also called "loose RO". The principles of NF are therefore similar to RO, but the rejection rate of solutes depends on molecular size and Donnan exclusion effects. The Donnan effect is a description of the behavior of charged particles near the membrane surface, where the particles are not evenly distributed across the two sides of the membrane. In NF membranes this is due to carboxylic and sulfonic acid groups, so GO membranes will also exhibit this behavior. The equilibrium between the bulk solution and the charged membrane is an electrical potential called the Donnan potential. The membrane will reject ions smaller than the pore size because of Donnan exclusion. [11]

NF membranes are usually polyamide thin-film composite membranes (PA TFC). As with RO TFC membranes, the PA is used as a selective barrier mounted on a UF support membrane. According to [11], the rejection characteristics of RO and NF membranes are [11]:

- Monovalent ions (Na, K, Cl, NO_3): >98% for RO, >50% for NF
- Divalent ions ($Ca, Mg, SO4, CO_3$): >99% for RO, >95% for NF
- Microsolutes (MW> 100 Da): >90% for RO, >50% for NF
- Microsolutes (MW<100 Da): 0-90% for RO, 0-50% for NF
- Bacteria, viruses: >99% for RO, <99% for NF

Where MW is the molecular weight and Da is Daltons ($\frac{g}{mol}$).

The membrane surface charge is also of significant importance when filtering. The rejection of various salts has been characterized according to surface charge [11]:

- Anionic NF membranes: Positive charges will repel anions, especially Mg^{2+}. These charges will also attract anions, especially SO_4^{2-}. Salt rejection is $CaCl_2 > NaCl > Na_2SO_4$
- Neutral NF membranes: The rejection of salts will depend on particle size. Salt rejection is $Na_2SO_4 > CaCl_2 > NaCl$
- Cationic NF membranes: Negative charges will repel anions like SO_4^{2-} while attracting cations, especially Ca^{2+}. Salt rejection is $Na_2SO_4 > NaCl > CaCl_2$.

Advantages of NF membranes over UF and RO are listed below [11]:

- Because they are able to selectively reject organic compounds with low MW and divalent ions, they are a better alternative to UF and RO for treating wastewater.
- When separating salts with monovalent ions from organics with a MW in the range of 200-1000 Da, NF membranes can concentrate the compounds with high MW, while removing monovalent ions.
- When treating bleaching effluents from paper and pulp plants, NF is cheaper than RO, which has lower flux and higher energy cost. It is also more efficient than UF at rejecting low MW toxic chlorinated compounds.

3.4 Membrane Transport Theory

When describing the permeation through a membrane there are two models; the pore-flow model and the solution-diffusion model, see figure 3.6.

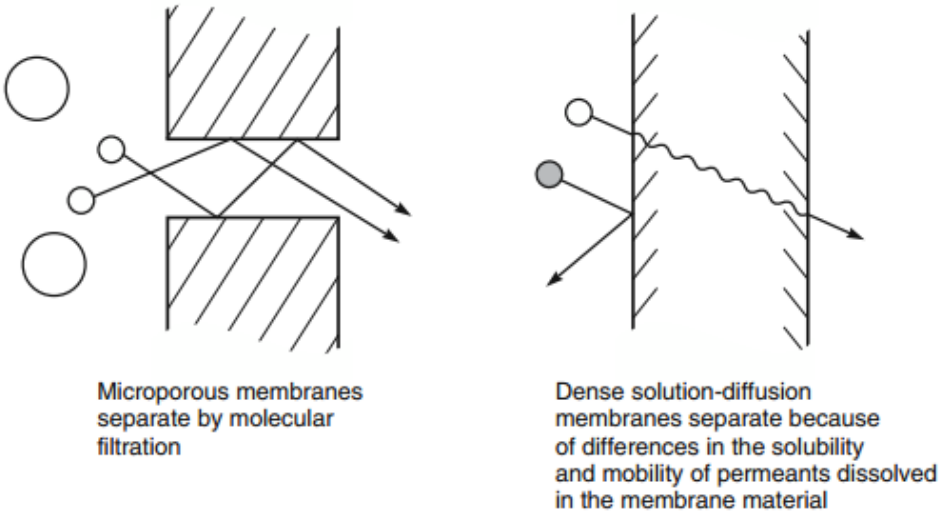

Figure 3.6: *Molecular transport through membranes via the pore-flow model and the solution-diffusion model.*[12]

In the pore-flow model the permeants are transported through tiny pores by pressure-driven convective flow. The separation occurs because particles larger than the smallest pores are filtered while smaller particles permeate the membrane. In the solution-diffusion model the permeants dissolve in the membrane material and the rate of diffusion through the membrane is based on their solubility in the material. This diffusion is a process in which permeants are transported from one side of a system to another by a concentration gradient. The permeant molecules in the membrane are moving in a constant random motion, and therefore it is not possible to predict how each molecule will diffuse through a membrane. However, if the permeate forms a concentration gradient in the membrane, a net transport of permeate will occur from the high concentration to the low concentration region. For example, if two adjacent sections in a membrane differ in permeant concentrations, there will be a higher transfer of molecules to the segment with the lowest concentration and hence moving towards a sort of equilibrium. This concept was recognized by Fick theoretically and experimentally in 1855, resulting in the formulation of Fick's law of diffusion[12]:

$$J_i = -D_i \frac{dc_i}{dx}$$

Where J_i is the rate of transfer for component i or flux ($\frac{g}{cm^2 \times s}$), $\frac{dc_i}{dx}$ is the concentration gradient of component i ($\frac{g}{cm^3 \times cm}$), and D_i is the diffusion coefficient ($cm^2 \times s$) and describes the mobility of individual molecules. The minus sign is because the direction of diffusion is down the concentration gradient. Diffusion is a slow process, so high flux is achieved by creating large concentration gradients in the membrane, while also reducing the thickness of the membrane as much as possible. [12]

The pore-flow model, which relies on pressure-driven convective flow, is mostly used to describe the flow in a porous medium or capillary. This type of transport is described by Darcy's law:

$$J_i = K' c_i \frac{dp}{dx}$$

Where K' is a coefficient reflecting the nature of the medium, c_i is the concentration of component i in the medium, and $\frac{dp}{dx}$ is the pressure gradient existing in the porous medium. Pore-flow pressure-driven membranes generally have higher flux than membranes using simple diffusion.

The difference between pore-flow and solution-diffusion mechanisms is due to the relative size and permanence of the pores. For membranes which are best described by the solution-diffusion model and Fick's law, the pores in the membrane are tiny spaces between polymer chains caused by thermal motion of the polymer molecules. These pores appear and disappear as permeants diffuse through the membrane. In membranes where the transport is best described by the pore-flow model and Darcy's law, the pores are relatively large and fixed, meaning they do not fluctuate in position or volume as permeant passes through the membrane. With larger pore sizes, there is a bigger chance they are present long enough to give the characteristics of a pore-flow membrane. A general rule of thumb is that the transition between transient pores (solution-diffusion) and permanent (pore-flow) is a pore diameter around 5-10Å. [12]

It is difficult to directly measure the average pore diameter of a membrane, and it is therefore often determined by analyzing the particle size of permeants or by other indirect methods. Membranes can be divided into the three groups seen in figure 3.7.

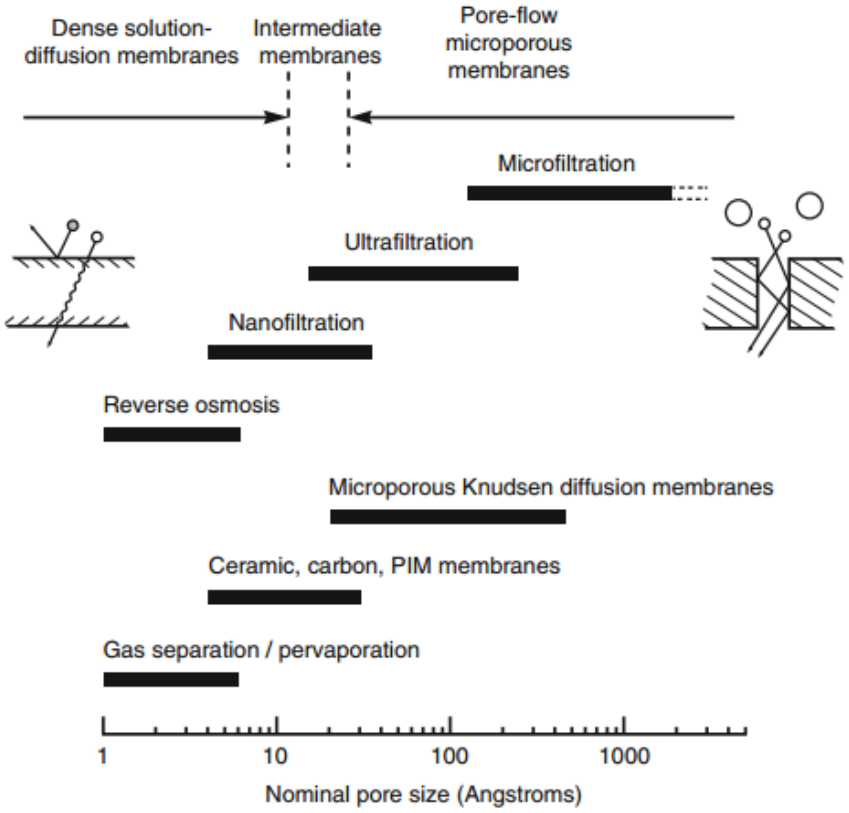

Figure 3.7: *A representation showing the nominal pore size and their proposed transport models.*[12]

UF and MF membranes are both clearly microporous membranes, as they contain pores larger than 10-15Å in diameter. The transport can therefore be described by pore-flow and Darcy's law. RO membranes have a dense selective polymer layer with no visible pores and show different transport rates for molecules with diameters as small as 2-5Å. The flux through these membranes is significantly lower than through microporous membranes and is best described by the solution-diffusion model. The space between polymer chains in RO membranes is less than 5-10Å in diameter. The pores in these membranes are transient, meaning that they appear between polymer chains as a permeant diffuses through the membrane. The membranes with pore sizes in the range of 5-15Å are intermediates between microporous and solution-diffusion membranes. As can be seen in figure 3.6, NF membranes are intermediates between UF and RO membranes, UF membranes clearly being microporous and RO membranes clearly being dense films. As previously stated, dry GO membranes will lie in the area of RO and are therefore best described by the solution-diffusion model. When used for water treatment, the membranes will be wetted and therefore have an increase in pore size, putting them in the area of NF. These membranes therefore fall in the range of intermediate membranes, so transport is described by both pore-flow and solution-diffusion.

3.5 Membrane Fouling

One of the major limitations of membranes is the fouling phenomena. Membrane fouling is a process where particles are deposited on the membrane surface during filtration, so that the membranes performance is reduced. Fouling is defined as either reversible (can be removed by backwashing) or irreversible (only recoverable by chemical cleaning). The cause of reduction of flow rate through a membrane can be divided into two separate parts; concentration polarization and fouling. Concentration polarization is a consequence of the selectivity of the membrane and results in an accumulation of solutes or particles in the mass transfer boundary layer adjacent to the surface of the membrane. The dissolved molecules accumulated at the surface reduces the solvent activity and therefore reduces solvent flow through the membrane. The accumulation of solutes will result in a higher concentration at the membrane surface (C_m) than in the bulk feed (C_b), see figure 3.8. [15]

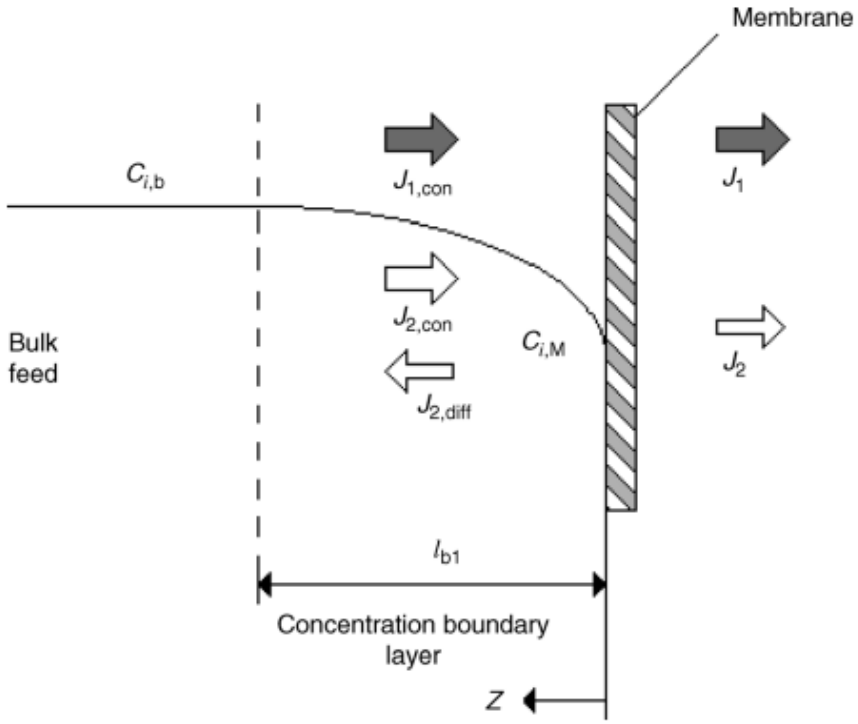

Figure 3.8: *An illustration of concentration polarization.*[15]

Besides concentration polarization there is fouling, which is an accumulation of particles on or in the membrane surface. There are the following forms of fouling[15]:

- Adsorption: This happens when there are interactions between the membrane and the solute/particles. If the adsorption degree is dependent on concentration, then concentration polarization will increase the adsorbed amount.

- Pore blockage: The blockage of pores can occur when filtering, resulting in a reduction in flux due to the closure/partial closure of pores.
- Deposition: This is commonly known as cake resistance. When filtering, the particles rejected can build up at the surface of the membrane (known as filter cake), and leads to additional hydraulic resistance.
- Gel formation: For some macromolecules, the concentration polarization can lead to gel formation at the membrane surface. An example of this could be a solution of concentrated proteins.

Fouling can therefore be defined as non-dissolved material that is either deposited on the membrane surface, or material that is blocking pores in the membrane. An illustration of fouling can be seen in figure 3.9.

Figure 3.9: *Illustration of three mechanisms that can cause fouling. (a) Adsorption, (b) pore blocking/plugging, (c) cake deposition*[15]

Fouling by particles relies on different factors; type of membrane used, membrane properties, nature and characteristics of the particles, such as size distributions, surface properties (hydrophilic/hydrophobic, zeta potential), the type of particles (organic/inorganic), and the mode of operation.[15] According to [11], the fouling and scaling problems are generally speaking as follows[11]:

- 50% Organic fouling
- 30% Colloidal fouling
- 20% Mineral scaling

The organic fouling consists of biofouling via natural organic matter (NOM), such as humic and fulvic acids along with potential organics added during pretreatment, namely coagulants and anti-scalants. Colloidal fouling is present in almost all membrane filtrations and is the most serious. It occurs if the amount of suspended solids in the feed stream is too high. Table 3.4 shows sources of membrane fouling and scaling.[11]

Fouling substances are often hydrophobic and carry a surface charge. Because of this, hydrophobic membranes are more susceptible to fouling than hydrophilic membranes. When fouling occurs, it is also harder to remove the adsorbed layer from a hydrophobic membrane. For example, during one test with NF membranes for the removal of NOM, the flux was reduced by 60% in the hydrophobic membrane and 20% in the hydrophilic. Hydrophilic surfaces

Table 3.4: Sources of membrane fouling and scaling

Substance	Extent and/or mechanism
Fe, Mn, Al hydroxides	Severe fouling, rapid kinetics
Mineral salts ($CaCO_3, CaSO_4, BaSO_4, SrSO_4$)	Form mineral scales when their solubility is exceeded
Colloids	Electrically charged; SDI (Silt Density Index) and zeta potential determine fouling
Microbiological	Forms a biofilm gel layer
Proteins	Fouling by hydrophobic and charge interactions
Polyelectrolytes	Fouling by charge interaction
Organic acids	Humic and fulvic acids cause severe fouling
Oil and grease	Hydrophobic membrane fouling
Suspended solids (Applicable to RO/NF)	Cannot exceed 0.5ppm

have hydrogen-bond acceptors, are electro-neutral and do not have hydrogen bond donors. Therefore these membranes are good at resisting protein adhesion. Membranes with these surface characteristics are also believed to bind a thin layer of water to the surface, thereby providing a steric or energetic barrier to adhesion.[11]

The surface charge of a membrane is indicated by the zeta potential and as previously mentioned, it is an indicator of fouling tendencies. Generally, membranes are modified to carry a negative charge, as NOM in water is negatively charged at neutral pH, due to the carboxylic and phenolic groups.[16]

Surface roughness is also important in terms of adhesion, as rougher surfaces increase the adhesion of substances to the membrane. For example, cellulose acetate (CA) membranes are more fouling resistant than polyamide (PA) membranes. This is due to CA membranes having a smoother surface and thus reducing fouling. As previously mentioned, PA TFC membranes are currently the most used NF membranes, but these membranes do not possess the anti-fouling properties discussed.[11]

3.6 Summary

Graphene oxide membranes made for filtering would be anisotropic TFC membranes. These membrane types consist of a very thin selective layer mounted on a microporous support. This support is important, as graphene oxide membranes have a pore size of 0.7 nm and 3-5 nm for a dry and fully wetted membrane, respectively. This means that graphene oxide membranes are in the RO/NF range, and as can be seen from table 3.3, these processes operate under significant pressure.

The intended use of the membrane is water treatment and as such, the membrane is expected to be fully wetted and therefore lie in the range of NF. This means that the transport mechanism for these membranes is described

by a combination of pore-flow and solution-diffusion.

Fouling of membranes is a major limitation of the process and is generally caused by organic fouling by NOM, colloidal fouling and mineral scaling. Fouling is dependent on membrane surface characteristics, and it has been shown that hydrophilic membranes with a negative surface charge have better fouling resistance, due to the fouling substances often being hydrophobic. A way to potentially change surface characteristics and make the membranes more hydrophilic is adding TiO_2, which will be described in the next chapter.

4 Titanium dioxide

Titanium dioxide (TiO_2) is the naturally occurring oxide of titanium, it has a lot of uses like paints and sunscreen, when used as a pigment it is called titanium white. For this project the photocatalytic abilities of the TiO_2 anatase crystal structure, when exposed to UV light are of interest. It can generate superhydrophillic surface properties [17] and oxidize water which creates hydroxyl radicals[18]. Hydroxyl radicals are often used for degrading pollutants, breaking these pollutants into smaller molecules.

TiO_2 is found in 3 major crystalline structures: anatase, rutile and brookite (see figure 4.1).

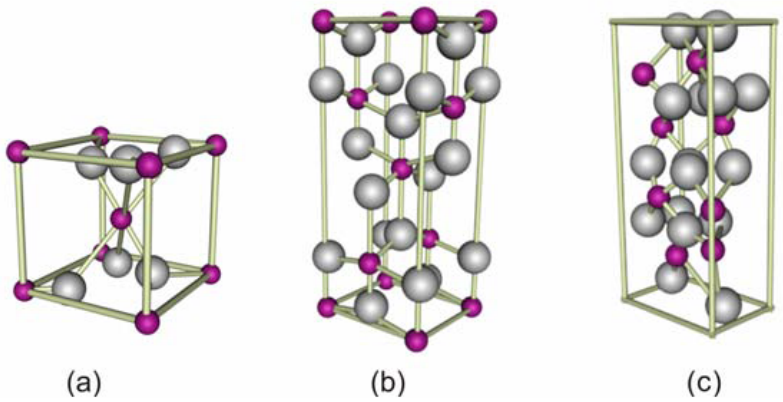

Figure 4.1: *The three crystalline structures of TiO_2, (a) anatase, (b) rutile and (c) brookite*[19]

Anatase and rutile play the biggest roles in TiO_2 applications, both these structures have a basic building block consisting of a titanium atom surrounded by six oxygen atoms in a distorted octahedral configuration. In both structures, the two bonds between the titanium and oxygen atoms at the aspices of the octahedron are slightly longer. In the anatase a sizeable deviation from a 90° bond angle, in rutile the neighboring octahedral share one corner along the $\langle 110 \rangle$ directions, and are stacked with their long axis alternating by 90°. In anatase the corner sharing octahedra form $\langle 001 \rangle$ planes, the edges are connected with the plane of the octahedra below, see figure4.2. [20]

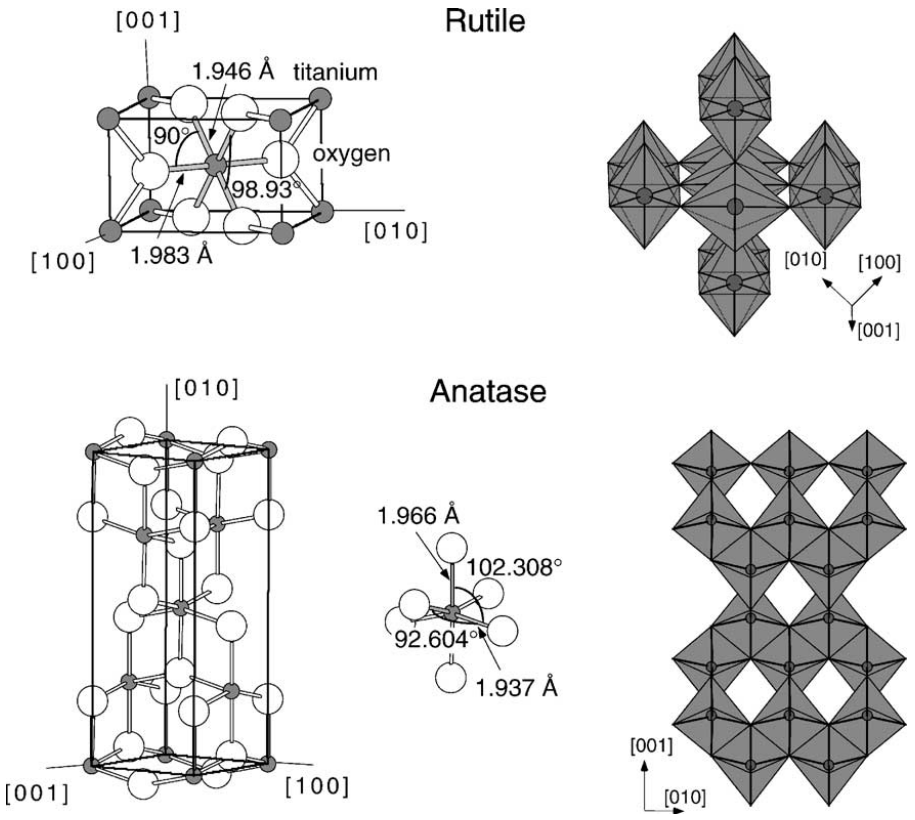

Figure 4.2: *Bulk structures of anatase and rutile, the rutile unit cell has the dimensions: a=b=4.587Å, c=2.953Å. The dimensions of the anatase is a=b=3.782Å, c=9.502Å. Both structures have a slightly distorted octahedral as basic unit. The bond lengths and angles of the octahedral coordinated Ti atoms are indicated and the stacking of the of the octahedral is also shown.*[20]

4.1 Photocatalytic Oxidation

The photoactivity of TiO_2 is a very attractive property, it originates from the initial step in photocatalysis, where an electron-hole pair is generated by light activation. The electron-hole pair generated can participate in different redox reactions like the creation of hydroxyl radicals, which is used in water treatment for degrading organic compounds.[17]

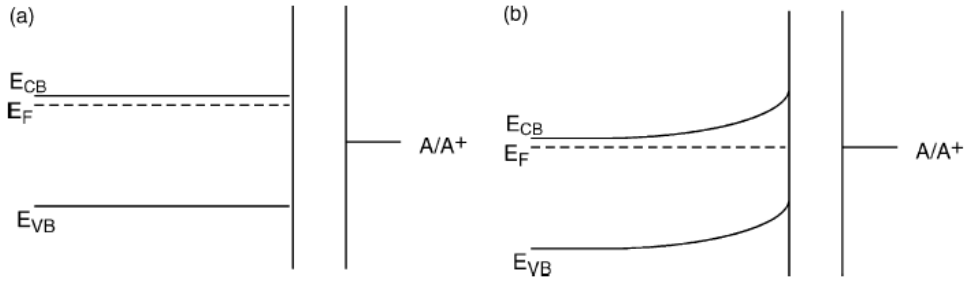

Figure 4.3: *Band structure in an n-type semiconductor, (a) before contact with an electrolyte and (b) in contact with an electrolyte.* [20]

The result of the primary excitation process is an electron in the conduction band and a hole in the valence band (figure 4.3a, equation 4.1). When in contact with an electrolyte, the chemical potential equilibrates with the redox potential of the redox couple. The formed potential energy barrier (figure 4.3b) drives the electron and the hole in different directions. The components of the electron-hole pair are capable of reducing and oxidizing an adsorbate, effectively forming a oxidized electron donor and a reduced electron acceptor (equation 4.2-4.6) [20]

$$TiO_2 + hv \rightarrow TiO_2(e^-, h^+) \tag{4.1}$$
$$TiO_2(h^+) + RX_{ads} \rightarrow TiO_2 + RX^{\bullet +}_{ads} \tag{4.2}$$
$$TiO_2(h^+) + H_2O_{ads} \rightarrow TiO_2 + OH^{\bullet}_{ads} + H^+ \tag{4.3}$$
$$TiO_2(h^+) + OH^-_{ads} \rightarrow TiO_2 + OH^{\bullet}_{ads} \tag{4.4}$$
$$TiO_2(e^-) + O_{2,ads} \rightarrow TiO_2 + O_2^{\bullet -} \tag{4.5}$$
$$TiO_2(e^-) + H_2O_{2,ads} \rightarrow TiO_2 + OH^- + OH^{\bullet}_{ads} \tag{4.6}$$

The result of these process is radicals which has the possiblity to undergo further reactions. Hydroxyl radicals are known as one of the important radicals in photocatalytic degradation of organics. [20]

The band gap of TiO_2 anatase is $3,2eV$ (see figure 4.4, meaning the required energy to create these photocatalytic reactions corresponds to light with a wavelength of 388nm, which lies in the UV region. It is possible to dope TiO_2 with for example Nitrogen, changing the energy needed to activate the photocatalytic abilities to the visible light spectrum. [17]

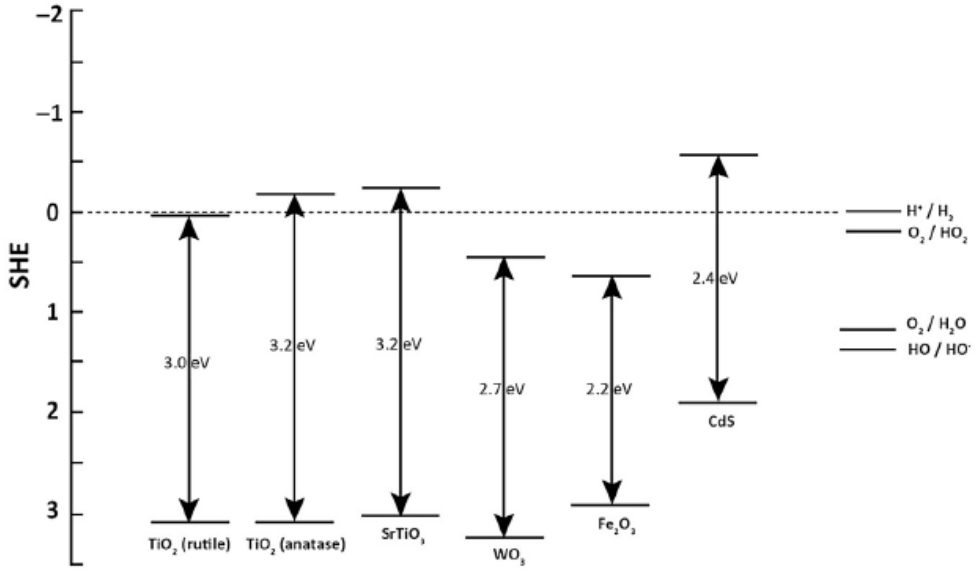

Figure 4.4: *Band edges for various semiconductors vs standard hydrogen electrode (SHE) at pH 0.*[17]

4.2 Photoinduced Superhydrophilicity

UV radiation can generate superhydrophilicity, one of the models explaining this is based on surface structural changes, while another model simply suggests the superhydrophilicity is caused by removal of surface organics, which makes it related to photocatalytic oxidation.[17]

XPS analysis of TiO_2 solgel films have shown that UV light activation yields a higher concentration of hydroxyl groups on the surface. The XPS spectra (figure 4.5) show the O 1s peak, the peak have been deconvoluted into 2 peaks, corresponding to the $Ti-O$ bond at $529,9eV$ and the $Ti-OH$ bond at $531,9eV$. The spectra shows the difference in pure TiO_2 solgel film and film exposed to UVC light for 1 hour, the UV exposure reveals that the hydroxyl group peak rises, indicating that chemical water adsorption on the surface is enhanced. [17]

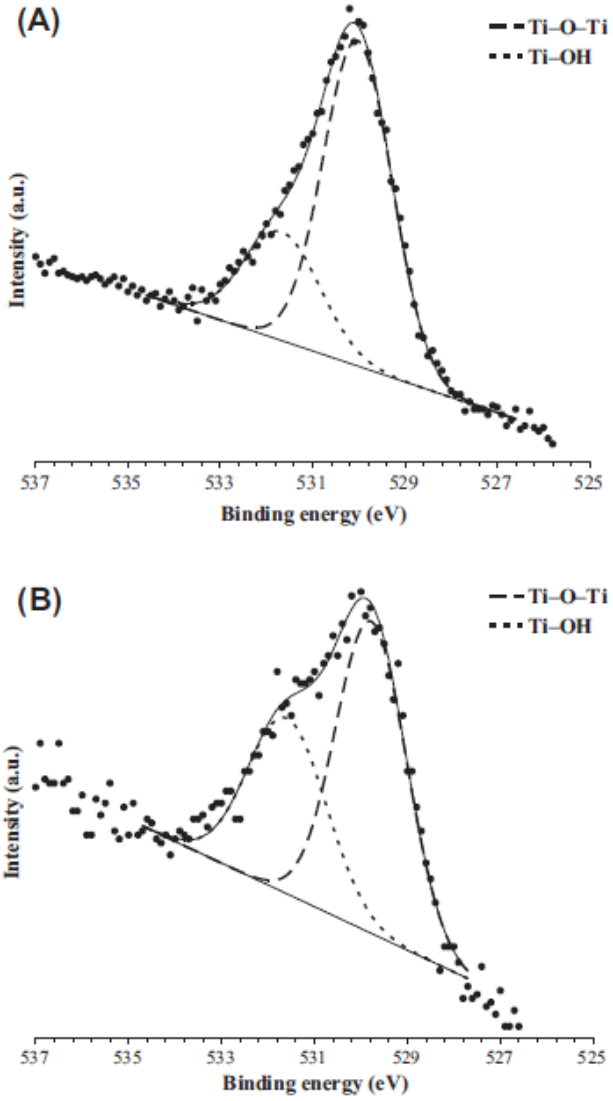

Figure 4.5: *O 1s spectra from XPS analysis of solfel films, (A) before UV radiation, (B) after UV radiation. Both samples were radiated with UVC light with an intensity of* $10\frac{mW}{cm^2}$.[17]

The superhydrophyllic state does not change when further exposed to UV light, but if stored in a dark place, the surface state does revert back to its original state. And studies have shown that the amount of OH groups at the surface influence the photocatalytic activity, meaning that it might be linked to the superhydrophyllic state. The increased amount of OH groups at the surface means more groups which can be photoactivated and generate hydroxyl radicals. [17]

5 Thesis Statement

In the previous chapters, the theory behind GO and their use as membranes were investigated. Based on the theory, GO is believed to be an excellent material for water-treatment membranes due to its hydrophilic nature. One major limitation of membrane usage is the fouling phenomena, which was found to be dependent on surface characteristics; membranes with higher hydrophilicity were found to have better fouling resistance. This is where the potential use for TiO_2 arises, as it has gained increasing popularity for usage in surface cleansing. When TiO_2 is irradiated with UV-light it creates free radicals which could break down fouling particles, while also creating hydroxyl groups on the surface, thus making the material more hydrophilic creating a superhydrophilic state. While it is hypothesized that the free radicals could break down fouling particles, it is also a possibility that the membrane material could be degraded from the free radicals. The project aims to find the best synthesis of GO and use the material obtained to create membranes. The TiO_2 will then be added in hopes of producing stable membranes with anti-fouling properties. The laboratory work in this project will be based on the theory previously described and will be trial and error, in hopes of developing stable, fouling-resistant membranes:

- Which method for synthesizing GO is ideal to use for experiments: Hummers, Modified Hummers or Tours?
- What is the ideal thermal treatment of GO membranes for creating stable membranes?
- What are the optimal ratios of GO/TiO_2 for creating stable membranes?
- Will the TiO_2 be able to change surface characteristics and provide anti-fouling properties? Does UV-treatment break down the membrane material?
- What is the permeance of the membranes? Do they block water or is the permeation unimpeded?

6 Characterization

This chapter will give the reader sufficient knowledge about the intended characterization methods for characterizing the membranes produced in this project.

6.1 FTIR and Raman spectroscopy

FT-IR (Fourier transform infrared spectroscopy) and Raman spectroscopy are two different ways of analyzing materials, but they compliment each other well. FT-IR measures absorbency of light caused by molecule vibrations, where Raman measures scattering of light by the vibrating molecules, see figure 6.1. Generally strong bands in FT-IR spectras corresponds to weak bands in Raman and the other way around, which is why they compliment each other well. [21]

The main reason they compliment each other is because of the electrical characteristics of the vibrations, a strong polarized bond like $C-O$, $N-O$ or $O-H$ will only have a small effect on polarisation, resulting in weak scattering giving weak Raman peaks. The same bonds will however perform vibrational movements resulting in strong FT-IR peaks. Neutral bonds like $C-C$, $C-H$ and $C=C$ changes alot when polarized producing strong Raman scatterers, but weak FT-IR results.[21]

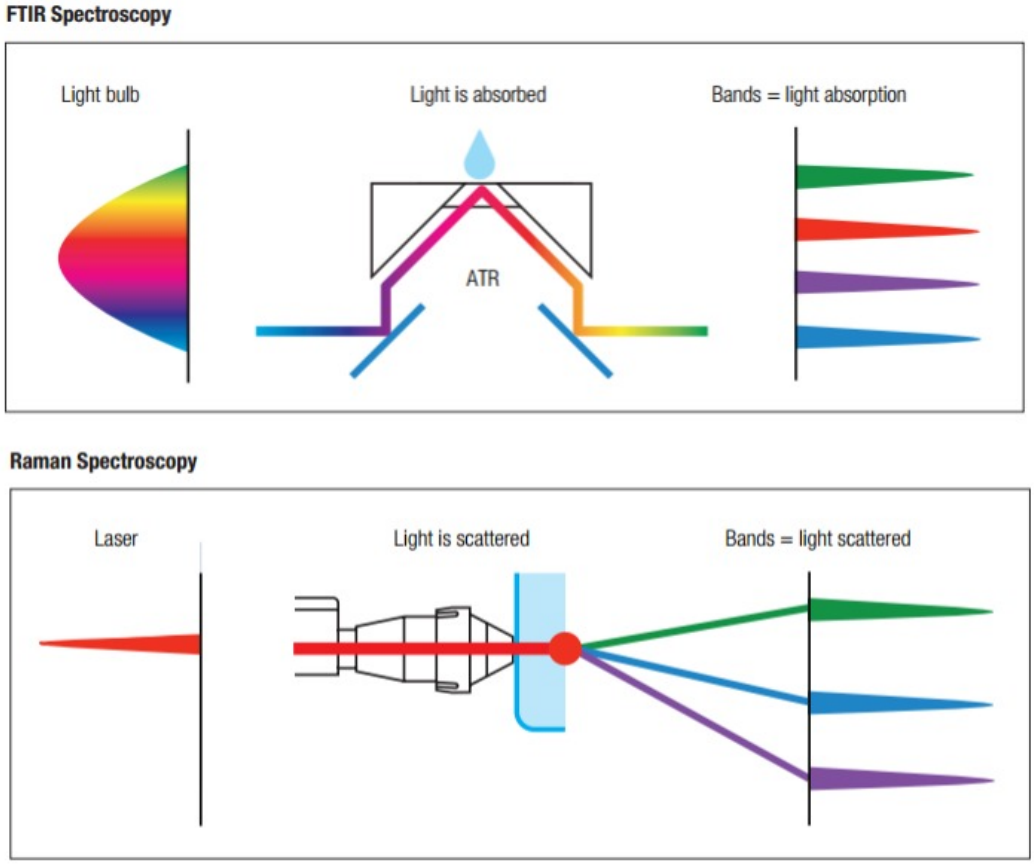

Figure 6.1: *Comparison of how measurements are performed with FT-IR and Raman spectroscopy.*[22]

6.2 X-ray Diffraction

Bragg's diffraction occurs when a sample is irradiated with X-rays, and they are scattered in a specific way causing constructive interference. For a solid the waves are scattered from lattice planes separated by interplanar distance d, when these scattered waves interfere constructively the difference between length of the waves is equal to n multiplied by the wavelength (λ). The path difference between two waves causing interference is defined as $2d\sin\theta$, where θ is the scattering angle. This definition is known as Bragg's law: $2d\sin\theta = n\lambda$, see figure 6.2 [23]

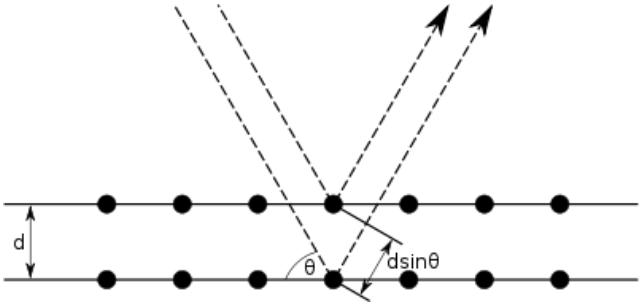

Figure 6.2: *Bragg diffraction, two identical beams hits the solids and are scattered off two different atoms. The lower beam travels an extra length of* $2d\sin\theta$*, when this length is equal to* $n \times \lambda$ *constructive interference occurs*[23]

The intensity of the constructive interference can be plotted as a function of the scattering angle, for graphene oxide the results of this plot contains valuable information about the space between the layers (d_{002}), which can be calculated using Braggs law. The thickness of the stacking layers can be calculated using the Scherrer equation:

$$D_{002} = \frac{K\lambda}{\beta\cos\theta}$$

D_{002} is the thickness of the layers. K is the Warren shape constant which varies from 0.89 for spherical to 0.94 for cubic particles. Usually, this is set to 0.9 for particles of unknown size. λ is the wavelength of the X-rays. β is the full width of the at half the maximum intensity (FWHM). θ is the Bragg angle.

From the Scherrer equation the number of layers can be obtained using the following equation:

$$N_{layers} = D_{002}/d_{002}$$

6.3 Zeta potential

Zeta potential is electrokinetic potential, it is denoted using the greek letter zeta (ζ), and its a measure of the charge at the diffuse outer layer of ions on a molecule see figure 6.3. A common way to influence the zeta potential is by changing the pH, which causes ionization of the surface groups, this ionization changes the zeta potential. When the zetapotential is 0, it is known as the isoelectrical point, at this point the charge of the surface is 0. [24]

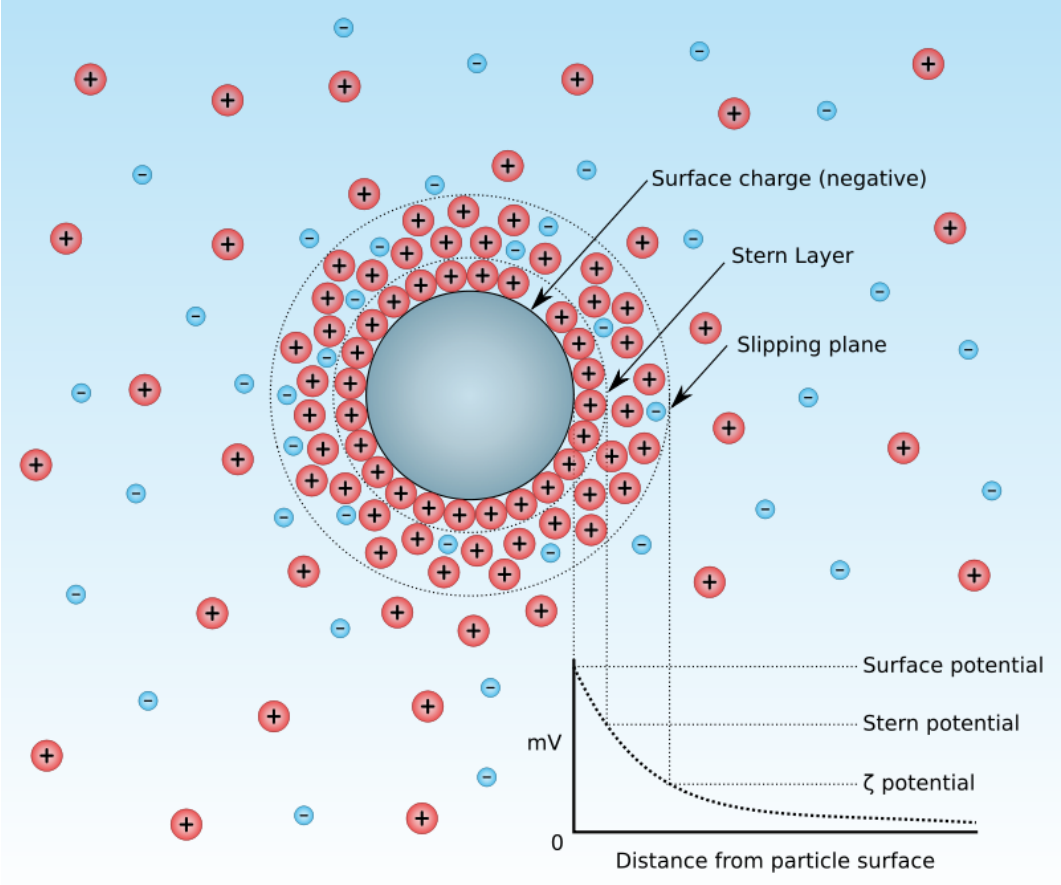

Figure 6.3: *Diagram showing the ionic concentration and potential difference as a function of distance from the charged surface of a particle suspended in a dispersion medium.*[25]

For membranes measuring the streaming potential is a method to characterize the zeta potential of its surface. This is done by used polarisable electrodes set perpendicular to the flow direction. An electrolyte is pumped through a cell covered with the membrane, this setup can be seen on figure 6.4, the streaming potential in these cells are calculated using the following equation:

$$\zeta = \frac{dl}{dp} \times \frac{\eta}{\varepsilon \times \varepsilon_0} \times \frac{L}{A}$$

Where:
$\frac{dl}{dp}$ is the slope of the streaming current vs. the differential pressure
η is the viscosity of the electrolyte
ε is the dielectric coefficient of the electrolyte
ε_0 is vacuum permittivity
L is the length of the streaming channel
A is the cross-section of the streaming channel

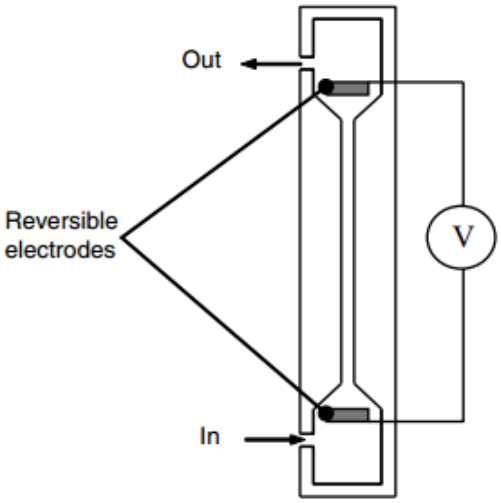

Figure 6.4: *Experimental setup for measuring zeta potential of a membrane.*[24]

6.4 DSA - Drop shape analysis

In order to examine the membrane surface characteristics, drop shape analysis is performed. The contact angles from water and diiodomethane were used to determine the dispersive and polar components of the membranes, allowing for calculation of the surface energy and surface polarity. When interpreting contact angles, there are 3 tensions acting in different directions, see figure 6.5.

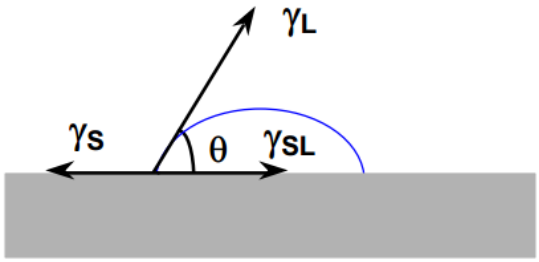

Figure 6.5: *The equilibrium balance of forces of a liquid drop on a solid surface.*[26]

The forces shown in figure 6.5 can be formulated into Young's equation:

$$\gamma_s = \gamma_{sl} + \gamma_l \cos\theta$$

Where γ_s is the surface energy of the solid, γ_{sl} is the free energy associated with the liquid/solid interface, and γ_l is the free energy associated with the air/liquid interface. The liquid/solid interfacial energy (γ_{sl}) can be described by Good's equation [26]:

$$\gamma_{sl} = \gamma_s + \gamma_l - \left[\left(\gamma_s^D \gamma_l^D\right)^{\frac{1}{2}} + \left(\gamma_s^P \gamma_l^P\right)^{\frac{1}{2}}\right]$$

Where:
γ_l = overall surface tension of the liquid
γ_l^D = dispersive component of surface tension for the liquid
γ_l^P = polar component of surface tension for the liquid
γ_s = overall surface tension of the solid
γ_s^D = dispersive component of surface tension for the solid
γ_s^P = polar component of surface tension for the solid

Good's equation can be combined with Young's equation and be used to determine the polar and dispersive components of both liquids and solids[26]:

$$\left(\gamma_s^D \gamma_l^D\right)^{\frac{1}{2}} + \left(\gamma_s^P \gamma_l^P\right)^{\frac{1}{2}} = \gamma_l \frac{\cos(\theta + 1)}{2}$$

The equation holds two unknowns, namely γ_s^D and γ_s^P. Because diiodomethane only has a dispersive component, the equation can be further reduced:

$$\gamma_s^D = \frac{\gamma_l}{4} (\cos\theta + 1)^2$$

This allows us to obtain γ_s^D and thus to solve the aforementioned equation for γ_s^P. The surface energy is then calculated by adding γ_s^P and γ_s^D. The surface polarity, a measure of polar component versus surface energy, is then calculated:

$$Surface\ polarity\ (solid) = 100\% \times \frac{\gamma_s^P}{\gamma_s}$$

6.5 Scanning Electron Microscopy

Scanning Electron Microscopy (SEM) scans the surface of a sample with beams of electrons, the signals obtained from the electrons interacting with the atoms in the sample are gathered, they contain information about the topography and composition of the surface. The setup of a microscope is made up of a few crucial components:

- Electron gun: capable of emitting electron beams.
- Various lenses: used to produce clear and detailed images.
- Sample chamber: chamber for samples to be analyzed.
- Detectors: the "eyes" of the microscope, detecting the ways the beams interact with the sample.

- Vacuum chamber: SEM requires vacuum to operate, to eliminate interference between the electron beams and air particles.

The setup can be seen on figure 6.6. [27] [28]

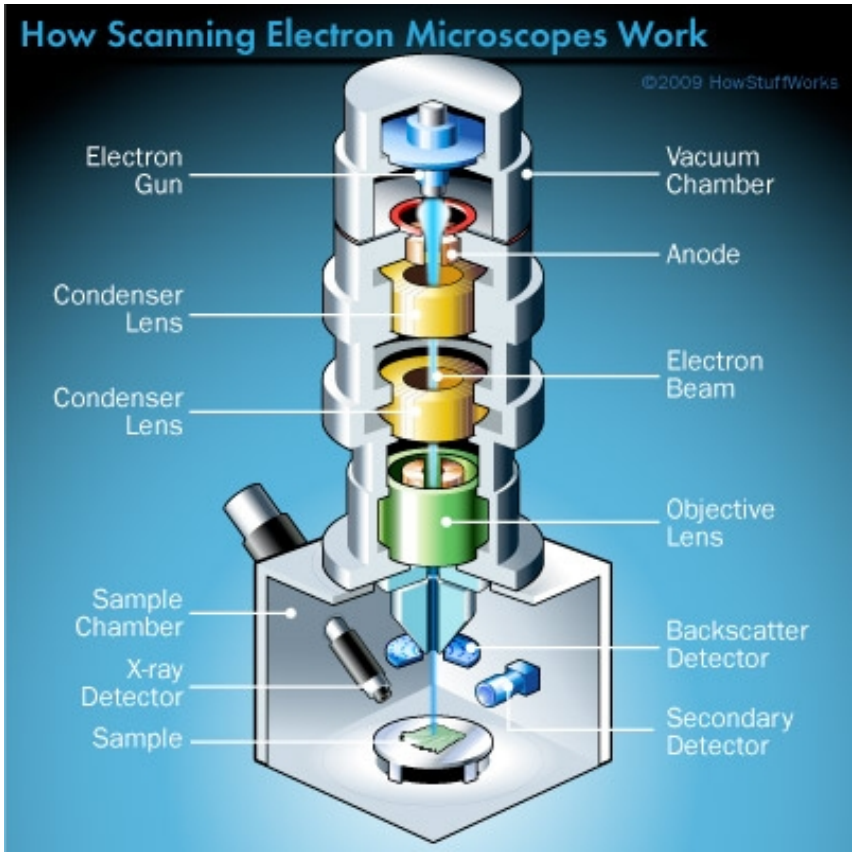

Figure 6.6: *Setup of a Scanning Electron Microscope [28]*

An addition to the microscope can be made with Energy-Dispersive X-ray Spectroscopy (EDS), providing elemental analysis or chemical characterization of a sample. It relies on X-ray excitation, since each element has a unique atomic structure they will have unique peaks on a X-ray emission spectrum. The cause for this is when the primary electrons (PE) hit the orbital electrons of the atoms, they will either ionize the atom or promote the orbital electrons to a higher energy level. If the orbital electron is promoted to a higher energy level, it will emit a X-ray emission spectrum unique to this element, these emissions are specific to which electron shell was filled, see figure 6.7. [29][30]

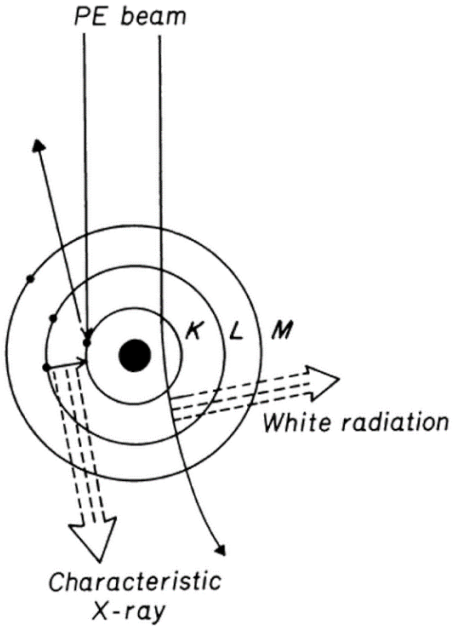

Figure 6.7: *Atom model when exposed to an electron beam. [30]*

This gives information of the elements found in the sample, combining this with SEM it is possible to do a mapping of the surface, creating images showing where the different elements are present on the surface. An example of this mapping can be seen on figure 6.8, the image analyzed is shown (top left), along with images showing the intensity of the elements found on the surface. [29]

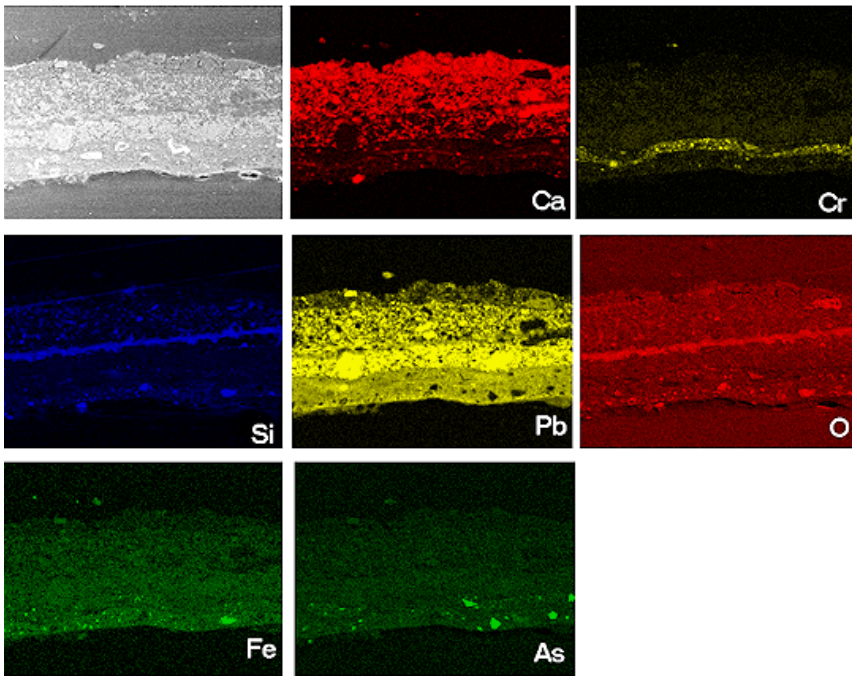

Figure 6.8: *An image of SEM-EDS mapping [31]*

6.6 Tensile test

The tensile test is a standard test for testing strengths of a material, this test will be done to test the overall strength of the membrane material produced. If the material is fairly weak, strengthening or mounting it on a different surface to provide extra strength might be needed.

For testing the tensile strength, a piece of the material is mounted in 2 clamping cells, one which is fixed and one capable of moving. The tension of the material is then measured as the moving part starts to pull the material apart, providing a stress/strain diagram of the matrial.

6.7 Water Vapor Transmission

In order to examine the permeation of the GO membranes produced, tests with water, ethanol and hexane were performed. Water is expected to permeate the membranes unimpeded due to its' polarity, as described in theory section 2.6. Ethanol as a molecule can be said to be both polar and non-polar; it possesses a polar end because of the hydroxyl group, while the ethyl group is non-polar. It is therefore expected that only small amounts of ethanol will pass through the membranes, if any. Hexane as a pure hydrocarbon cannot donate or accept hydrogen bonds and is therefore non-polar. Therefore, hexane should not be able to permeate the GO membranes. Using water, ethanol and hexane we get an idea of how the membrane performs with different types of molecules; water is polar, ethanol is an intermediate (both polar and non-polar), and hexane is non-polar. Furthermore, the The GO membranes will be characterized and compared to two commercial membranes (Alfa Laval NFT99HF and NFT50), in order to compare them in terms of WVT and permeance. The WVT will be calculated using the following equation:

$$WVT = \frac{w_0 - w_s}{t \times A}$$

Where w_0 is the start weight, w_s is the weight at the end of the experiment. T is the elapsed time and A is the section area of the glas tube used. The permeance is then calculated using the following equation:

$$Permeance = \frac{WVT}{P_s(R_1 - R_2)}$$

Where P_s is the saturation vapour pressure, R_1 is the relative humidity inside the tube, R_2 is the relative humidity outside the tube. While the saturation vapour pressure was found in thermodynamic tables with water, Antoine's equation was used to calculate the saturation vapour pressure with hexane and ethanol:

$$P_s = 10^{A - \frac{B}{C+T}}$$

Where A, B and C are Antoine equation parameters and T is the temperature in $°C$. An example of calculations can be seen in appendix A.4.

7 Experimental design

The synthesis of graphene oxide was tested with different methods and the best method was then chosen for later experiments. The synthesis of TiO_2 will also be explained while also explaining the initial tests that led to the final mixtures of GO/TiO_2 along with optimal reduction temperature. For characterizing the membranes produced, the methods described in chapter 6 will be used.

In order to see how the produced membranes performed compared to commercially available membranes, we tested 2 Alfa Laval membranes (NF99HF and NFT50). Both membranes are nanofiltration membranes, with an active polyamid layer for use in water filtration.

7.1 Graphene oxide synthesis

This section will describe the different methods used for graphene oxide synthesis; Hummer's method, Modified Hummer's and the Tour method. The Tour's method was ultimately chosen for several reasons; the Hummer's and Modified Hummer's methods are both time consuming and require several hours of work in the lab, while also possessing more steps and hence a larger margin of error. As it is described in chapter 2 (figure 2.4), the Tour method also has little leftover unoxidized graphite compared to the latter, which is also of significant importance. The tour method is described in further detail with pictures in Appendix A.1.

7.1.1 Hummer's method

The first method tested was the well known Hummer's method. The stepwise synthesis is as follows [32]:

1. Graphite flakes (2g) and $NaNO_3$ (2g) were mixed in 50 mL of H_2SO_4 (98%) in a 1000 mL volumetric flask kept under an ice bath ($0 - 5°C$) with continuous stirring

2. The mixture was stirred for 2 hours at this temperature and $KMnO_4$ (6 g) was added to the suspension very slowly. The rate of addition was carefully controlled to keep the reaction temperature lower than $15°C$.

3. The ice bath was then removed, and the mixture was stirred at $35°C$ until it became pasty brownish and kept under stirring for 2 days.

4. It is then diluted with slow addition of 100 mL water. The reaction temperature was rapidly increased to $98°C$ with effervescence, and the color changed to brown color.

5. Further this solution was diluted by adding additional 200 mL of water stirred continuously.

6. The solution is finally treated with 10 mL H2O2 (30%) to terminate the reaction. The solution will get a yellow color when enough H_2O_2 is added.

7. The solution was then diluted with water in order to sediment GO particles, followed by decanting.

8. For purification, the mixture was washed by rinsing several times with 1 M HCl and then deionized water under centrifugation at 6000 RPM.

9. After filtration a stock solution was made of the cleansed GO.

7.1.2 Modified Hummer's method

This method of synthesis involves both oxidation and exfoliation of graphite sheets due to thermal treatment of solution. The stepwise synthesis is as follows[32]:

1. Graphite flakes (2 g) and $NaNO_3$ (2 g) were mixed in 90 mL of H_2SO_4 (98%) in a 1000 mL volumetric flask kept under an ice bath $(0 - 5°C)$ with continuous stirring

2. The mixture was stirred for 4 hours at this temperature and potassium permanganate (12 g) was added to the suspension very slowly. The rate of addition was carefully controlled to keep the reaction temperature lower than $15°C$.

3. The mixture is diluted with very slow addition of 184 mL water and kept under stirring for 2 hours. The ice bath was then removed, and the mixture was stirred at $35°C$ for 2 hours.

4. This mixture is kept in a reflux system at $98°C$ for 10-15 min. After 10 min, the temperature was changed to $30°C$ and results in a brown colored solution.

5. Again after 10 min the temperature is changed to $25°C$ and maintained for 2 hours.

6. The solution is then treated with 40 mL H_2O_2 (30%) which changes the solution color from brown to yellow.

7. The solution is then diluted with water and GO particles are allowed to settle before decanting the solution.

8. For purification, the mixture was washed by rinsing several times with 1 M HCl and then deionized water under centrifugation at 6000 RPM.

9. After centrifugation a stock solution was made of the cleansed GO.

7.1.3 Tour's method

The Tour's method is a further improved synthesis which uses a 9:1 mixture of concentrated H_2SO_4/H_3PO_4 and a 6:1 mixture of $KMnO_4/Graphite$. The synthesis is as follows [6]:

1. Concentrated H_2SO_4/H_3PO_4 (360:40 mL) was added to a 1000 mL volumetric flask containing graphite flakes (3 g) and $KMnO_4$ (18 g), producing a slightly exothermic reaction ($35 - 40°C$).

2. The solution was then heated to $50°C$ and stirred for 12 hours.

3. The solution was then cooled to room temperature in an ice bath, and 400 mL of water was slowly added to the reaction, keeping the temperature below $60°C$. The synthesis is then terminated using approximately 3 mL H_2O_2 (30%).

4. In order to speed up precipitation, the solution is then divided evenly into two beakers and deionized water is added. When the GO has precipitated, the solutions are decanted.

5. The solution is then rinsed with 1 M HCl and deionized water several times under centrifugation.

6. After centrifugation a stock solution was made of the cleansed GO. The stock solution was approximately 200 mL every time.

The w/w% of the Tour stock solution was: 2,1%

7.1.4 Initial tests with GO

Initially it was the intent to obtain a GO powder, but this required vacuum drying it and did not yield the powder wanted. It was also attempted to dry the GO as one big piece and mortar it, but it was not possible to grind it to powder. The decision was therefore made to make a stock solution with a fixed volume of 200 mL per batch and the w/w percentage was tested in an oven at $100°C$, weighing the sample before and after one hour. The next step was finding the best method for producing homogenous membranes. It was attempted to produce membranes by vacuum filtration using a Whatman 47 mm diameter filter with 0,2 μm pores. This method was however discarded as it took 2-3 days to produce one membrane. After this it was decided to use

petri dishes for the drying process. The amount of stock GO would be weighed on a petri dish and subsequently be placed in an oven at 80, 50, and 40°C. In all attempts the membranes became burned and ripped with holes, so finally it was decided to let the membranes dry at room temperature under a fume hood, producing pristine membranes as seen on figure 7.1.

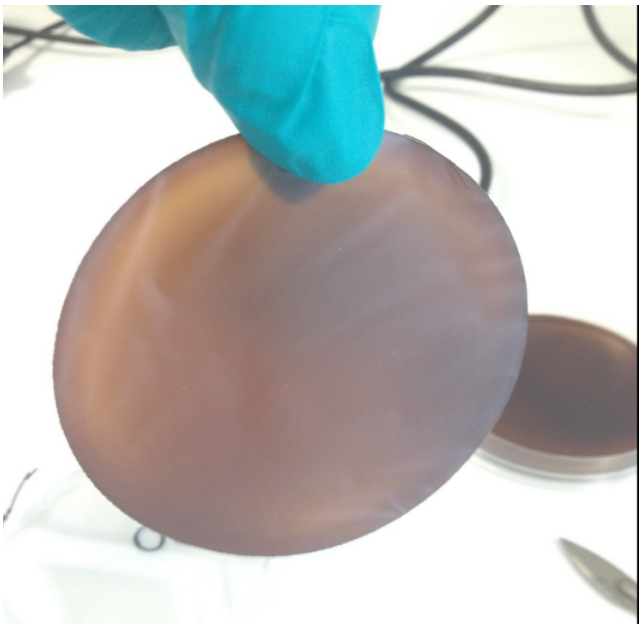

Figure 7.1: *Pristine GO membrane dried in a petri dish at room temperature.*

After doing several tests it was found that the best membranes were produced with 10 g of stock solution, as the thinner membranes at e.g. 7,5 g were too fragile when handled.

7.2 Titanium dioxide synthesis

The TiO_2 particles were obtained using a microwave assisted sol-gel process which produces nanosized TiO_2 particles, it is possible to tweak these parameters creating TiO_2 particles of different sizes. The method is as follows:

1. 25 mL titanium-(IV)-isopropoxide (TTIP) was added into 5 mL glacial acetic acid. The TTIP is carefully injected below the surface of the glacial acetic acid using a pipette.

2. This solution is then slowly added to a solution of 150 mL 0,1 M nitric acid. The solution of nitric acid is under rigorous stirring and the TTIP/glacial acetic acid solution is slowly added in the center of the swirl.

3. Afterwards, if the TTIP is not fully dissolved in the nitric acid, the solution is kept under stirring for 1-2 days until fully dissolved.

4. The precursor solution was then placed in a microwave reactor (Anton Paar, Multiwave 3000 (Frequency 2.45 GHz)) in order to control the sol-gel synthesis.

5. The synthesis used a temperature ramp to reach the final temperature of 220°C and pressure of 60 bar. The ramp was set to 30 min and the final temperature and pressure were also held for 30 min before cooling down.

6. After synthesis, the particles were redispersed using ultrasound and the resulting solution is the stock solution containing TiO_2 particles in the nanometer range.

The w/w% of the TiO_2 stock solution was: 3,6%

Figure 7.2: *On the left is the precursor and on the right is the stock TiO_2 solution*

7.3 Initial tests with GO/TiO_2

In order to find an optimal ratio of $GO/TiO2$ for the final experiments, several ratios were tested. The first test done with GO and TiO_2 was in a 3:1 ratio (75:25 mL) and resulted in a mayonnaise-like thick gel as seen on figure 7.3.

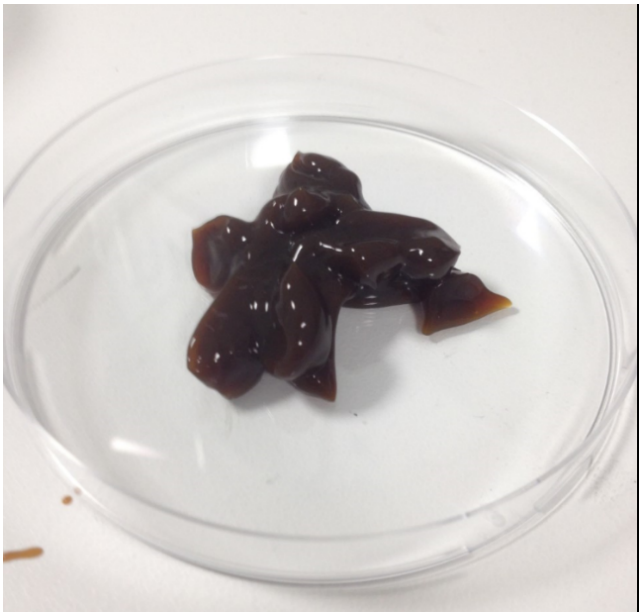

Figure 7.3: *GO and TiO_2 in a 3:1 ratio, giving a thick gel.*

Lumps of the gel were dried to see if the mixture could possibly form a material and some of the gel was diluted in order to spread it evenly across a petri dish, see figure 7.4.

Figure 7.4: *GO/TiO_2 membrane with a ratio of 3:1 after drying.*

The test membranes seemed to be homogenous, but all of the membranes cracked upon drying and were very crisp. Several mixture ratios were tried afterwards and this led to the following mixtures to be used for further tests:

- Mixture 1: 2 mL TiO_2 + 40 g GO (1:20 ratio) + approx. 15 mL H_2O

- Mixture 2: 6 mL TiO_2 + 40 g GO (3:20 ratio) + approx. 60 mL H_2O
- Mixture 3: 10 mL TiO_2 + 40 g GO (5:20 ratio) + approx. 80 mL H_2O
- Mixture 4: 10 g GO

In all the mixtures it was necessary to add water in order obtain a solution thin enough to distribute across a petri dish. As one would expect, the amount of water needed to make it sufficiently thin increased with higher TiO_2 content. According to figure 2.11 on page 13, reduction of the functional groups in graphene oxide begins around 180°C. It was therefore decided to reduce each mixture at 200, 250 and 300°C for 3 hours under nitrogen purge.

Figure 7.5: *From left to right; mixture 1, 2 and 3 reduced at* 300°C

The membranes had minor tears in them before reduction, but there was enough material for further tests. This batch of membranes were reduced in another lab and had to undergo shipment. They were all so fragile that the membranes of all temperatures disintegrated during shipment and when handled, see figure 7.5. After this more ratio tests were done in order to produce a more stable membrane and this led to an important observation; the tests done were with 10 g GO and this seemed to have an impact on the viscosity of the mixtures, as opposed to using 40 g. Further testing with 10 g GO led to the final mixtures being used:

- A: 0,667 mL TiO_2 + 10 g GO (1:15 ratio)
- B: 0,5 mL TiO_2 + 10 g GO (1:20 ratio)
- C: 0,334 mL TiO_2 + 10 g GO (1:30 ratio)
- D: 10 g GO

The A mixture is just thin enough to be able to spread out on a petri dish, while mixture B and C are easily spread out.

7.3.1 Thermal reduction

While initial reduction tests were carried out in another laboratory, the thermal reduction of the remaining membranes were done in a smaller cylindrical oven (Carbolite model 201). Like previously, reduction was done with nitrogen purge. The temperature chosen for thermal reduction was 140, 180, and 220°C for 3 hours. When using the cylindrical oven it was necessary to stack the membranes on top of each other in tight space, and it is speculated that this was the main reason why several batches continuously exploded when going above 150°C. In all but one of the explosions, the membranes would disintegrate into fine powder and the pressure would pop the sealing corks out of the oven. The leftover debris of a membrane not completely disintegrated can be seen in figure 7.6.

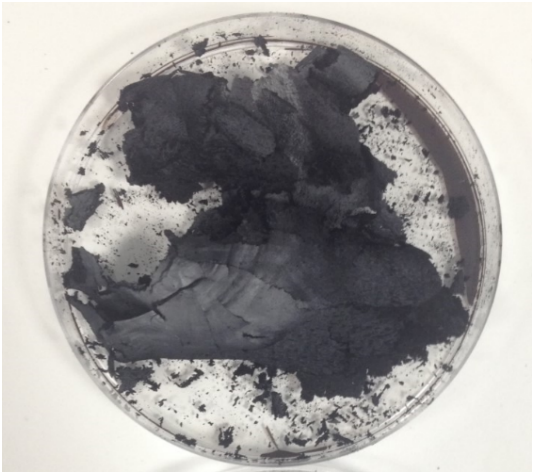

Figure 7.6: *The leftover debris of a B membrane after exploding during reduction.*

The heating rate first used was $\frac{10°C}{min}$ and this caused an explosion around $160 - 180°C$. The heating rate was then adjusted to $\frac{5°C}{min}$ and when heating up to 180 or 220°C, the heating was stopped for 5 minutes at 140°C and the heating rate was adjusted to $\frac{2{,}5°C}{min}$. The reduction at 3 hours produced fragile membranes even at 140°C and the reduction time was therefore adjusted to 1 hour instead. The membranes at 180 and 220°C still became very fragile even at 1 hour reduction, while the membranes reduced at 140°C were easily handled without damaging them. The membranes also could not be reduced more than one at a time in the oven at 180 and 220°C. Following these tests, it was concluded that the membranes would be reduced for 1 hour at 120, 140 and 160°C. However, when measuring the zeta potential of the membranes from 120Â°C, they quickly disintegrated and filled the system and electrolyte solution with debris. The experiments therefore ended up being confined to 140 and 160Â°C.

In order to get a better understanding of the problem with the exploding material, a small experiment with crucibles for TGA was heated in the Car-

bolite oven. Different sample weights were tested to see how much was safe to reduce at once in a crucible, with the main goal of analyzing the reduction process with DSC and TGA without risking the graphene oxide to explode in the sensitive lab equipment. Different sample sizes were added to crucibles and heated to 220°C with a heating rate of $\frac{10°C}{min}$, the crucibles with 1, 2 and 4mg GO did not show explosive behavior, however a crucible with 7mg GO did show the explosive behavior, see figure 7.7.

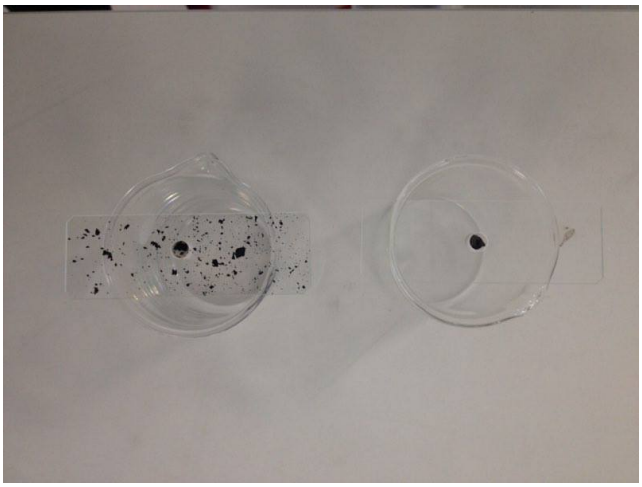

Figure 7.7: *To the left is a crucible with 7mg GO which exploded during the heating to* 220°C*, on the right is a crucible with 4mg GO which did not exploding when heated to* 220°C

This small experiment backs up the theory that the mass is a big factor behind the explosive behavior, if the mass is too big when thermally reducing it, the gasses aren't able to dissipate fast enough leading to runaway reaction culminating in an explosion. With a safe sample mass in a crucible, it was possible to test the graphene oxide reduction process with TGA and DCS without triggering the runaway reaction. The TGA and DSC measurements were performed using Mettler Toledo DSC822e and Mettler Toledo TGA/SDTA851e, heating the samples to 300°C with a heating rate of $\frac{10°C}{min}$.

7.4 IR-Spectroscopy and Raman

To test if the TiO_2 is creating a superhydrophilic surface when irradiated with UV-C light (254 nm), FT-IR spectra was gathered from membranes with and without UV-C light treatment for 30 minutes and a light intensity of $2\frac{mW}{cm^2}$. 10 FT-IR spectra were collected from each sample, the measurements were gathered using Thermo Scientific Nicolet iS5. The functional groups of interest are listed in table 7.1

To analyze the results SNV correction is applied, it is a preprocessing treatment to remove scatter; the average and standard deviation for the spectra is calculated, every data point is then subtracted from the mean and divided by the standard deviation. After the SNV correction the IR spectra were

Table 7.1: List of the important functional groups found in GO.

Functional group	Wavelength / $cm^{-}1$
O-H stretching	3412
C=O stretching vibration	1726
C=C sp^2 bonds	1624
O-C-O vibrations	1260
C-O vibrations	1087

evaluated using Principle Component Analysis (PCA), to determine possible patterns in the variance of the spectra.

For gathering the Raman spectra of the membranes a Kaiser RamanRxn1 with a MultiRxn Probe 785nm, was used, however the laser source used could not pick up any information as the membranes were too dark. A laser with a different wavelength would have to be used, which unfortunately was not available.

7.5 Zeta potential measurements

The measuring of zeta potential were performed using an Anton Paar SurPASS electrokinetic analyzer. For the measurements an adjustable gap cell was used see figure 7.8, the material to be tested will be taped to blue blocks which are then inserted into the cell. The blocks can be moved back and forth in the cell with knobs in order to achieve a distance of $100\mu m$, which is ideal distance for measurements. The cell is then inserted into the machine and 2 electrodes are attached to each end of the gap cell.

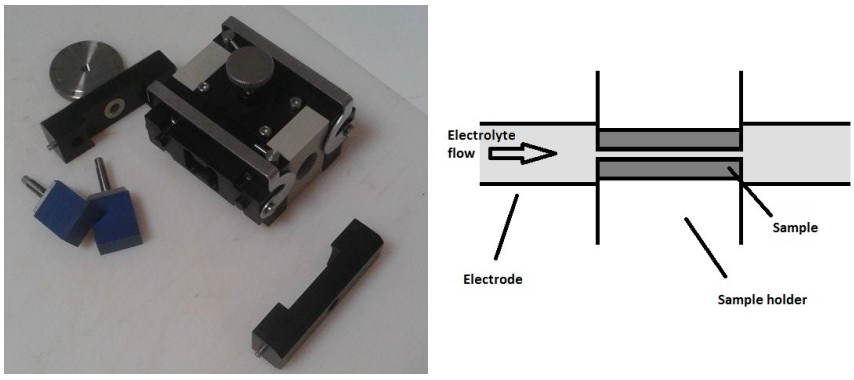

Figure 7.8: *Left: adjustable gap cell for measuring the zeta potential of membranes. Right: schematic showing how the gap cell works.*

The measurements were performed using an electrolyte solution with 0.1 KCl purged with nitrogen. For adjusting the pH levels of the measurements 0.1M $NaOH$ and 0.05M HCl was used. Distilled water were used for the electrolyte solution as well as the titrants.

The GO membranes were tested without UV radiation, and after being exposed to UV-C irradiation for 30 minutes, in order to determine if the UV radiation has any effect on the zeta potential.

7.6 Tensile test

For testing the tensile strength of the membranes a Lloyd Instruments LR50K Plus was used, however it was not possible to get any useful results, as the material proved too brittle to mount in the clamps.

7.7 DSA - Drop Shape Analysis

For measuring the contact angles of the membranes a Krüss DSA100 was used, the machine has 4 fixed syringes (water, diiodomethane, chloroform, ethyleneglycol) capable of depositing identically drops of a specific volume each time. Only measurements using water and diiodomethane were performed, water using droplets of $3\mu l$ and diiodomethane using droplets of $1\mu l$. Each measurement was performed 5 times, and the average value was used.

For testing the UV effect on the contact angle, the membranes were exposed to UV-C light with an intensity of $2\frac{mW}{cm^2}$ with different exposure time (5, 10, 15, 20 and 30 minutes). This test was performed to test how much exposure is needed to reach the maximum effect.

A similar test was done exposing a B membrane reduced at $140°C$ to UV-C light for 30 minutes, then measurements were performed 15, 30, 45 and 60 minutes after the exposure ended. This test was performed to determine how long it takes for the photocatalytic effect to dissipate.

7.8 X-ray diffraction (XRD)

X-ray diffraction patterns were gathered in order to determine difference in the layer thickness, distance between layers and the number of layers, as a result of thermal reduction and also to determine if the addition of TiO_2 has any effect.

The samples chosen for testing, were GO unreduced and GO reduced at $140°C$, $160°C$, $180°C$ and $220°C$; 2 TiO_2/GO mixtures, one with a high TiO_2 content and one with low (mixture A and C), the TiO_2/GO mixtures were reduced at $140°C$ and $160°C$. Additionally, the commercial TiO_2 powder Kronos and the TiO_2 created using microwaves were sampled to compare them.

For gathering the XRD patterns of the membranes a Philips Panalytical X'Pert X-Ray Diffractometer was used, with a Cobalt source running at $45kV$, $20mA$ and a wavelength of 1,7889700Å.

7.9 Scanning Electron Microscope (SEM)

SEM was used to analyze the surface characteristics of the membranes before and after UV exposure, and evaluate if the UV exposure caused any damage to the surface. EDX (Energy-dispersive X-ray spectroscopy) mapping was used to determine the particle size of TiO_2 clusters and see if there was a difference in TiO_2 surface concentration of mixture A and C (high and low TiO_2 content).

The SEM measurements were performed using a Zeiss 1540xb, for the EDX mapping a Thermo UltraDry attachment was used.

7.10 Water Vapor Transmission

The GO membranes were tested according to a standard test method for water vapor transmission (WVT) of materials, ASTM E96, and compared to two commercial membranes (Alfa Laval NFT50 and NF99HF). The experiments were conducted using water, ethanol and hexane as the permeants. All experiments were carried out in a temperature controlled oil bath set at $35°C$ where each sample was weighed at the start and then at hourly intervals. The permeant solution was poured into test tubes where the membranes were subsequently glued upon using ethyl cyanoacrylate based glue or epoxy glue, see figure 7.9.

Figure 7.9: *Setup for permeation tests with GO membranes and water as permeant.*

Table 7.2: First experiment setup with water as the permeant. The experiment was double determination.

T	T 140	T 160	A 140	A 160	B 140	B 160	C 140	C 160	Open

The first experiment conducted was a duplicate analysis with all GO membranes using water as the permeant, which is the setup seen in figure 7.9. For this experiment, a glue based on ethyl cyanoacrylate was used. Two open samples were also run in order to compare these results to the GO membranes. After this experiment concluded, it was found that there were small variations in the diameter of the test tubes, which explains some of the variations in the results. The diameter was measured to be approximately 1 cm in these test tubes, which is the value used for WVT and permeance calculations. The setup can be seen in table 7.2, where T is unreduced GO.

The second experiment was done using ethanol and hexane and T, T 140, C 140 and an open tube. The third and final experiment was a test of the commercial membranes NF99HF and NFT50, where permeation with water, ethanol and hexane was tested. In the second and third experiment, an epoxy glue was used and the test tubes had a diameter of 1,35 cm which is used for WVT and permeance calculations.

8 Results

In this chapter the results gathered from the characterizations will be presented.

8.1 GO Method

In order to evaluate the best method for producing GO for the laboratory work, 3 methods were tested and compared using XRD and FT-IR.

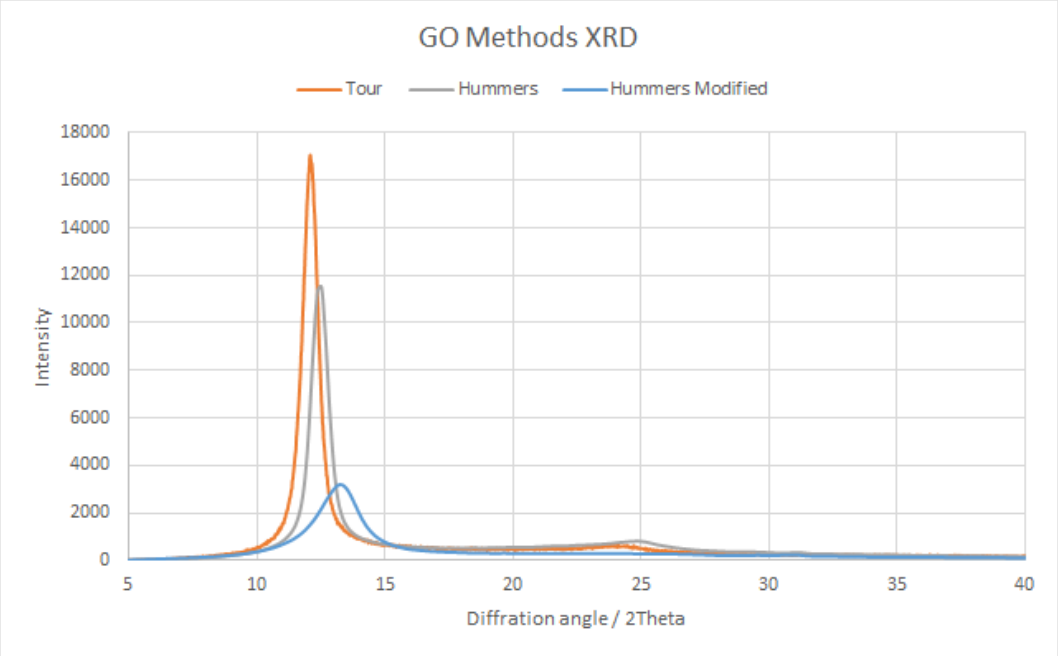

Figure 8.1: *XRD patterns comparing Tour's, Hummer's and Modified Hummer's method for preparing GO.*

The XRD results shows that the peaks for Tours and Hummers method are similar, however modified Hummers has slightly shifted broad peak resulting in a high FWHM value. The methods were expected to be similar, but since only one batch of modified Hummers was made, the difference could be from an error in the synthesis. This difference could be from overheating in the synthesis, where the temperature was heated to $98°C$. If the temperature was too high, the GO solution might have been reduced and result in a slightly shifted peak with a lower count. This tendency is also apparent in the Hummers method,

where the peak is also shifted slightly compared to the the Tour's method, see figure 8.1 and table 8.1

Table 8.1: FWHM, peak, d, D and N values for the 3 GO methods tested.

	FWHM	Peak	d / nm	D / nm	N
Tour	0,7397	12,106	0,848	12,54	14,78
Hummers	0,7289	12,459	0,824	12,73	15,44
Modified Hummers	2,0272	13,258	0,775	4,58	5,91

As seen from figure 8.2, the FT-IR spectras are similar, but there is a difference in the $C-H$ peak at approximately $3000cm^{-2}$. The C-H peak is larger in Hummer's and modified Hummer's method, which indicates a larger amount of hydrophobic carbon material, as is described with figure 2.4. Because the XRD spectra of the Tour's method is similar to that of the Hummer's method, and the FT-IR spectra indicate more leftover hydrophobic carbon material in Hummer's and modified Hummer's, the Tour's method was chosen for further experiments. The Tour's method is also significantly more time efficient than Hummer's and modified Hummer's, both of which require many hours of laboratory work.

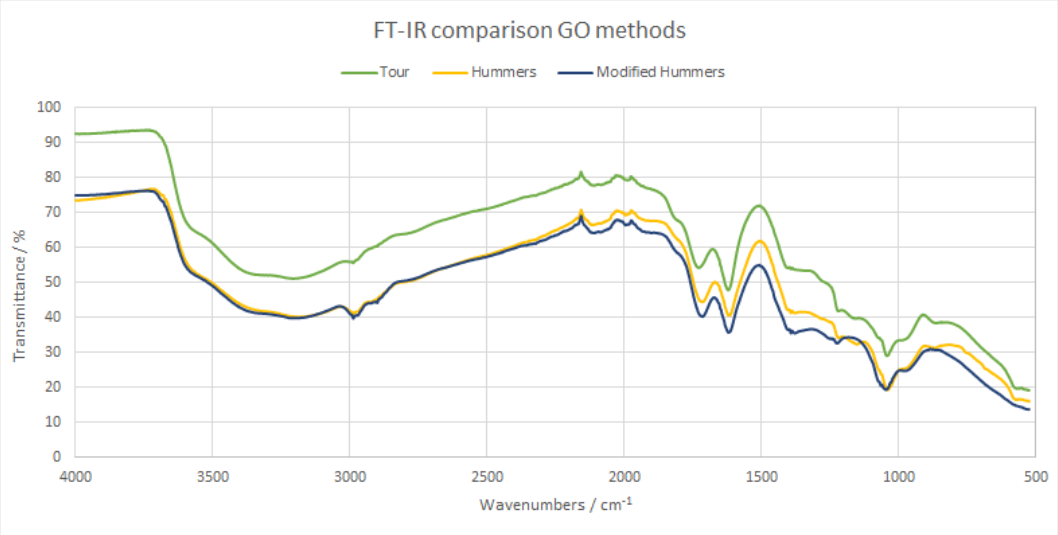

Figure 8.2: *FTIR spectra comparing Tour's, Hummer's and Modified Hummer's method for preparing GO.*

8.2 FT-IR

Several FT-IR spectra was obtained for analyzing the membrane material produced. These FT-IR spectra show the functional groups present in the membrane, as can be seen on figure 8.3, there is the possibility of several different functional groups. The presence of carboxylic groups can be seen from the peak O-H peak at $3400cm^{-2}$, the $C = O$ peak at $1740cm^{-2}$ and the C-O peak at $1230cm^{-2}$. This was also observed during zeta potential measurements, where the starting pH was below 5 in all measurements. This is because the carboxyl group dissociates into H^+ and COO^- and thus providing slightly acidic conditions. The $O - H$ peak at $3400cm^{-2}$ and $C - O$ peak at $1080cm^{-2}$ confirms the presence of alcohol groups. The $C = O$ peak at $1740cm^{-2}$ and $C - O$ at $1080cm^{-2}$ indicates the presence of ester groups in the membranes. There is also the possibility of ketone groups (C=O $1740cm^{-2}$) and ether groups (C-O $1080cm^{-2}$). Overall the GO appears to be highly oxidized and thus hydrophilic.

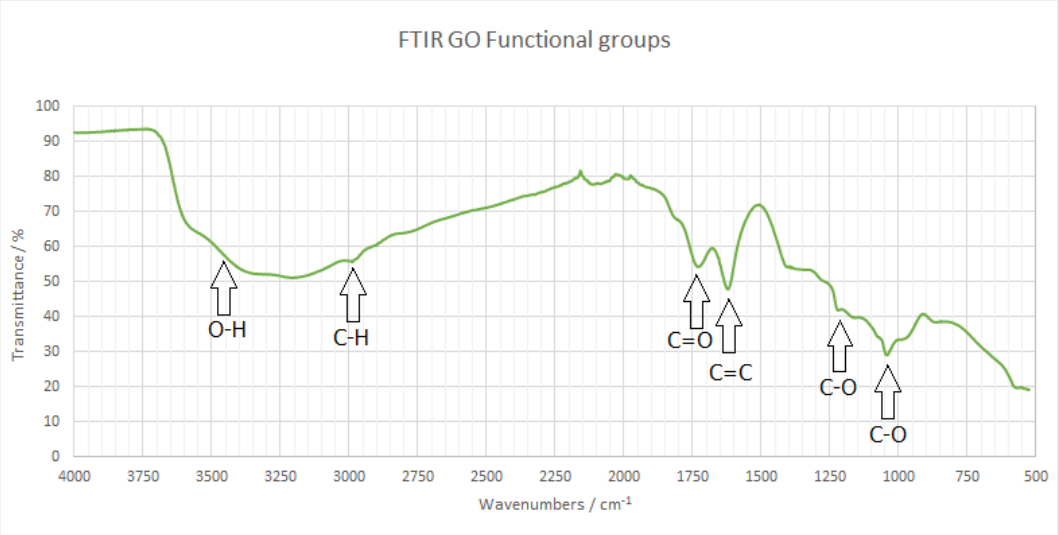

Figure 8.3: *FT-IR spectre of GO showing the functional groups measured.*

Table 8.2: List of bonds and possible functional groups for the FT-IR spectra of GO.

Wavelength	Bond	Functional group
3400	O-H	alcohol, carboxylic acid
2950	C-H	alkan
1740	C=O	ester, ketone, carboxylic acid
1650	C=C	alken
1230	C-O	carboxylic acid
1080	C-O	ester, ether, alcohol

Figure 8.4 shows the difference between reduction at 140 and 160°C and the results are what was expected. The difference in the spectra lies in removal

of more O-H groups ($3400cm^{-2}$) at $160°C$ and a slightly larger $C-H$ peak at 2950. The difference between 140 and $160°C$ therefore seems to be in removal of $-OH$ groups, which are replaced by $C-H$ groups. This is also evident by the larger $C-H$ peak at $160°C$.

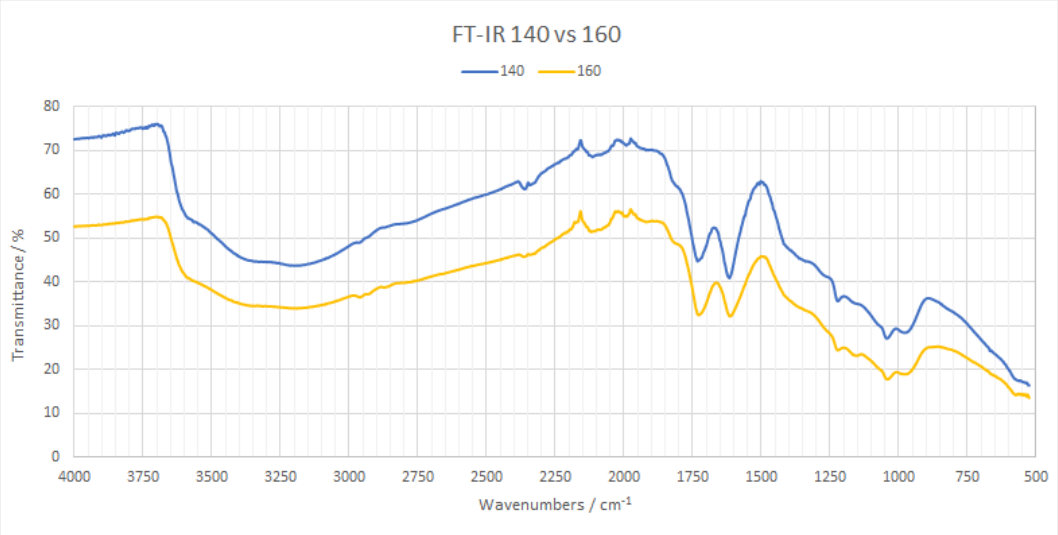

Figure 8.4: *Comparison of FT-IR spectra of GO reduced at* $140°C$ *and* $160°C$.

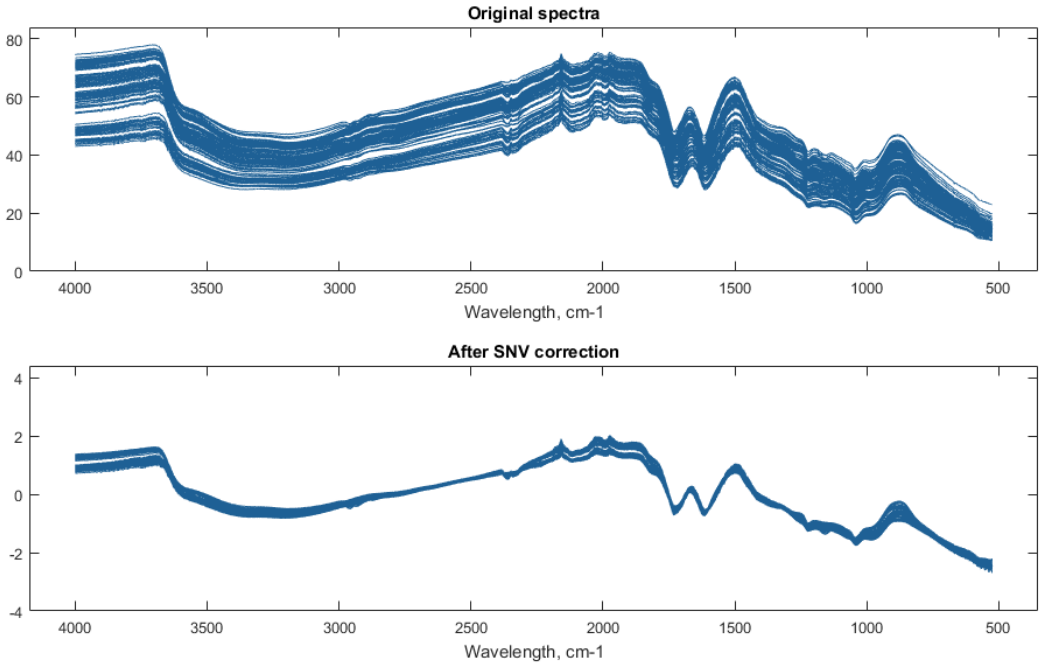

Figure 8.5: *FT-IR spectra of the samples tested (10 spectra from each sample), above is the raw spectras and below is the SNV corrected spectras.*

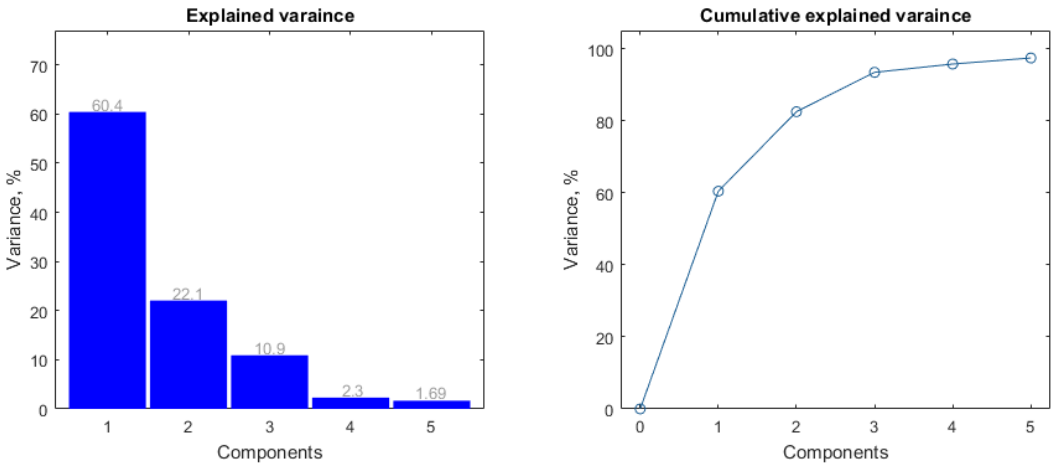

Figure 8.6: *Explaned variance and cumulative explained variance based on amounts of components. 2 components explains 82,5% of the variance in the data*

The results from the UV test, exposing the membranes to UVC light for 30 minutes, can be seen on figure 8.5, where 10 spectra from each sample are combined and SNV corrected. When the results were analyzed using PCA, it revealed that 2 components explained 82,5% of the variance, see figure 8.5

When analyzing the data plotting the results of component 1 variance vs component 2 variance, see score plots on figure 8.7 and loading plots on figure 8.8. In the score plot for mixtures, there is a clear groupings of the samples on the left side, which is the samples unexposed to UVC light, however these samples exposed to UV-C on the right side seems scattered.

The UV score plot shows clear groupings along the y-axis, which is explained the component 1 and component explains the -OH group, this shows a possiblity that the surface has more -OH groups after being irradiated with UV light. This could be evidence that the surface is induced with superhydrofility caused by the TiO_2 when exposed to UV light.
The score plot for temperature seems random, the reason for this is the heavy influence the UV treatment has on the samples, causing the effect of reduction temperature to be of lesser importance.

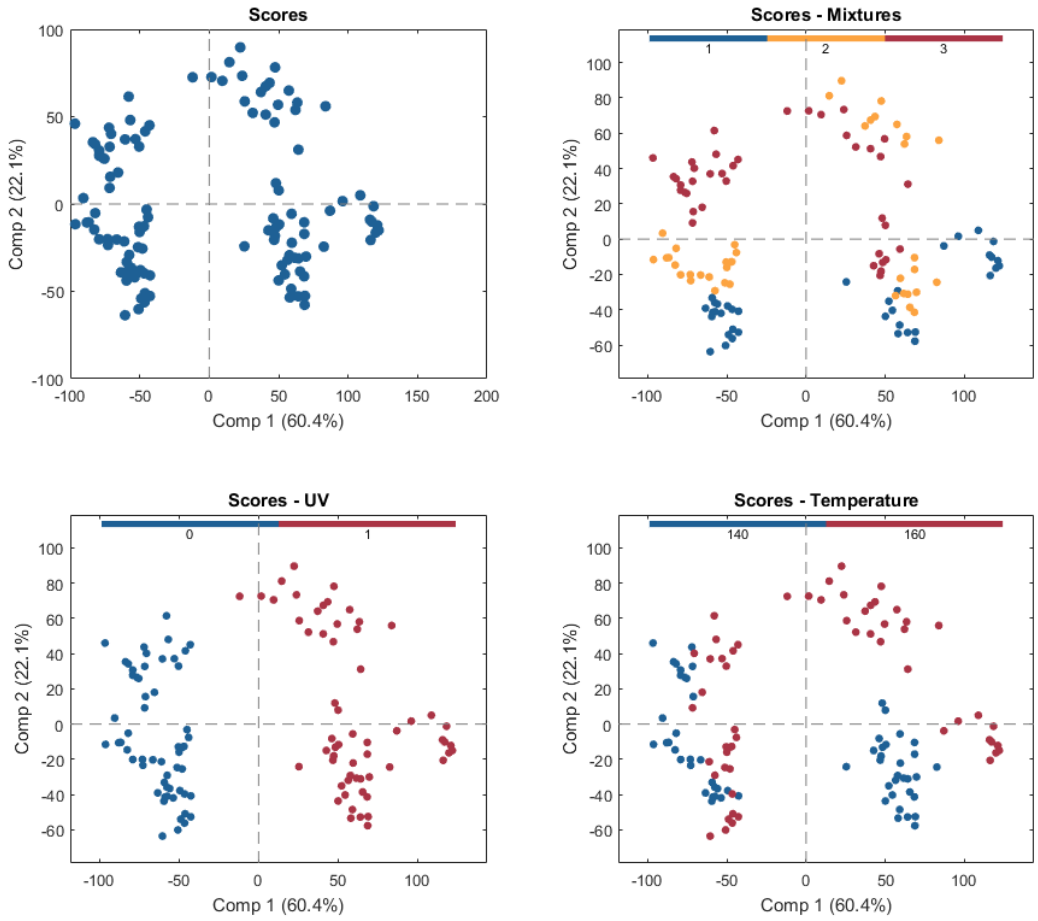

Figure 8.7: *Score plots, top left: same color for everything, top right: colored by mixture (1=A (high TiO_2 content), 2=B (medium TiO_2 content), 3=C (low TiO_2 content)), bottom left: colored by UV treatment (0= no UV, 1= UV), bottom right: colored by reduction temperature.*

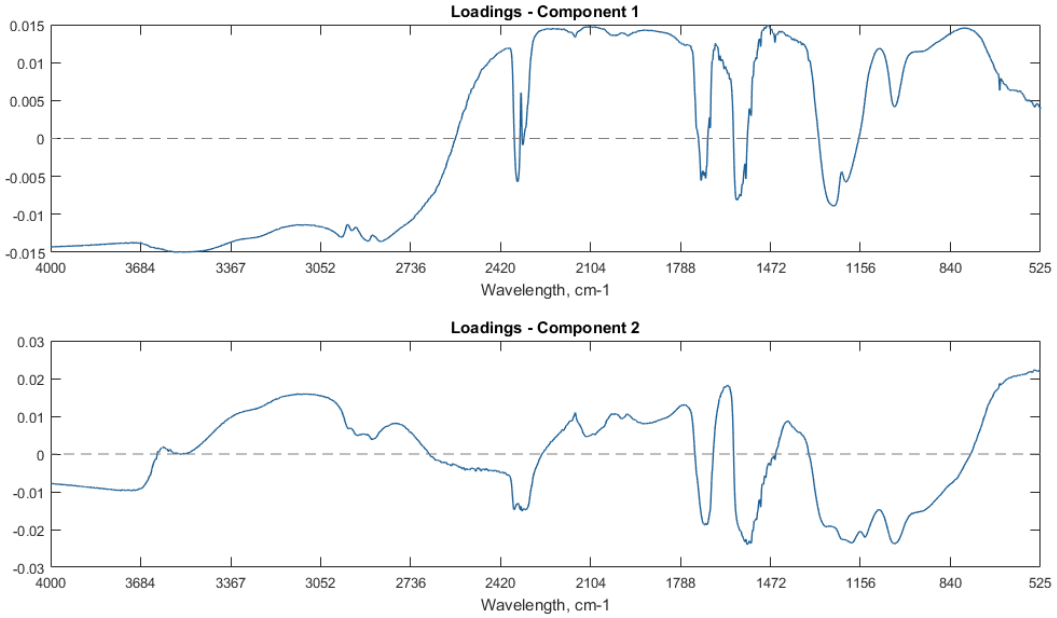

Figure 8.8: *Loading plots for component 1 and 2, showing what wavelengths are explaining the variance in the different components.*

8.3 Drop Shape Analysis

Table 8.3 shows the results gathered from the drop shape analysis of the membranes, and table 8.4 shows the results gathered after exposing the membranes to UV-C light.

Table 8.3: Contact angles for membranes, tested with water and diiodomethane, 5 measurements taken for each to find the average value. Calculated surface energy and surface polarity.

	Water	Diiodomethane	P component / $\frac{mN}{m}$	D component / $\frac{mN}{m}$	Surface Energy / $\frac{mN}{m}$	Surface Polarity / %
Tour 140	53,0	39,7	14,49	39,75	54,24	26,7
A 140	48,1	27,7	14,78	45,15	59,93	24,7
B 140	52,0	31,9	13,43	43,43	56,86	23,6
C 140	65,3	25,6	6,07	45,94	52,01	11,7
Tour 160	88,8	37,2	0,39	40,98	41,37	0,9
A 160	78,9	28,9	1,78	44,68	46,46	3,8
B 160	80,8	29,1	1,35	44,59	45,94	2,9
C 160	86,7	29,1	0,38	44,59	44,97	0,9
NF99HF	19,8	63,7	42,14	26,45	68,59	61,4
NFT50	25,0	60,8	38,30	28,09	66,39	57,7

The contact angle measurements shown in table 8.3 show that there is a big difference between membranes reduced at 140 and 160°C in terms of a hydrophilic surface. The membranes reduced at 140°C have a measured contact angle of around 50° when water is used, apart from mixture C, which has a contact angle of $65,3°$. When reduced at 160°C, the contact angle lies in the range of $80 - 85°$, indicating a large loss of hydrophilic functional groups at the surface. The surface energy of the membranes is also higher at 140°C

than 160°C, and there is a big difference in polar component and thus surface polarity. If the C mixture reduced at 140°C is regarded as a slight outlier, there seems to be a pattern in TiO_2 concentration and the corresponding contact angles for water and diiodomethane. The contact angle for water is lower in membranes with higher TiO_2 concentrations for membranes reduced at 140 and 160°C. While this shows increased hydrophilicity linked to TiO_2 concentrations, the data also clearly shows a change in the contact angle for diiodomethane in membranes without TiO_2 versus membranes with TiO_2. As seen in the table, the membranes with TiO_2 have a significantly lower contact angle with diiodomethane and therefore have a larger dispersive component.

The contact angle measurements of the commercial membranes NF99HF and NFT50 show what was expected; these membranes have been engineered to have a highly hydrophilic surface and thus a low contact angle with water. Meanwhile, the contact angles for diiodomethane were also significantly higher in these membranes compared to GO, resulting in membranes with high surface polarity.

Table 8.4: Contact angles for membranes containing TiO_2 after 30 minutes exposure to UV-C light, tested with diodomethane and water, 5 measurements taken for each to find the average value. Calculated surface energy and surface polarity.

	Water	Diiodomethane	P component / $\frac{mN}{m}$	D component / $\frac{mN}{m}$	Surface energy / $\frac{mN}{m}$	Surface polarity / %
A 140	19,8	27,7	28,13	45,15	73,28	38,4
B 140	22,0	31,9	28,39	43,43	71,82	39,5
C 140	21,8	25,6	26,96	45,94	72,90	37,0
A 160	20,8	28,9	28,05	44,68	72,73	38,6
B 160	36,3	29,1	21,30	44,59	65,89	32,3
C 160	42,5	29,1	18,06	44,59	62,65	28,8

The results from the UV-C irradiated membranes, shows that the contact angle with water is reduced significantly, see table 8.4. The membranes reduced at 140°C attains a contact angle of around $20 - 22°$ with water, where the membranes reduced at 160°C attains contact angles of $20 - 42°$ with water. As the contact angle with water drops, the P component rises increasing the overall surface polarity. The content of TiO_2 doesnt seem to have a great influence on the contact angle of water when reduced at 140°, however it seems to have a big influence in the membranes reduced at 160°C. The contact angles for diiodomethane are uninfluenced by the UV-C treatment.

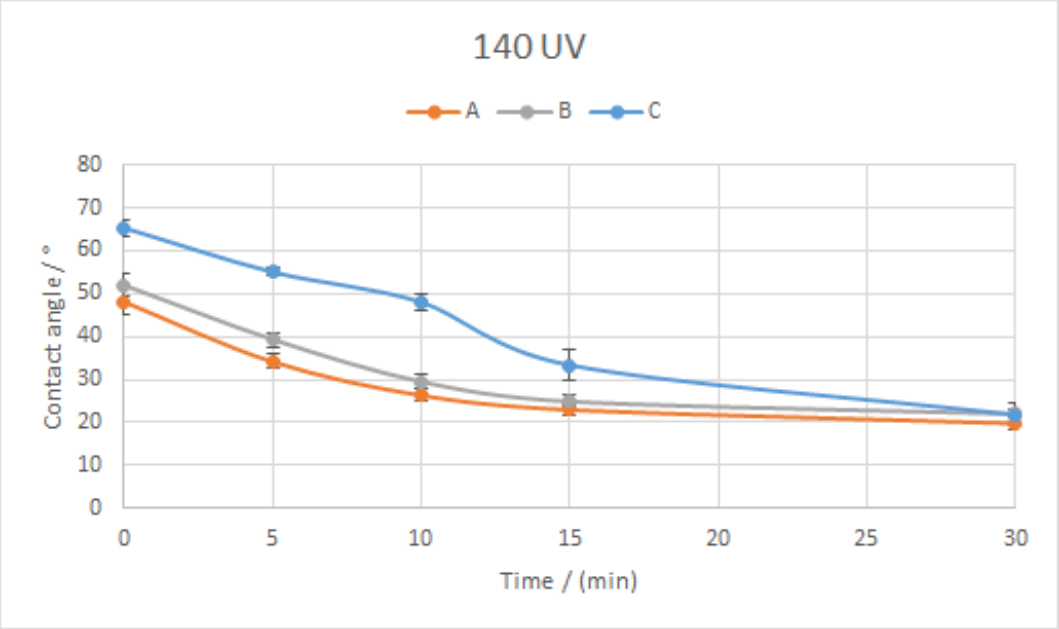

Figure 8.9: *Changes in contact angle for mixture A (high TiO_2 content), B (medium TiO_2 content) and C (low TiO_2 content) when exposed to UV light, measured 5 times, average value plotted with standard deviation.*

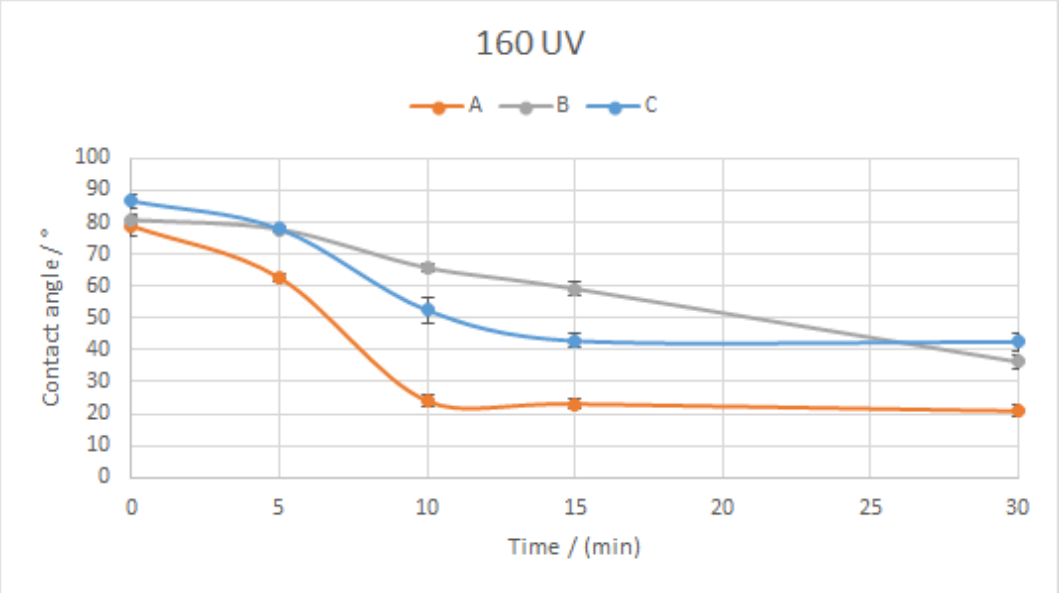

Figure 8.10: *Changes in contact angle for mixture A (high TiO_2 content), B (medium TiO_2 content) and C (low TiO_2 content) reduced at 160°C when exposed to UV light, measured 5 times, average value plotted with standard deviation.*

As seen on figure 8.9, the A, B and C mixtures at 140°C seem to follow an exponentially decreasing function, where the maximum effect is reached around 30 minutes of UV-C irradiation. The time required for maximum effect

also seems to be dependent on TiO_2 concentration; the A and B mixtures are very close to maximum effect at 15 minutes, where the C mixture requires 30 minutes for maximum effect. If UV-C irradiation is used for 30 minutes, from 8.9 it can be seen that the mixtures will all reach the same contact angle, so it may not be necessary to use high amounts of TiO_2.

Figure 8.10 shows the changes in contact angle during UV-C irradiation. The graph is very different from the experiments done with membranes reduced at 140°C; the starting contact angle is significantly higher, and the membranes do not end up with the same contact angle after 30 minutes. The A mixture surprisingly reaches maximum effect after 10 minutes, while the B mixture this time has a linear tendency and might not have reached maximum effect. The C mixture this time reaches maximum effect after 15 minutes, as opposed to the membranes from 140°C, where the membranes needed 30 minutes for maximum effect.

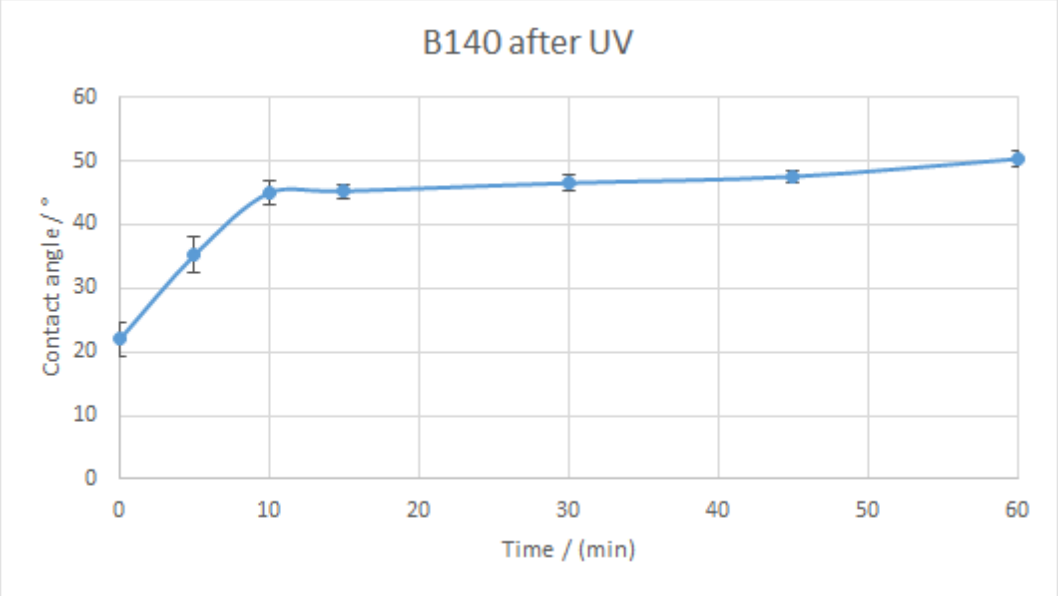

Figure 8.11: *Changes in contact angle for mixture B (medium TiO_2 content) reduced at 140°C after being exposed to UV light for 30 minutes, measured 5 times, average value plotted with standard deviation.*

Figure 8.11 show the change in contact angle after the membrane has been UV-C irradiated for 30 minutes, the contact angle starts at around 22°, and rapidly rising to a contact angle of around 45° after 10 minutes, then it slowly rises to 50° an hour after being irradiated.

8.4 XRD

The thermal reduction of pure GO membranes was examined, see figure 8.12.

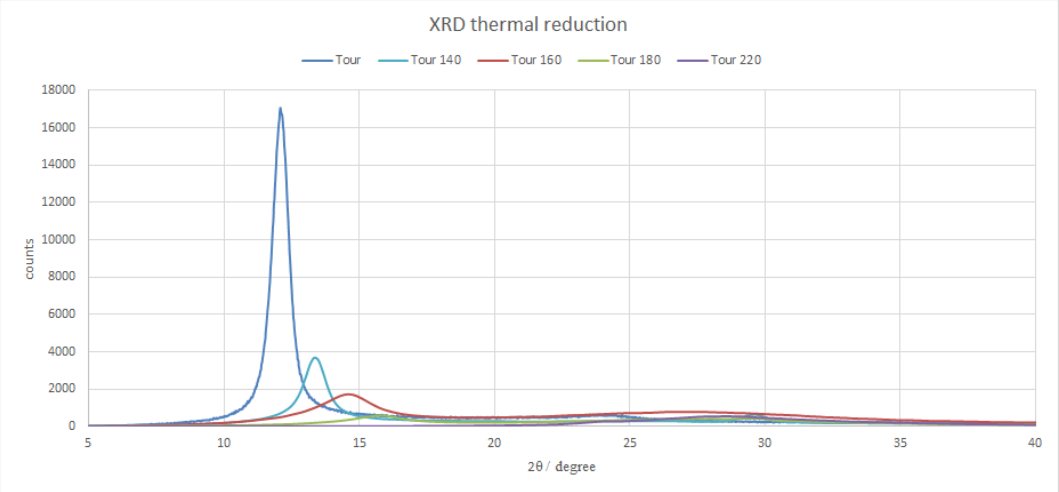

Figure 8.12: *XRD spectre of Tour GO, reduced at different temperatures*

The figure shows the same tendency as found in literature and depicted on figure 2.8. The peak count is significantly higher for an unreduced GO membrane; the peak count declines and the peak shifts according to reduction temperature. The membrane at $140°C$ has a lower count and also a shifted peak, and this tendency is consistent up to $220°C$, indicating changes in the membrane structure.

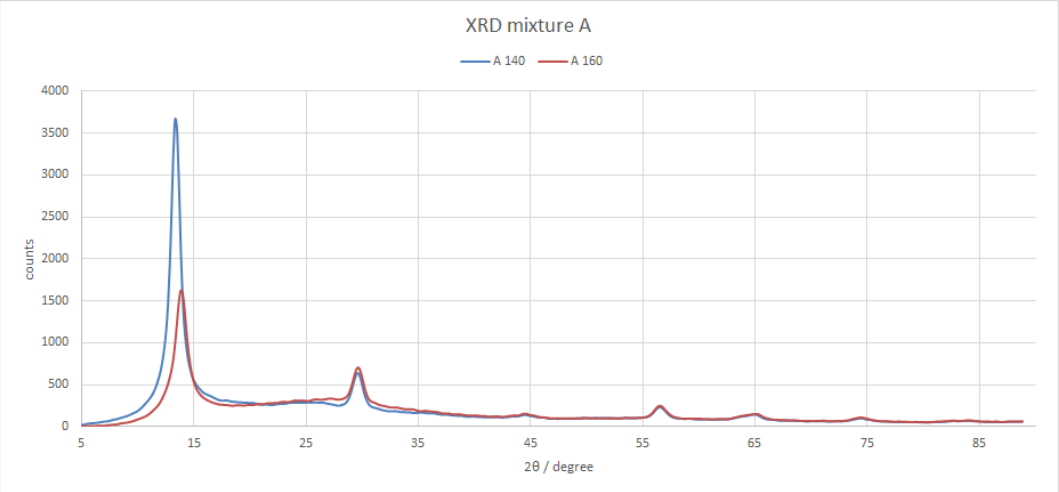

Figure 8.13: *XRD spectre of mixture A (high content of TiO_2*

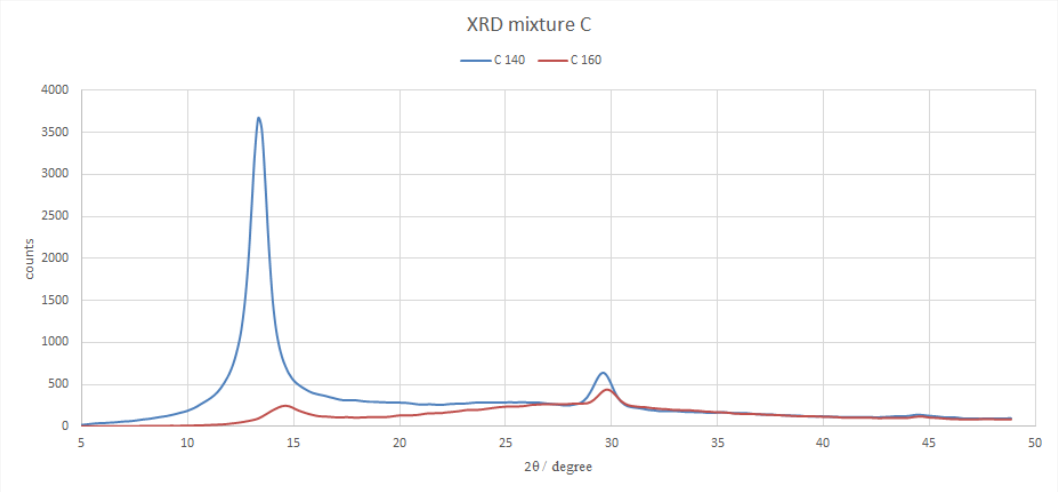

Figure 8.14: *XRD spectre of mixture C (low content of TiO_2*

As expected, there is a slight shift in the peak and the count between A and C membranes reduced at 140 and 160°C. The C membrane reduced at 160°C has a very low peak count in comparison to the A membrane, indicating that the C membrane may have been reduced more. The spectra showing the A membranes is full range in order to see the TiO_2 peaks, but as can be seen from figure 8.13, there is no difference in TiO_2 peaks.

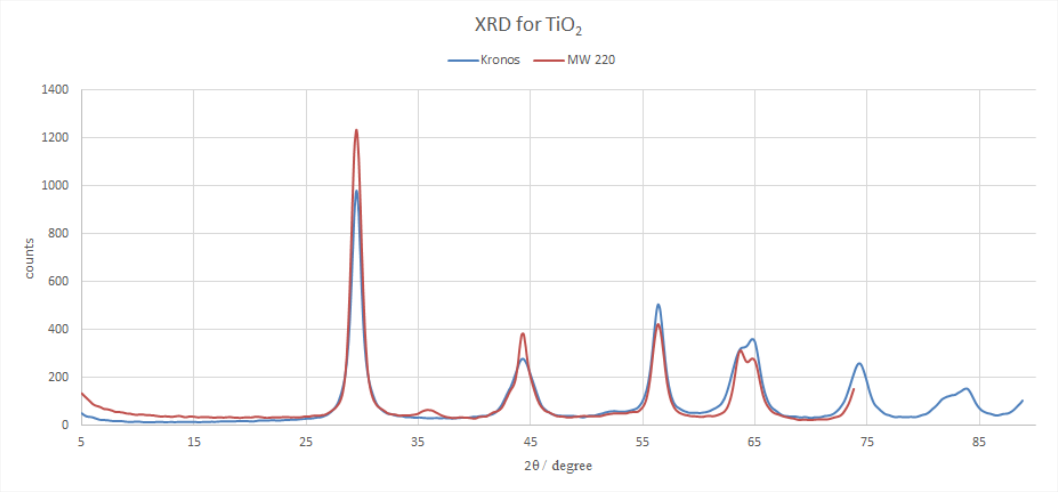

Figure 8.15: *XRD spectre of 2 types of TiO_2, selfmade in microwave (MW220) and a commercial available TiO_2 powder (Kronos)*

Table 8.5 shows the tendency observed in figure 8.12. The distance between layers decreases when the material is reduced, as a result of the loss of water and functional groups. The thickness of the layers and the number of layers also decreases. There does not seem to be a clear difference between membranes with TiO_2 and pure GO membranes in terms of material structure under thermal reduction. While the A and C membranes at 160°C have a thicker layer and a higher number of layers, this tendency is non existent in the membranes reduced at 140°C.

Table 8.5: XRD results, peaks and FWHM values. Calculated values of d and D, and estimated of number of layers N

	FWHM	Peak	d / nm	D / nm	N
GO	0.7397	12.106	0.848	12.54	14-15
GO140	0.9045	13.397	0.767	10.27	13-14
GO160	2.1091	14.590	0.704	4.41	6-7
GO180	2.1545	15.758	0.653	4.32	6-7
GO220	8.3444	28.446	0.364	1.14	3-4
A140	1.0143	13.378	0.768	9.48	12-13
A160	1.4144	13.878	0.741	7.359	9-10
C140	1.1081	13.071	0.786	8.38	10-11
C160	1.5173	14.561	0.706	6.129	8-9
Kronos	0.9509	29.501	0.351	10.03	28-29
MW7 220	1.0166	29.471	0.352	9.383	26-27

Two different TiO_2 powders were also tested in order to compare our own synthesized TiO_2 versus a commercial TiO_2 powder Kronos. There is not a significant difference between the two, despite Kronos having a slightly larger particle size and a higher number of layers.

8.5 Water Vapor Transmission

3 different permeance tests were performed, the first one was done with only Tour membranes with water using glue based on ethyl cyanoacrylate to seal the cylinders, the results can be seen in table 8.6 and on figure 8.16.

Table 8.6: Average WVT and Permeance results from the test with water through the membranes see figure 8.16

	WVT / $\frac{g}{s \times m^2}$	Permeance / $\frac{g}{m^2 \times s \times kPa}$
T	$2,11 \times 10^{-2}$	$5,77 \times 10^{-3}$
T 140	$2,08 \times 10^{-2}$	$5,68 \times 10^{-3}$
T 160	$2,23 \times 10^{-2}$	$6,09 \times 10^{-3}$
A 140	$2,22 \times 10^{-2}$	$6,07 \times 10^{-3}$
A 160	$2,40 \times 10^{-2}$	$6,55 \times 10^{-3}$
B 140	$2,50 \times 10^{-2}$	$6,84 \times 10^{-3}$
B 160	$2,28 \times 10^{-2}$	$6,22 \times 10^{-3}$
C 140	$2,26 \times 10^{-2}$	$6,17 \times 10^{-3}$
C 160	$2,83 \times 10^{-2}$	$7,72 \times 10^{-3}$
Open	2.56×10^{-2}	

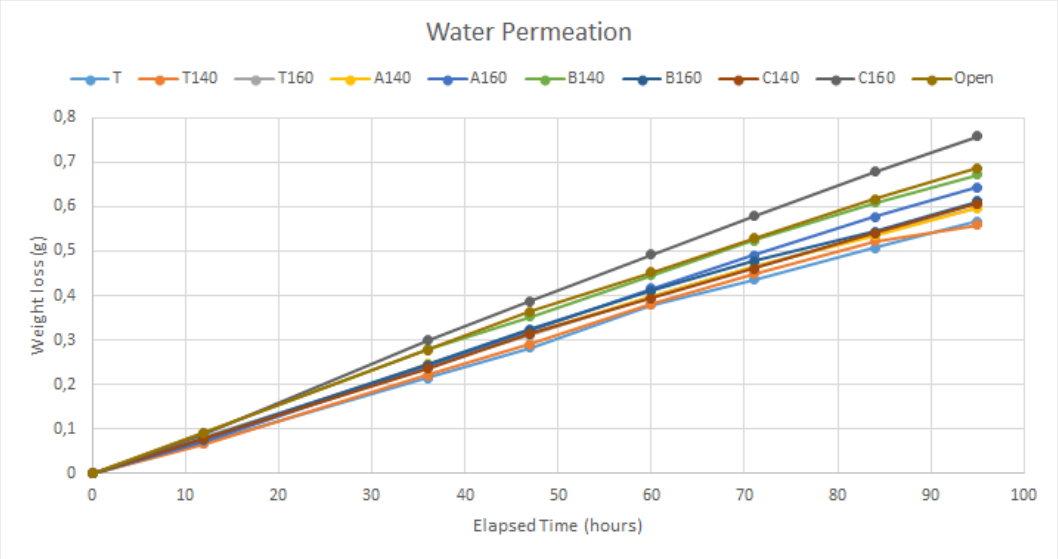

Figure 8.16: *Weightloss of water through membranes*

The results from the water permeance test shows that water is unimpeded through the membranes.

The second permeance test was done with ethanol and hexane, this time using an epoxy based glue. The results with ethanol can be seen in table 8.7 and on figure 8.17. The results show that the membranes slows the permeance through the membranes compared to the open cylinder. This was as expected as ethanol is somewhat polar in nature.

Table 8.7: WVT and permeance for Tour membranes using ethanol

	WVT / $\frac{g}{s \times m^2}$	Permeance / $\frac{g}{m^2 \times s \times kPa}$
C140	$2,70 \times 10^{-2}$	$3,03 \times 10^{-3}$
Tour140	$2,38 \times 10^{-2}$	$2,68 \times 10^{-3}$
Tour	$2,04 \times 10^{-2}$	$2,30 \times 10^{-3}$
Open 1	$6,49 \times 10^{-2}$	

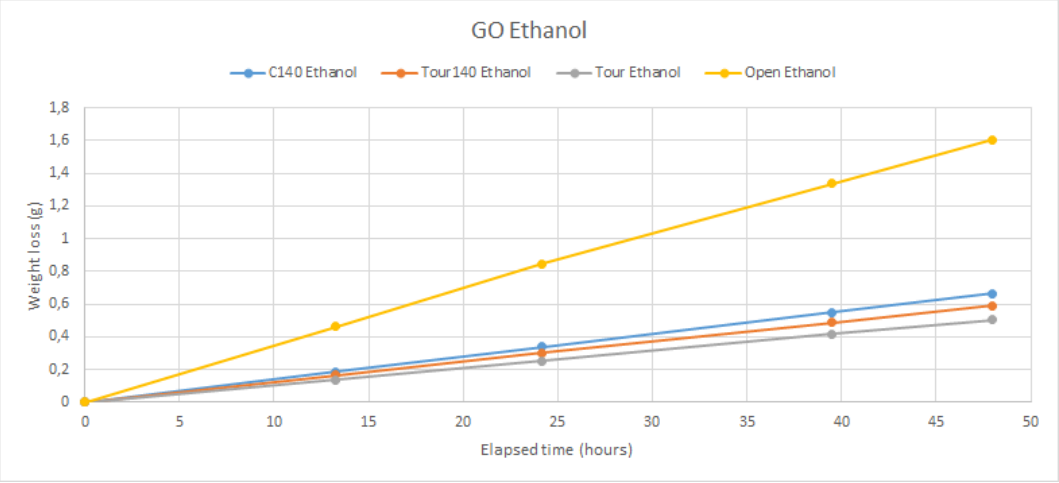

Figure 8.17: *Weightloss of ethanol through membranes*

The results with hexane can be seen in table 8.8 and on figure 8.18, the results show that the membranes almost completely blocks the permeation of hexane when compared to the open cylinder.

Table 8.8: WVT and permeance for Tour membranes using hexane

	WVT / $\frac{g}{s \times m^2}$	Permeance / $\frac{g}{m^2 \times s \times kPa}$
C140	$1,72 \times 10^{-2}$	$8,65 \times 10^{-4}$
Tour140	$1,42 \times 10^{-3}$	$7,15 \times 10^{-5}$
Tour	$1,96 \times 10^{-2}$	$9,88 \times 10^{-4}$
Open 1	$1,77 \times 10^{-1}$	

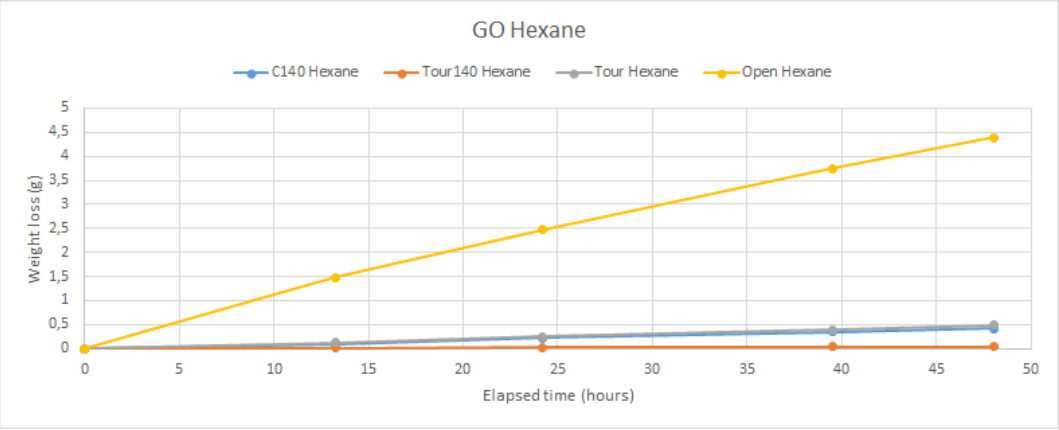

Figure 8.18: *Weightloss of hexane through membranes*

The third and last permeance test was performed with water, ethanol and hexane to test the commercial membranes from Alfa Laval against one of the GO membranes produced, this test used an epoxy based glue.

The results with water can be seen in table 8.9 and on figure 8.19, the results for the GO membrane differs a bit from the previous permeance test, this is possible due to the use of a different glue. The water transport through the GO membrane is higher than the water transport through the membranes produced by Alfa Laval.

Table 8.9: WVT and permeance of membranes with water.

	WVT / $\frac{g}{s \times m^2}$	Permeance / $\frac{g}{m^2 \times s \times kPa}$
NF99HF	$1,04 \times 10^{-2}$	$2,85 \times 10^{-3}$
NFT50	$1,04 \times 10^{-2}$	$2,84 \times 10^{-3}$
A140	$1,62 \times 10^{-2}$	$4,43 \times 10^{-3}$
Open	$2,15 \times 10^{-2}$	

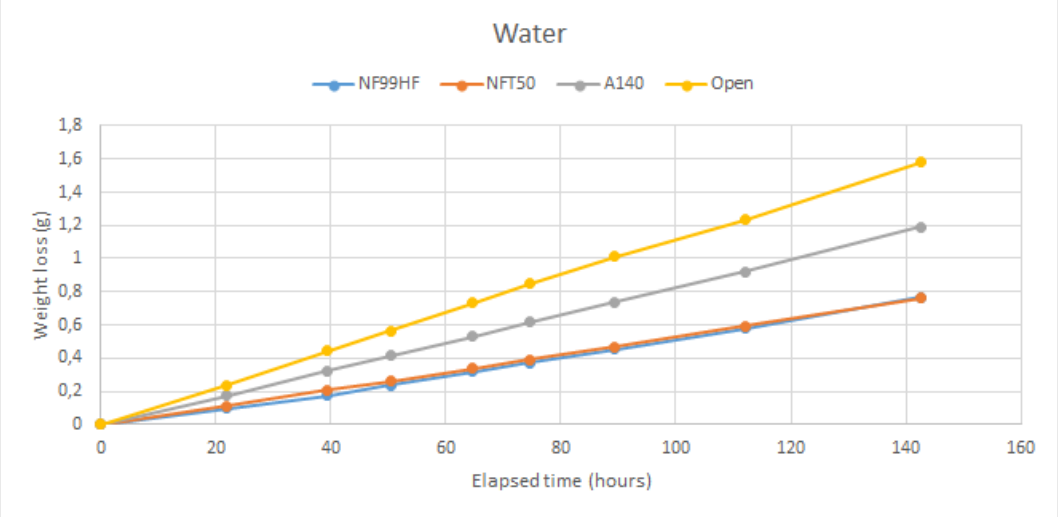

Figure 8.19: *Weightloss of water through membranes*

The results with ethanol can be seen in table 8.10 and on figure 8.20, the results show that the GO membrane holds more ethanol back compared to the 2 Alfa Laval membranes

Table 8.10: WVT and permeance of membranes with ethanol.

	WVT / $\frac{g}{s \times m^2}$	Permeance / $\frac{g}{m^2 \times s \times kPa}$
NF99HF	$3,88 \times 10^{-2}$	$4,36 \times 10^{-3}$
NFT50	$3,04 \times 10^{-2}$	$3,42 \times 10^{-3}$
A140	$1,55 \times 10^{-2}$	$1,75 \times 10^{-3}$
Open	$7,02 \times 10^{-2}$	

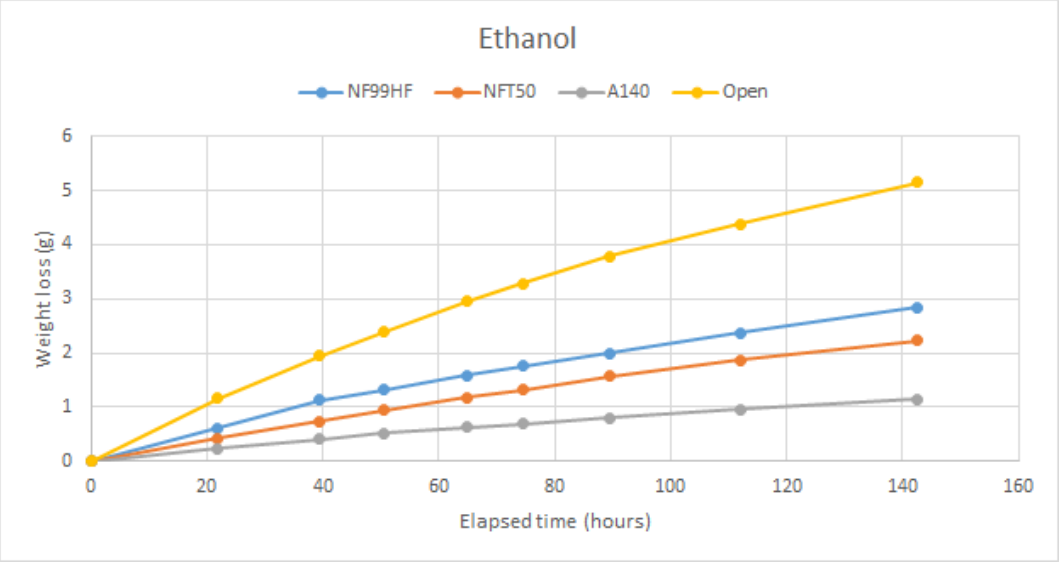

Figure 8.20: *Weightloss of ethanol through membranes*

The results with hexane can be seen in table 8.11 and on figure 8.21. The results show that one of the Alfa Laval membranes lets through more hexane, but the second Alfa Laval membrane blocks the passage of hexane a little better than the GO membrane.

Table 8.11: WVT and permeance of membranes with hexane.

	WVT / $\frac{g}{s \times m^2}$	Permeance / $\frac{g}{m^2 \times s \times kPa}$
NF99HF	$6,33 \times 10^{-2}$	$3,19 \times 10^{-3}$
NFT50	$1,26 \times 10^{-2}$	$6,33 \times 10^{-4}$
A140	$1,69 \times 10^{-2}$	$8,53 \times 10^{-4}$
Open	$2,11 \times 10^{-1}$	

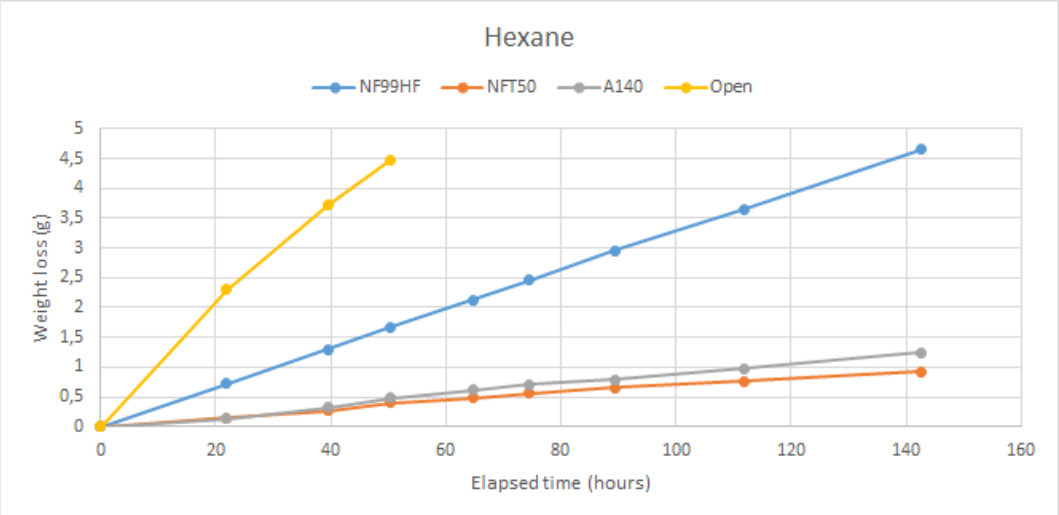

Figure 8.21: *Weightloss of hexane through membranes*

8.6 Zeta potential

The results from the zeta potential measurement performed on the produced GO membranes, with varying TiO_2 content reduced at 140 and 160°C can be seen on figure 8.22, the starting pH of the electrolyte solution was around 7. The carboxylic groups mentioned in the FT-IR results caused the pH to drop down to less than pH 5 before starting the measurements, $NaOH$ was used as titrant to increase the pH levels. All the membranes exhibits a stable negative zeta potential from pH 4-9.

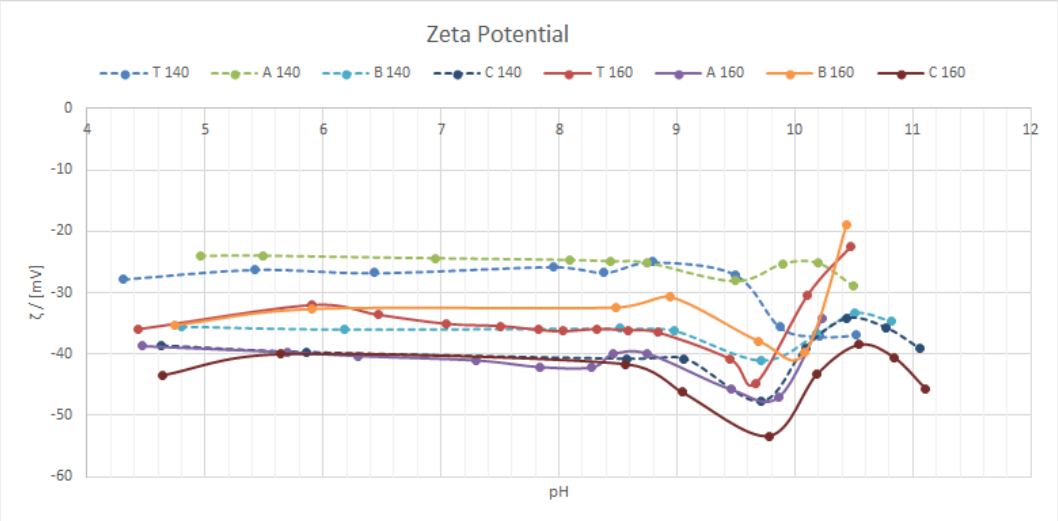

Figure 8.22: *Zeta potential of T (Tour), A (high TiO_2 content), B (medium TiO_2 content) and C (low TiO_2 content) reduced at* 140°C *and* 160°C

The results from irradiating the A membranes (high TiO_2 content) with UV-C light for 30 minutes can be seen on figure 8.23. The results show that the membranes irradiated with UV-C has a more negative zeta potential, the cause can be attributed to an increase in $-OH$ groups, also mentioned in the FT-IR results.

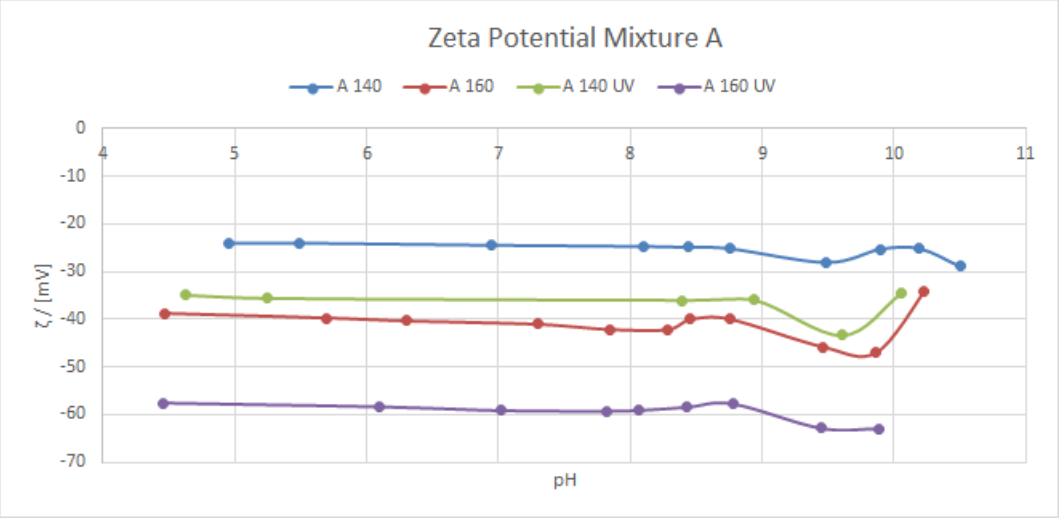

Figure 8.23: *Zeta potential of mixture A membranes (high TiO_2 content), with and without UV irradiation.*

The results from irradiating the B membranes (medium TiO_2 content) with UV-C light for 30 minutes can be seen on figure 8.24. The results show that the irradiated membranes also has a more negative zeta potential.

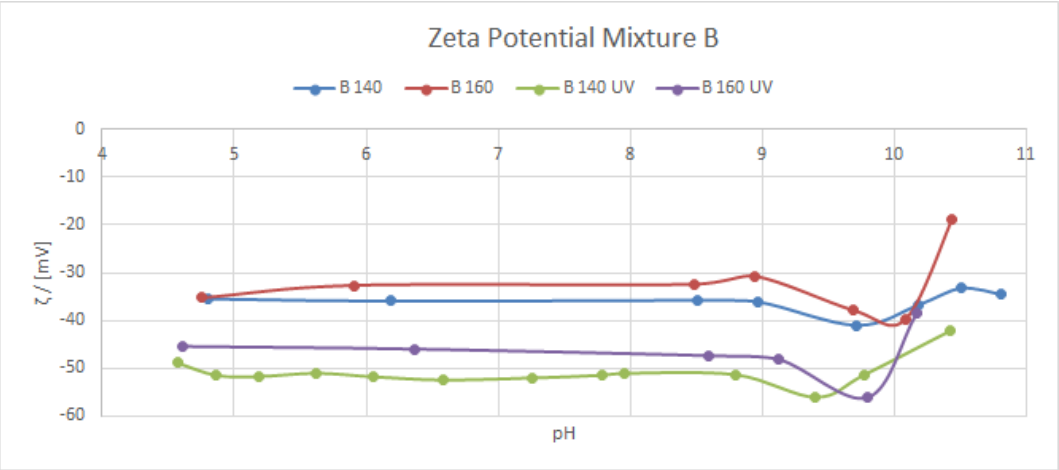

Figure 8.24: *Zeta potential of mixture B membranes (medium TiO_2 content), with and without UV irradiation.*

The results from irradiating the C membranes (low TiO_2 content) with UV-C light for 30 minutes can be seen on figure 8.25. The results show that the irradiated membranes also has a slightly more negative zeta potential.

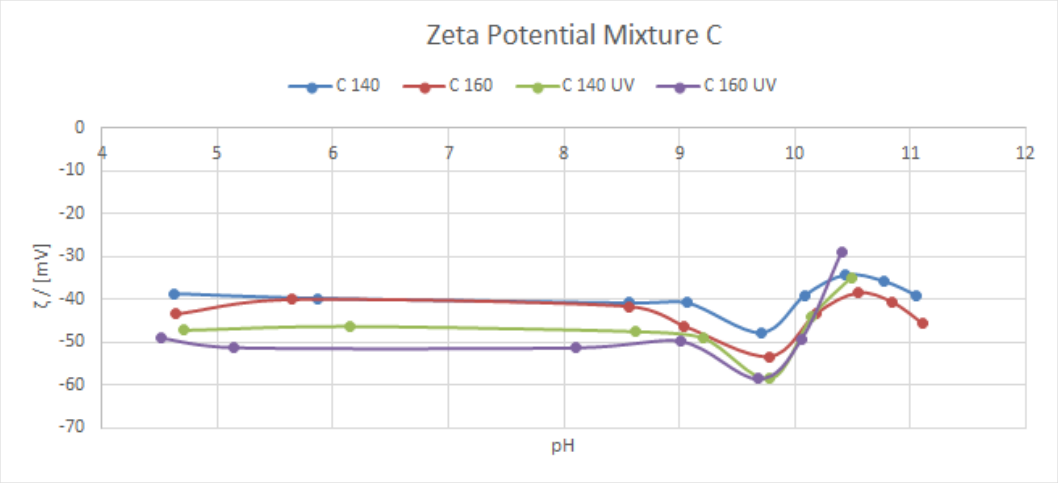

Figure 8.25: *Zeta potential of mixture C membranes (low TiO_2 content), with and without UV irradiation.*

From the zeta potential results observed from the A (high TiO_2 content), B (medium TiO_2 content) and C (low TiO_2 content) membranes with and without UV-C irradiation, its becomes evident that the membranes with a higher TiO_2 content treated with UV-C yields the highest increase in zeta potential.

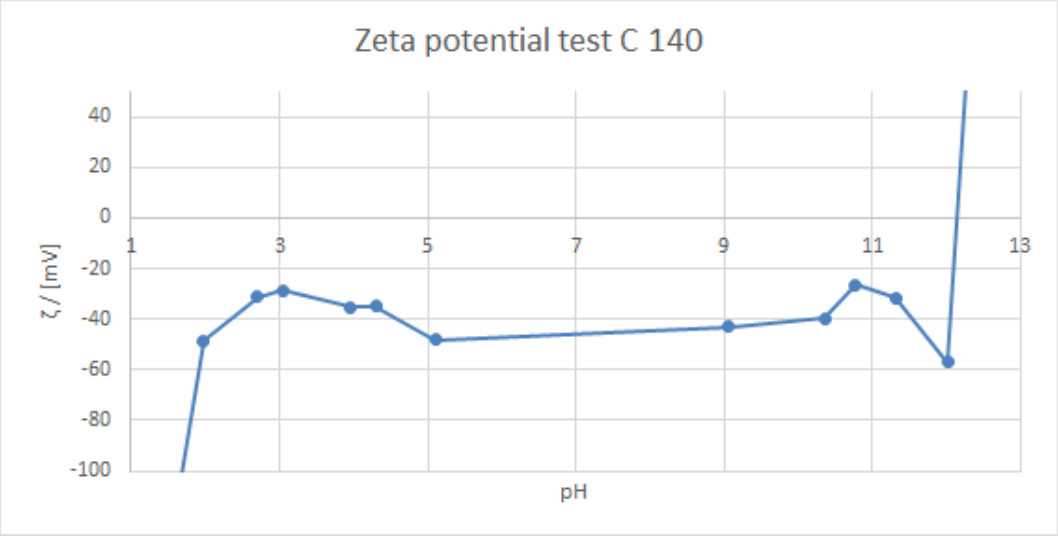

Figure 8.26: *Full pH range zeta potential of mixture C (low TiO_2 content) reduced at* 140°C

The result from the test to see how the membrane performed at extreme pH values can be seen on figure 8.26, the membrane was stable from pH 4-10, the measurements at high and low pH yielded a very high positive and high negative zeta potential, as the measurement wasnt calibrated for these extreme pH values, they arent too reliable.

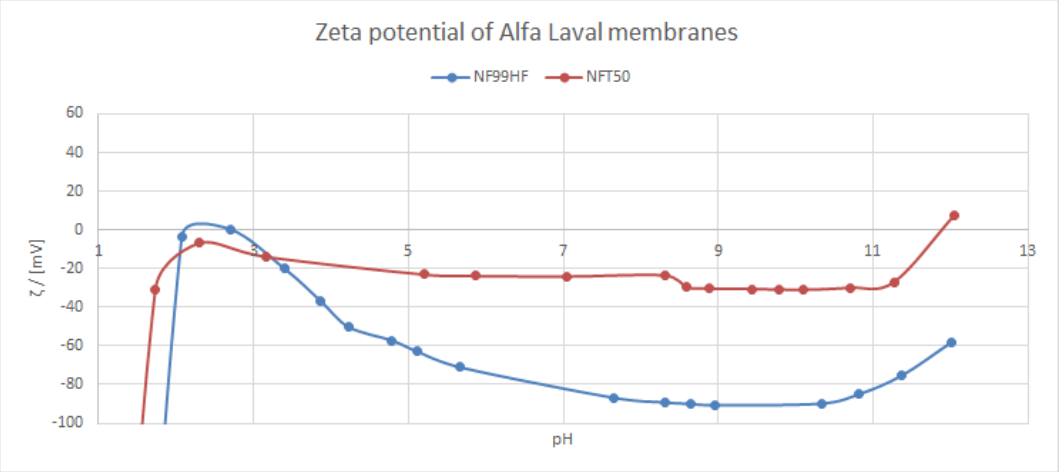

Figure 8.27: *Zeta potential of 2 commercially available membranes produced by Alfa Laval.*

To evaluate the GO membranes, the results from the zeta potentiale of the 2 Alfa Laval membranes can be seen on figure 8.27, the membranes both had a negative zeta potential from pH 4-10, one of them had a significant lower zeta potential, but both are comparable to the produced GO membranes.

8.7 DSC + TGA

During the initial testing periods the thermal reduction was a problem because of explosions when the reduction temperature exceeded $150°C$. This phenomena was investigated in the theory section and it was decided to also investigate it via DSC, see figure 8.28

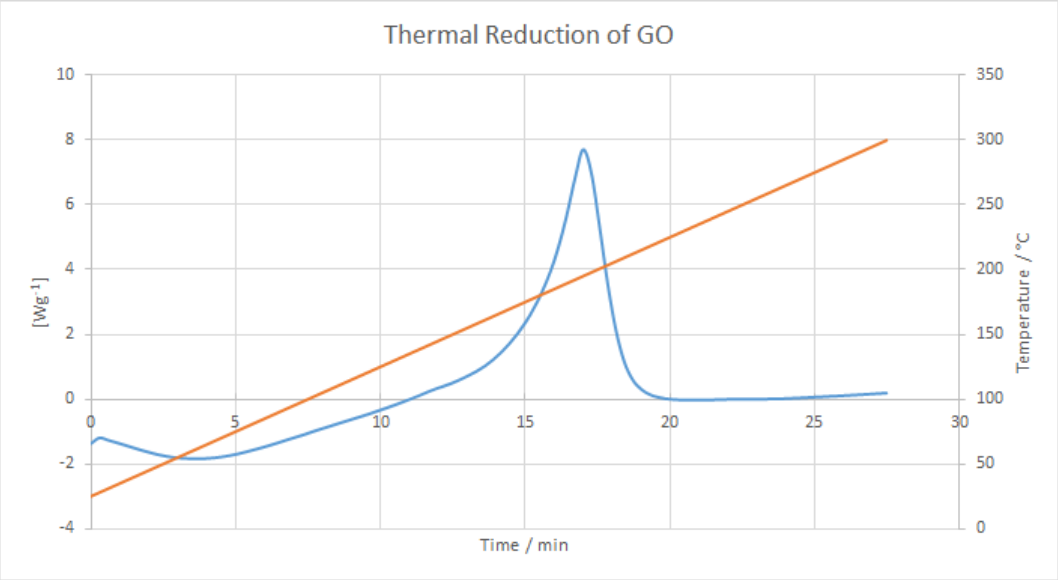

Figure 8.28: *DSC curve showing the evaporation of water and the exothermic reduction reaction, the curve is smooth indicating no explosion, also shows the temperature ramp with the heating rate* $10\frac{°C}{min}$

Figure 8.28 clearly shows the exothermic reaction with a peak ranging between 135 and $220°C$. It seems that the exothermic reaction starts around $135°C$, peaks at $195°C$ and stops around $220°C$. This explains the problems when reducing at $160-180°C$ and above, where it was necessary to slow down the heating rate to avoid explosions.

The weight loss during reduction was also investigated using TGA, see figure 8.29

As seen on figure 8.29, the weight loss during reduction is rapid around $180-200°C$. This corresponds to the results in figure 8.28; the exothermic reaction is caused by rapid weight loss attributed to the loss of functional groups, believed to be mainly hydroxyl groups.

The reduction programs used for reducing the membranes at 140 and $160°C$ were also tested with TGA in order to compare weight loss, see figure 8.30.

Figure 8.30 shows a significant difference in weight loss between the reduction programs for 140 and $160°C$, which was also expected based on the XRD and DSA results. The weight loss for the GO reduced at $140°C$ was 34,15%, while the weight loss for $160°C$ was 47,1%. Furthermore, the results show the weight slowly but steadily declining at $140°C$, confirming the removal of hydroxyl groups at this reduction temperature.

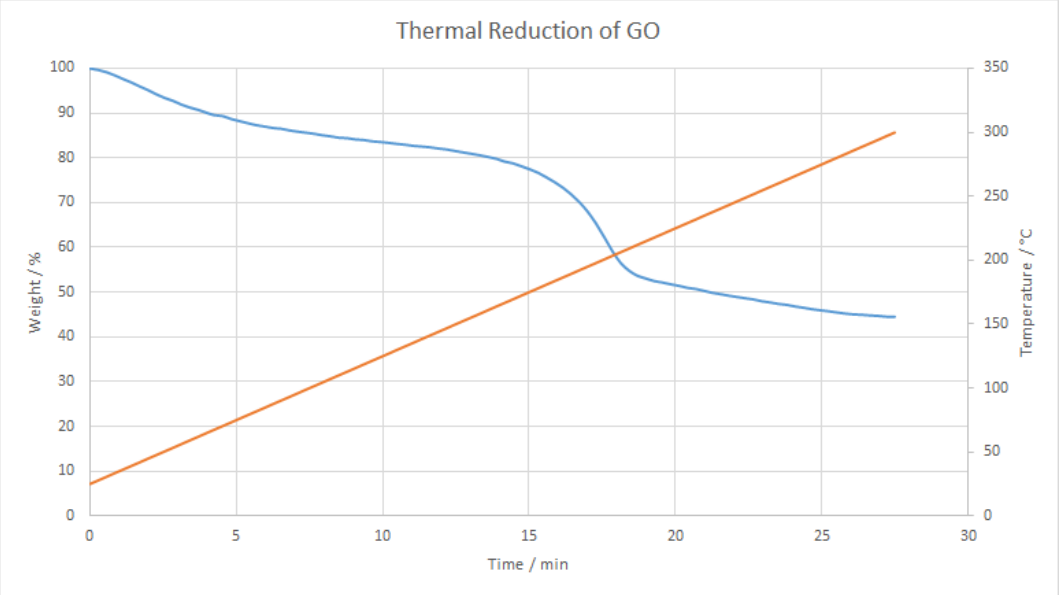

Figure 8.29: *TGA curve showing the weightloss of the sample when thermally reduced and the temperature ramp, the heating was* $10\frac{^{\circ}C}{min}$

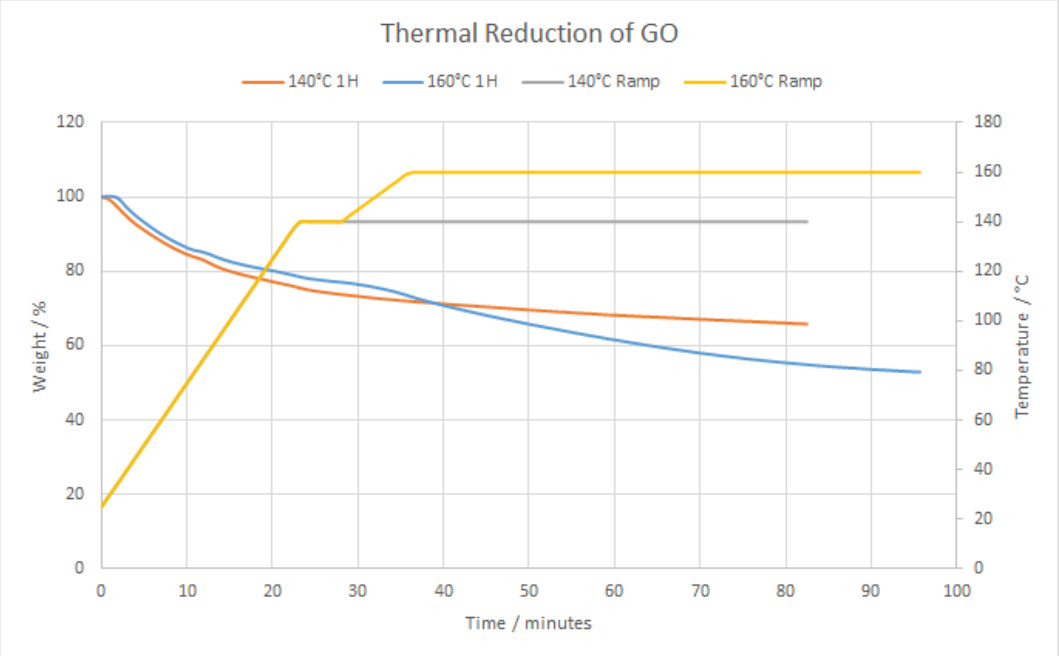

Figure 8.30: *TGA curves showing the weightloss difference of the thermal reduction profiles used for reducing the membranes and the temperature ramps. The heating rate for reducing at* $140^{\circ}C$ *was* $5\frac{^{\circ}C}{min}$ *till* $140^{\circ}C$ *and held there for 1 hour. The heating rate for reducing at* $160^{\circ}C$ *was* $5\frac{^{\circ}C}{min}$ *till* 140°*, held there for 5 min, then heating to* 160° *with a rate of* $2,5\frac{^{\circ}C}{min}$ *untill* $160^{\circ}C$ *was reached, then the temperature was held for 1 hour.*

8.8 SEM

The first results presented will be images obtained from SEM. Pure GO membranes reduced at 140 and 160°C will be compared to see potential structure differences. The A membranes are then compared before and after UV-C irradiation in order to see if the treatment damaged the membrane structure. Lastly, the A membranes will be compared to the C membranes, showing the difference in TiO_2 content at the surface. The following pages will contain SEM images.

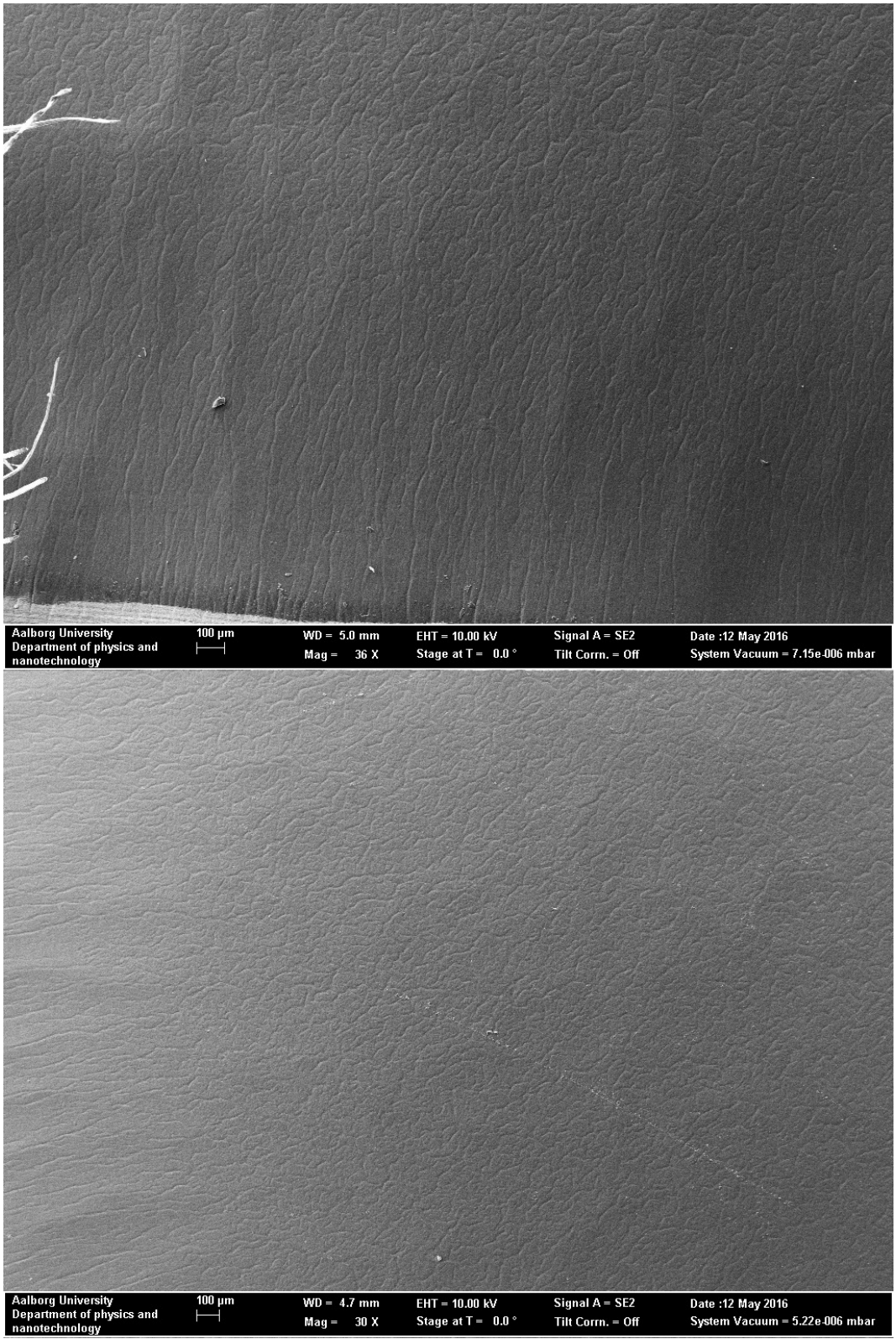

Figure 8.31: *GO membranes, top image is reduced at* $140°C$*, bottom image is reduced at* $160°$.

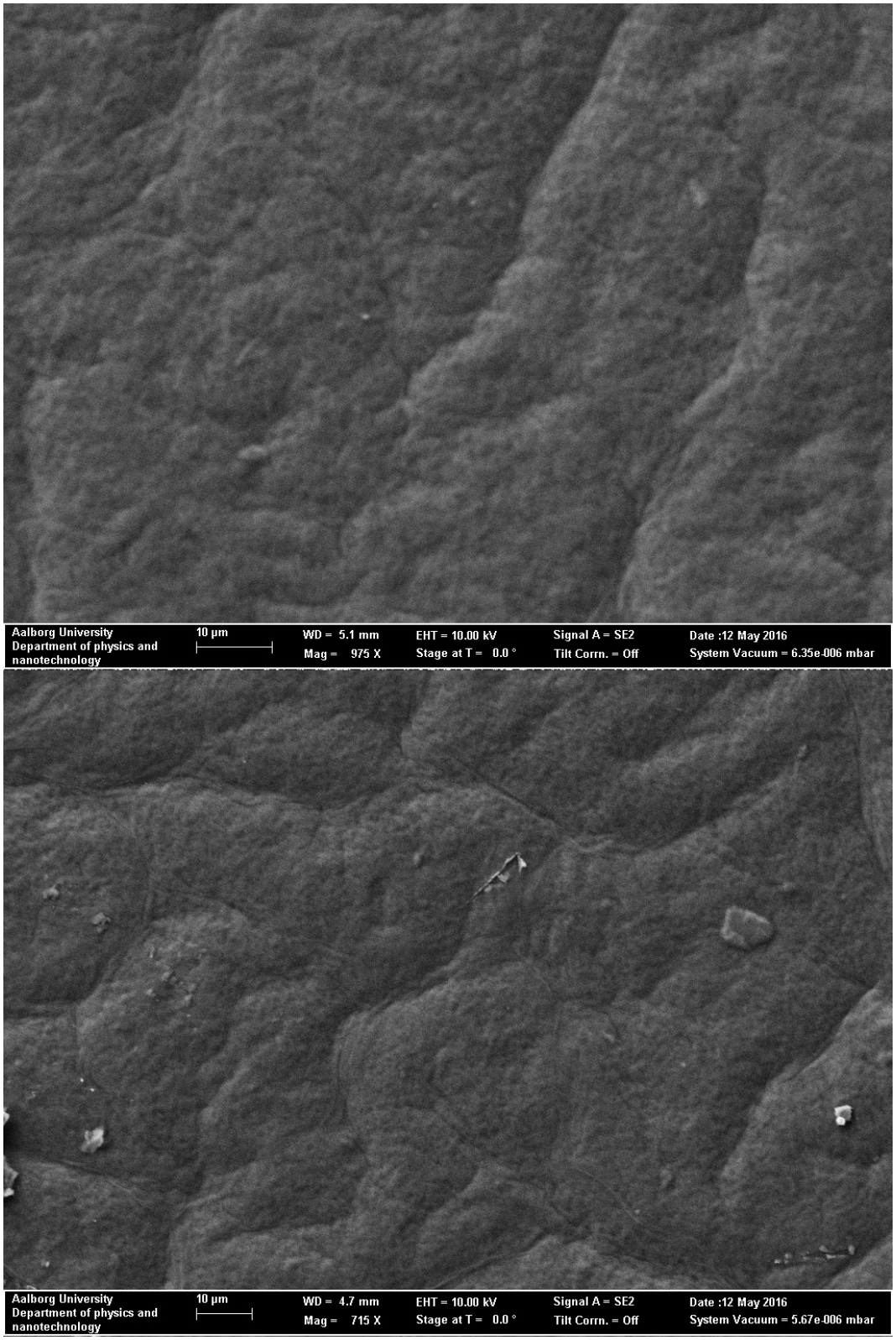

Figure 8.32: *Close up of GO membranes, top image is reduced at* $140°C$*, bottom image is reduced at* $160°$.

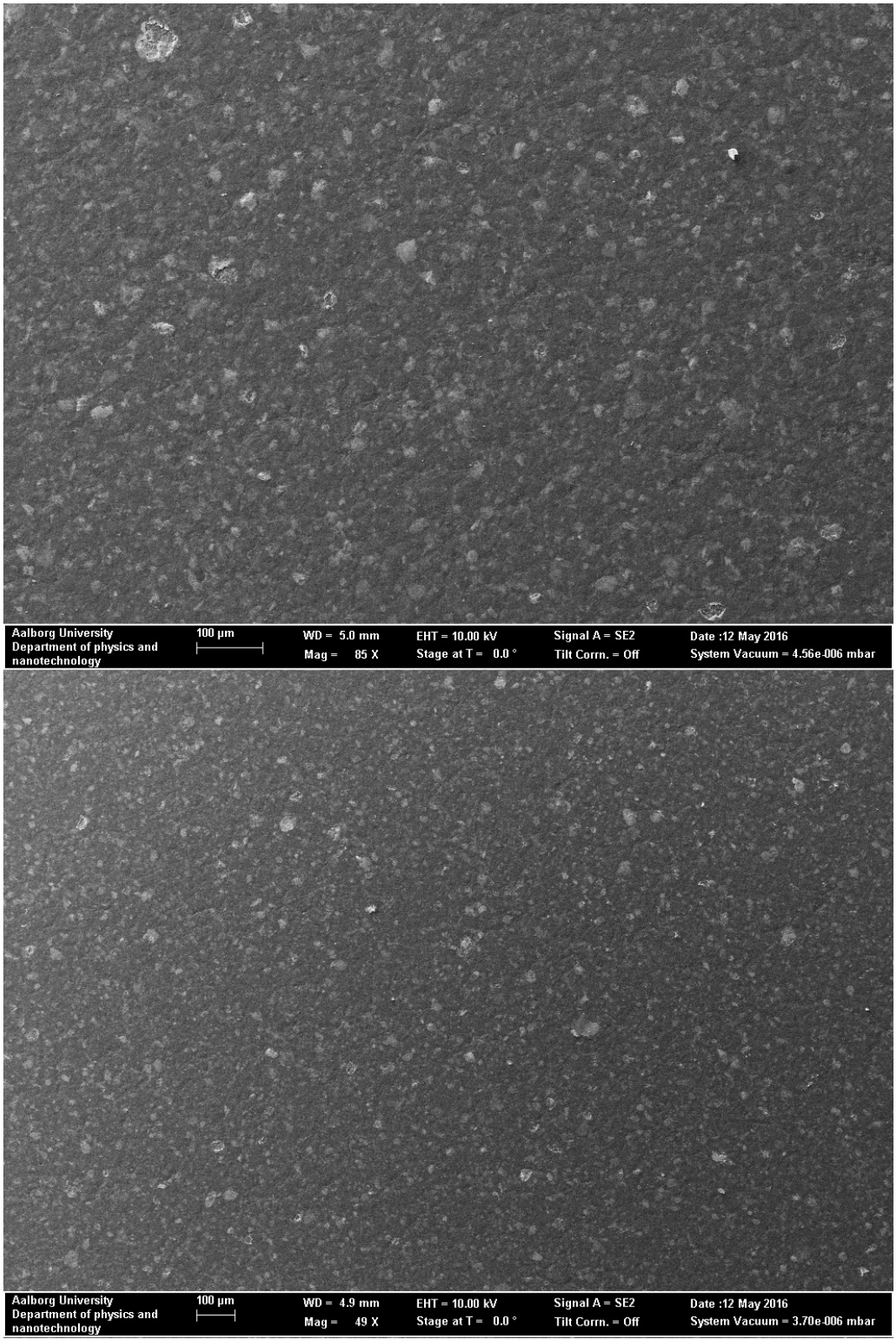

Figure 8.33: *Membrane A (high TiO_2 content) reduced at $140°C$, top image is without UV-C irradiation, bottom image is with 5 hours of UV-C irradiation.*

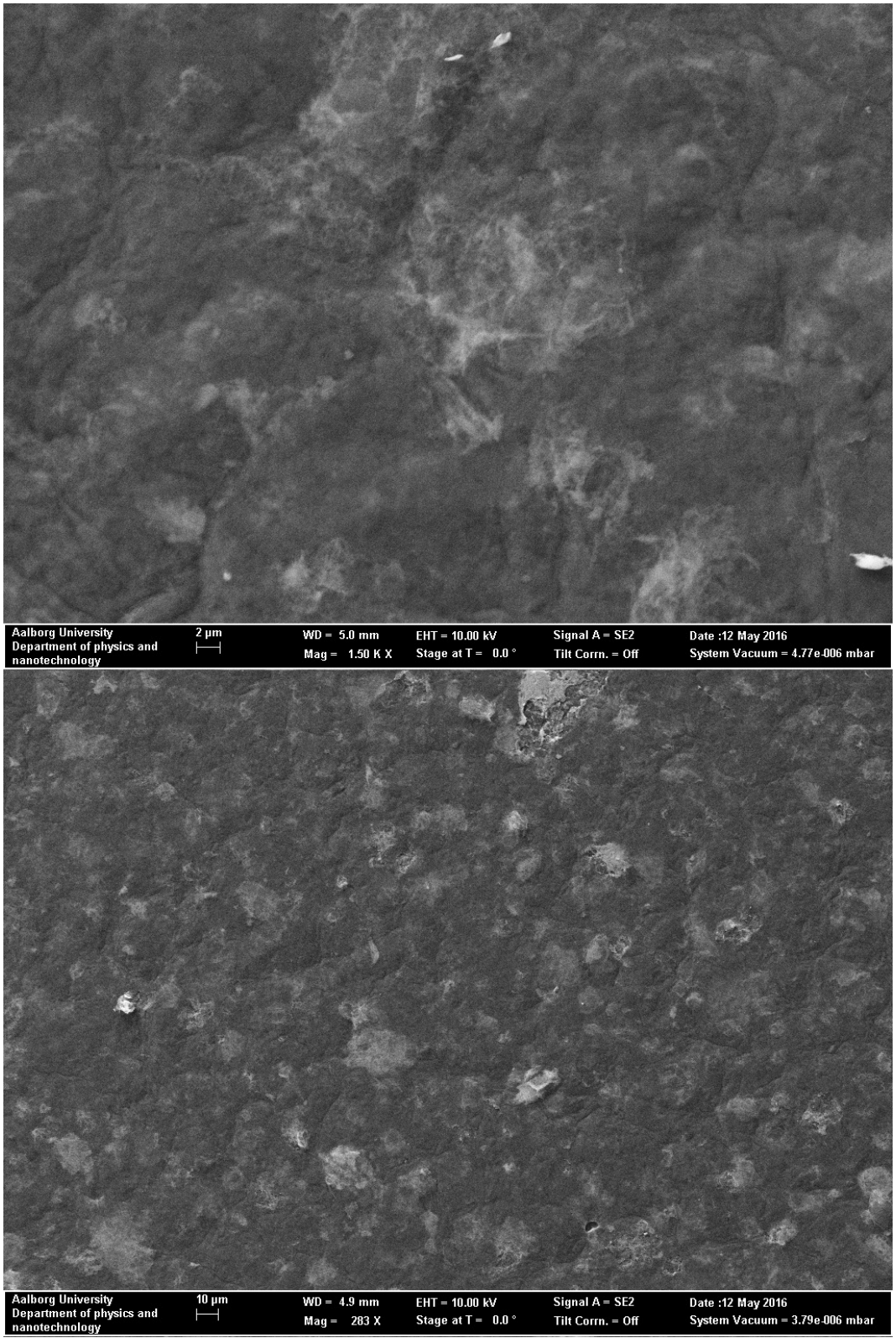

Figure 8.34: *Closeup of membrane A (high TiO_2 content) reduced at* $140°C$*, top image is without UV-C irradiation, bottom image is with 5 hours of UV-C irradiation.*

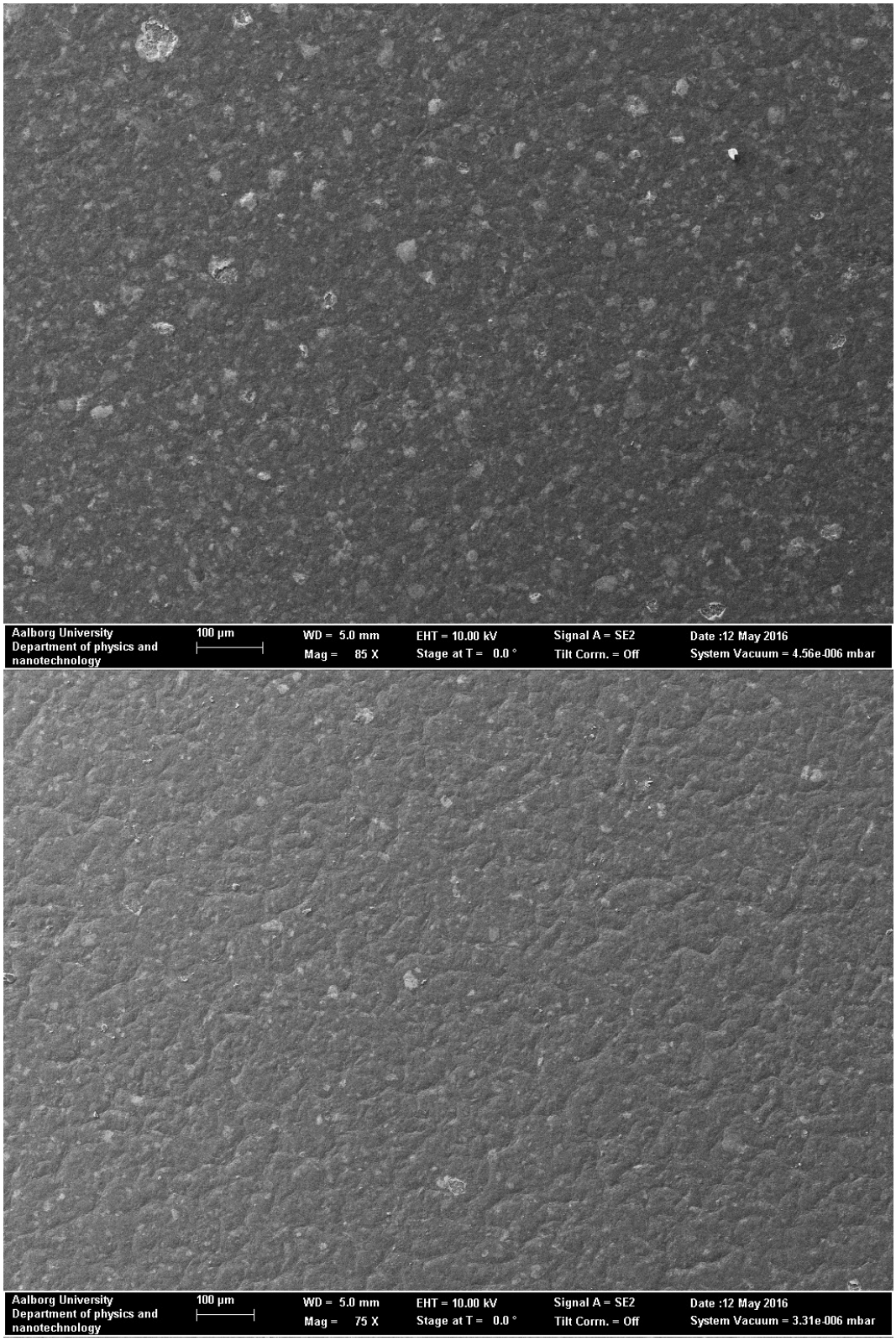

Figure 8.35: *Comparison of membrane A (high TiO_2 content) and C (low TiO_2 content) reduced at* $140°C$*, top image is membrane A, bottom image is membrane C*

When comparing pure GO membranes reduced at 140 and 160°C the structure is very similar. It is difficult to see significant differences in figure 8.31, but when comparing with figure 8.32, it appears the structure contains more wrinkles at 160°C. As we found out during TGA tests, the membranes reduced at 160°C lose significantly more mass than those at 140°C, so this would naturally cause these membranes to contract and become more wrinkled.

Looking at figure 8.33 and 8.34, no structural damage can be seen after UV-C irradiation for 5 hours. The images show that the TiO_2 is evenly divided across the surface of the A and C membranes and tend to form clusters of varying sizes. Figure 8.35 shows the difference in TiO_2 content, with the A membrane having significantly more TiO_2 in the surface, as was expected. The wrinkles seen in the pure GO membranes and C membranes cannot be seen in the A membranes; it seems that TiO_2 content smooths out the material. This also explains why initial tests with GO/TiO_2 membranes with high TiO_2 content tore when dried.

SEM-EDX mapping was also done with the A and C membrane in order to analyze the surface composition, the images will be on the following pages, see figure 8.36 and 8.37.

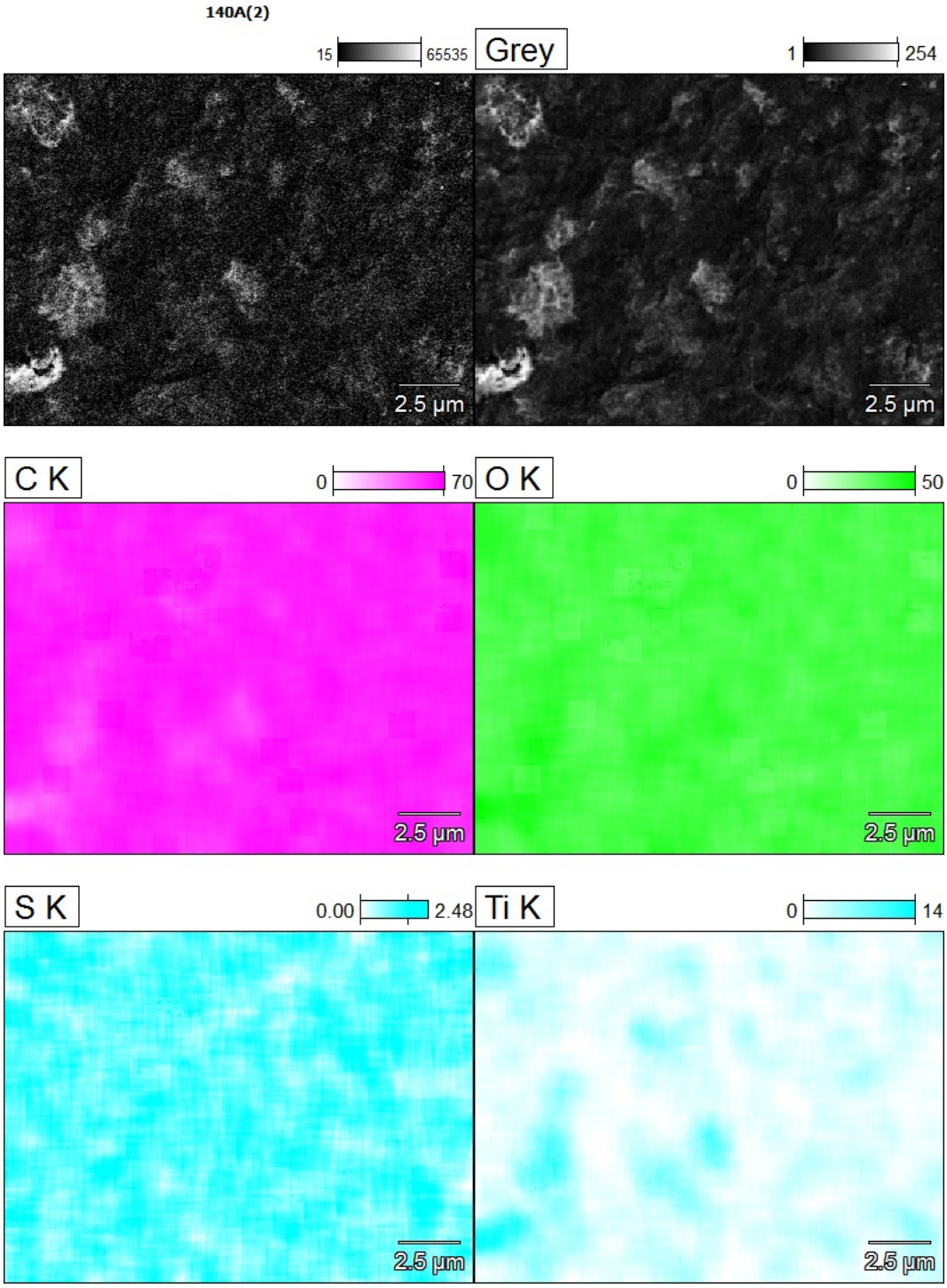

Figure 8.36: *SEM-EDX mapping of membrane A (high TiO_2 content) reduced at 140°C. Carbon, Oxygen, Sulfur and Titanium is present. The color scale indicate the surface concentration.*

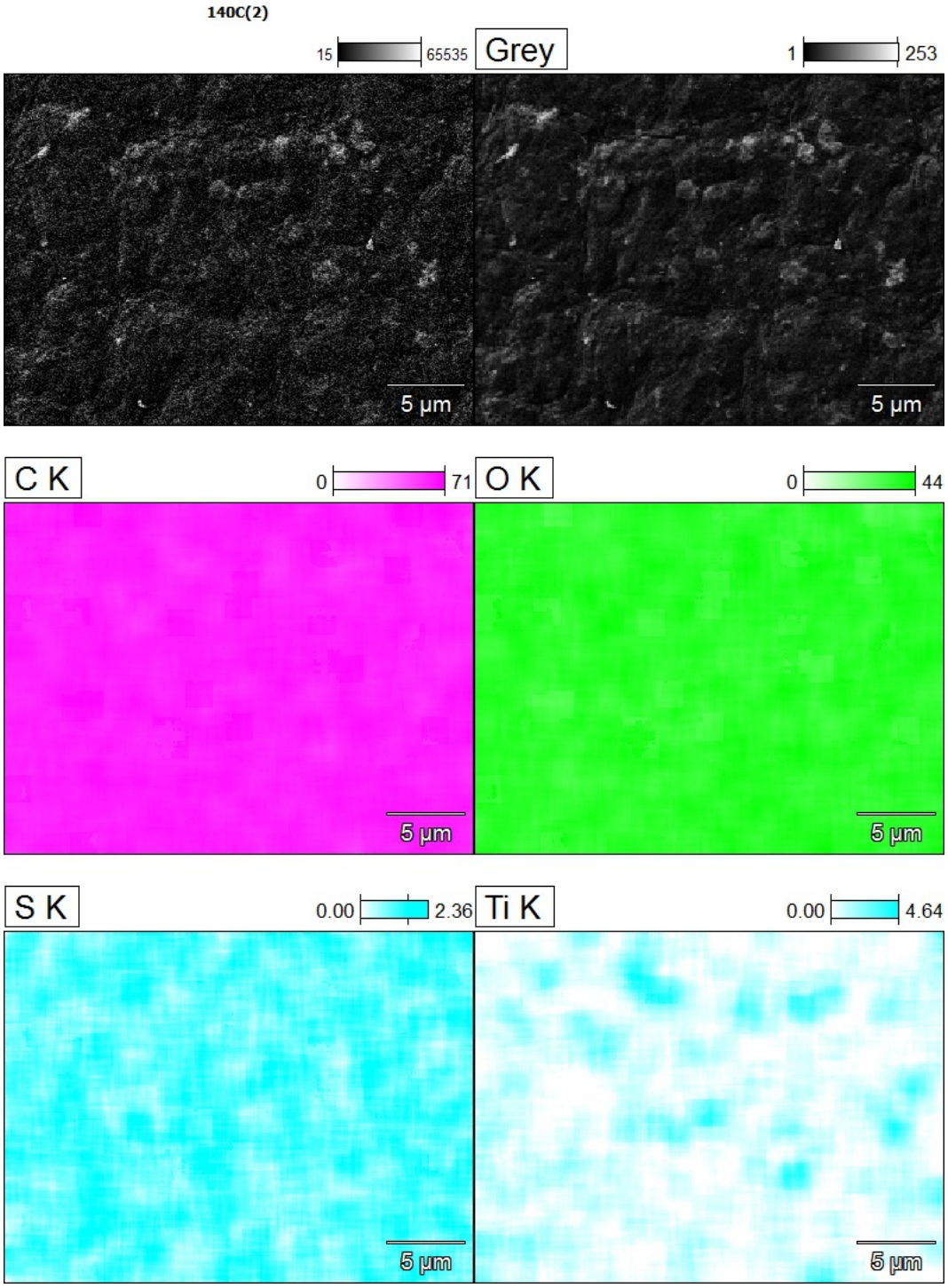

Figure 8.37: *SEM-EDX mapping of membrane C (low TiO_2 content) reduced at 140°C. Carbon, Oxygen, Sulfur and Titanium is present. The color scale indicate the surface concentration.*

Both figures show small amounts of sulfur present at the surface, which is attributed to the sulfuric acid used in synthesis. The signal for oxygen is strong across the whole surface in both the A and C membrane, once again confirming the large number of hydrophilic groups in the material. The signal

for carbon is generally strong, but the signal is weak in places corresponding to high TiO_2 content. This difference in surface composition explains what is seen in figure 8.7; the difference between mixtures is explained by PC2 which explains the difference in TiO_2 content at the surface. EDX scans were also performed in order to determine surface composition in atom %, see table 8.12.

Table 8.12: EDX scans performed on GO membranes A (high TiO_2 content) and C (low TiO_2 content) and A membranes irradiated with UV-C light for 30 minutes and 5 hours.

	Atom %			
	C K	O K	S K	Ti K
140A	61.78	34.67	1.19	2.36
140C	62.57	35.35	1.29	0.78
140A-UV 30m	61.40	35.35	1.10	2.14
140A-UV 5h	61.36	34.33	1.20	3.11

Table 8.12 confirms what was seen in the SEM images, as the TiO_2 content in the C membranes is roughly one third of that in A membranes. While the SEM images did not show visible damages to the A membrane after UV-C irradiation for 5 hours, the TiO_2 content was measured to be 32% higher in the membranes irradiated for 5 hours. This could be a coincidence explained by the tendency of large TiO_2 clusters in the material, but it could also indicate a breakdown of membrane material and thus exposing more TiO_2 particles.

9 Discussion

When doing experimental work there will always be several sources of error. This is especially true when working with material science; two membranes made from the same batch will always differ in structure to some degree. During the synthesis of GO, the oxidation of the graphite's basal planes happens at random and this results in a different composition of functional groups in different batches. During this project 9 batches of Tour were made in total, and while the properties seemed similar in all batches, this is a source of error in the experiments.

The GO synthesis chosen for experiments was the Tour method, which has FT-IR spectra and XRD results similar to that of Hummer's and Modified Hummer's method. The Modified Hummer's method had a shifted diffraction angle and significantly different FWHM than Tour's and Hummer's, which is attributed to unwanted thermal reduction during synthesis. The Tour's method also shows a smaller C-H peak in FT-IR when compared to Hummer's and Modified Hummer's, indicating that there is less leftover hydrophobic material in this synthesis. When comparing with the knowledge gained in the theory section, it can be discussed whether or not the literature is applicable to our project, as the articles found used Hummer's or Modified Hummer's for GO synthesis. However, the overall results and especially FT-IR and XRD results can be used as a strong argument for comparison.

The FT-IR analysis of GO membranes revealed that the difference between a reduction temperature of 140 and 160°C is the loss of hydroxyl groups, and thus a rise in C-H groups in membranes reduced at 160°C. When analyzing the data using PCA, there were clear groupings as a result of UV-C irradiation. PC1 clearly describes this difference in the scores plot, and while PC1 is shown to describe variance in the hydroxyl group area of the data, there is still the possibility that this is caused by membrane damage and not added hydroxyl groups. The theory of superhydrophilicity as a result of added hydroxyl groups is supported by the zeta potential and SEM results; the zeta potential increased after UV-C irradiation and was greater in membranes with higher TiO_2 content, clearly indicating the presence of additional hydroxyl groups. The SEM results also did not indicate any membrane damage, although the EDX-measurement of membrane A showed higher TiO_2 content in the surface after UV-C irradiation for 5 hours. This is expected to be random and caused by the randomized large clusters of TiO_2 divided across the membrane surface.

If the laser for Raman spectroscopy had worked, any potential breakdown of membrane material might have been visible when analyzing the data. The PCA analysis of FT-IR spectra also showed groupings on the scores plot according to TiO_2 content in the samples, described by PC2. This is supported by the SEM results, where the A membranes clearly has more TiO_2 in the surface compared to C membranes.

The drop shape analysis shows a big difference between membranes reduced at 140 and 160°C in terms of hydrophilicity. Based on the results in FT-IR, this is believed to be caused by a removal of significantly more hydroxyl groups at 160°C, also apparent in the TGA results comparing the reduction temperatures. The result is a very low polar component and surface polarity for membranes reduced at 160°C compared to 140°C. This difference is lessened significantly when the 160°C membranes are irradiated with UV-C, with the A membrane going from a contact angle of $78,9°$ to $20,8°$ with water and ending up with a polar component and surface polarity similar to membranes reduced at 140°C. This is again closely related to TiO_2 content, as the B and C membranes at 160°C end up with contact angles of $36,3°$ and $42,5°$, respectively.

The membrane mixtures reduced at 140°C reach the same contact angle with water after 30 mins UV-C irradiation and therefore TiO_2 content does not seem as important as when reducing at 160°C. The contact angle seems to follow an exponentially decreasing function when looking at membranes reduced at 140°C. This tendency is not as clear in the membranes reduced at 160°C, which could be caused by differences in surface structure.

During thermal reduction tests it was determined that temperatures above 160°C would not be used, as the material became too brittle and disintegrated on touch when handled. Furthermore, explosions were a big problem when reducing membranes at 160°C and above, because the heating rate had to be adjusted to $2,5°C/min$ after 140°C to avoid explosions. This phenomena was researched in literature and with TGA and DSC tests. As expected the explosion was dependent on sample mass, confirming that the explosions happened because the heat from the exothermic reduction reaction cannot dissipate to the surroundings fast enough.

When comparing the DSC results to literature in the theory section, the onset temperature for exothermic reaction is different; the onset temperature in literature was found to be 150°C, while results in this project found an onset temperature of 135°C. The literature also describes how the onset temperature is lower when soaking the samples in KOH prior to reduction. The difference in onset temperature might therefore be caused by higher potassium and hydroxyl content in the sample tested in this project. At the onset temperature, the reduction in material is no longer caused by water loss but hydroxyl groups. This explains why reducing the membranes at 140°C is just

enough to produce stable membranes, while the membranes reduced at 120°C dissolved when tested during zeta potential measurements.

While the experiments done in this project indicate that reduction is most optimal at 140°C, this was very dependent on the cylindrical oven used, where the membranes had to be stacked. Knowing that mass transfer limitations is the main culprit in explosions during reduction, it could be possible to reduce very thin membranes at higher temperatures. When interpreting the DSC and TGA results, there is a rapid weight loss around $180 - 200°C$, and it might therefore be an opportunity to do thermal treatment quickly at high temperatures, if the membranes are thin enough. This could be applicable to commercial production, where membranes are intentionally modified to have thin selective layers, in order to reduce flux.

The zeta potential measurements indicate membrane stability in the region of pH 4-9, and a selected membrane was tested to see zeta potential in low and high pH, resulting in an isoelectric point around pH 12. However, these measurements in high and low pH come with significant error, as the pH electrode in the machine is calibrated to a pH range of 4-9. As previously mentioned, it is evident that TiO_2 content determines the difference in zeta potential when irradiating the samples with UV-C.

During testing with the NF99HF and NFT50 PA NF membranes from Alfa Laval, it was clear that these membranes had been modified for high hydrophilicity and surface polarity. While the commercial membranes appear much more hydrophilic in drop shape analysis results, the WVT and permeance is significantly lower than that of GO membranes. The first permeation test with GO membranes indicates that permeation of water is close to unimpeded, as described in literature. When compared to the commercial membranes, the permeance is twice as high for GO membranes. However, the first permeation test used a different glue than in the second and third permeation tests, where the permeation of commercial membranes was tested. During these tests the A 140 membrane was also included as a control, and the WVT and permeance of water through the A 140 membrane was 50% higher as opposed to twice as high. This difference might be because a different GO batch was used, but it might also be because only the epoxy glue was leak tight.

When ethanol and hexane was tested, it was expected that hexane would be blocked, while small amounts of ethanol might pass through due to it's hydroxyl group. As expected, the hexane was almost completely blocked, while larger amounts of ethanol pass through.

10 Conclusion

From the different GO syntheses tested, the FT-IR spectra of Tour's method is similar to that of Hummer's and Modified Hummer's, with the exception of a larger C-H peak for Hummer's and Modified Hummer's. This confirms what was found in literature, where Hummer's and Modified Hummer's method were found to contain more hydrophobic under-oxidized carbon material. The XRD results were also similar when comparing Hummer's and Tour's method. Based on these findings and the fact that the Tour's method is also the easiest synthesis in terms of laboratory work hours, it is concluded that the Tour's method is the best synthesis of GO for experiments.

During experiments it was found that reduction temperatures should be kept between $140 - 160°C$ for one hour; the membranes reduced at $120°C$ dissolved when their zeta potential was tested, and the membranes reduced above $160°C$ became too brittle. From these experiments it can be concluded that the optimal thermal treatment was $140°C$, as these membranes showed the highest hydrophilicity in the contact angle measurements, explained by the higher loss of hydroxyl groups in $160°C$ reduction, which can also be seen in FT-IR and XRD results.

The thermal reduction was also studied with DSC and TGA. From DSC it can be concluded that the exothermic reaction starts around $135°C$ and peaks in the range of $180 - 200°C$. Combining this with the knowledge gained from FT-IR results, it can be concluded that hydroxyl groups will be removed starting from $135°C$ and rapidly dissipate around the exothermic reaction peak at $180 - 200°C$. The TGA measurements show a weight loss of 34.15% at $140°C$ and 47.1% at $160°C$. As previously described, FT-IR results show that the difference is loss of hydroxyl groups; this leads to a less hydrophilic and more compact material, as seen from DSA and XRD results.

The GO/TiO_2 ratio was thoroughly tested and high TiO_2 contents caused the membranes to become brittle and tear upon drying. The A mixture with the highest TiO_2 content has a GO/TiO_2 ratio of 15:1, which seemed to be close to the limit of maximum TiO_2 content possible without membrane tearing. When reducing the membranes at $140°C$, all membrane mixtures ended up with a contact angle around 20° when tested with water droplets after 30 mins of UV-C irradiation. Therefore, it can be concluded that the optimal GO/TiO_2 ratio is between 15:1 (mixture A) and 30:1 (mixture C), but it is

possible that even less TiO_2 can be used and still reach the same effect.

The membranes' surface characteristics are mainly determined by reduction temperature, as previously described. When reducing at $160°C$ the contact angles for water was in the range of approximately $80 - 85°$, compared to $50 - 55°$ for membranes reduced at $140°C$ (excluding the C membrane, which measured 65°). The membranes with TiO_2 had higher hydrophilicity than pure GO membranes (again excluding C $140°C$), while also having a larger dispersive component. The contact angle for diiodomethane on membranes with TiO_2 was around 10° lower than that of pure GO membranes. The membranes all had stable zeta potentials in the region of pH 4-9.

When the membranes with TiO_2 were irradiated with UV-C light, there were significant changes in surface characteristics. From DSA it can be concluded that the membranes become more hydrophilic when irradiated with UV-C, and that the time needed for maximum effect is 30 mins. The membranes reduced at $140°C$ end up with similar contact angles for water despite TiO_2 content, but the membranes reduced at $160°C$ are divided according to TiO_2 content. The duration of effect was tested and it can be concluded that the hydrophilicity induced by UV-C irradiation lasts approximately 10 minutes, before returning to baseline values after 60 minutes.

This change in surface characteristics is supported by the results in FT-IR and zeta potential measurements. When analyzing the FT-IR results with PCA, there are clear groupings according to UV-C irradiation on the scores plots. This difference is concluded to be caused by the formation of hydroxyl groups, as described in the TiO_2 theory chapter. The zeta potential is also increased after UV-C irradiation; membranes with higher TiO_2 content have higher increases in zeta potential, which based on the theory, DSA and FT-IR is concluded to be due to an increase in hydroxyl groups at the surface. Higher TiO_2 content therefore means more hydroxyl groups created.

Based on the abovementioned information, it was concluded that TiO_2 addition to GO membranes provides anti-fouling properties as a result of hydroxyl groups formed at the surface. The hydroxyl groups give the membranes a more negative surface charge and higher hydrophilicity, thus providing the anti-fouling properties discussed in the membrane theory chapter. The SEM images were inconclusive as to whether or not the free radicals formed by TiO_2 also break down the membrane, but the images obtained showed no visual damage.

The first permeance test with GO membranes showed that the water vapor permeation was close to unimpeded. The permeance of hexane and ethanol was also tested, where the open test tube with hexane had a weight loss approximately 10 times higher than the test tubes with GO membranes. When testing with ethanol, the open test tube had a weight loss approximately 3

times higher than ethanol. While the commercial Alfa Laval NF99HF and NFT50 membranes exhibit better hydrophilicity and higher surface polarity, it can be concluded from water vapor permeation tests that GO membranes have significantly higher water permeance. The first permeation test shows water permeance in GO to be over twice that of the commercial membranes, while the A 140 membrane tested along with the commercial membranes has a permeance that is 55% higher. From these results it is concluded that GO membranes have excellent permeance of water and are therefore suitable for water treatment.

11 Perspectivation

The work done in this project is considered to be groundwork for further research. When producing these membranes and testing them, there are several different factors that can be optimized. The reduction temperature in this project found to be the most optimal was $140°C$, but this was largely due to the oven used and the thickness of the membranes. If the membranes were to be made commercially, they would most likely be spraycoated or spincoated onto a more porous UF support, and the selective GO layer would be much thinner than the membranes produced in this project. This could make it possible to reduce the membranes at higher temperatures without causing an explosion, as the thermal runaway reaction is caused by the buildup of gases that cannot escape the material at a high enough rate. If the membranes can be reduced at higher temperatures it would reduce the reduction time required. This is also evident when looking at the TGA graph ramped up to $300°C$. There is a rapid weight loss in the temperature range of $180 - 220°C$, which is mainly attributed to the loss of hydroxyl-groups. It could therefore be a possibility to reduce the membranes in this temperature range in order to achieve a lower reduction time.

Another thing to test further is the ratio of GO/TiO_2 and the UV-C light intensity used. The amount of TiO_2 necessary for the desired effect could be directly correlated to the light intensity, which was set to 2 mW/cm^2 in this project. Further tests could therefore help determine an optimal GO/TiO_2 ratio.

Tweaking the size of the TiO_2 particles by changing the parameters of the synthesis to generate different particle sizes and testing their effects, as they might influence the optimal GO/TiO_2 ratio.

The permeation tests in this project were limited to vapor tests, as the membranes were fragile and would require being mounted on a porous UF support, as is commonly done with NF membranes. For further testing it would be interesting to mount a GO membrane and test it with liquid and see how it performs. During these tests, the anti-fouling properties could also be tested by intentionally fouling the membranes and testing if UV-C irradiation can reduce the fouling.

Raman was attempted in this project, but the wavelength of the laser was

not suitable for black samples, so no results were obtained. Raman could show any potential differences in C-C, C-H and C=C bonds, and it is recommended to obtain this data before and after UV-C irradiation and analyze them with PCA, in order to see if there is a breakdown of the membrane itself. This should be combined with additional SEM analysis for the same purpose.

In order to gain knowledge of the membrane surface area and pore size, Brunauer-Emmett-Teller (BET) analysis is also recommended for further testing.

Bibliography

[1] P. Mukhopadhyay and R. Gupta, *Graphite, Graphene, and Their Polymer Nanocomposites*. Taylor & Francis, 2012.

[2] J. Li, X. Zeng, T. Ren, and E. van der Heide, "The preparation of graphene oxide and its derivatives and their application in bio-tribological systems," *Lubricants*, vol. 2, no. 3, pp. 137–161, 2014.

[3] D. Konios, M. M. Stylianakis, E. Stratakis, and E. Kymakis, "Dispersion behaviour of graphene oxide and reduced graphene oxide," *Journal of Colloid and Interface Science*, vol. 430, pp. 108 – 112, 2014.

[4] W. Gao, *Graphene Oxide: Reduction Recipes, Spectroscopy, and Applications*. Springer International Publishing, 2015.

[5] A. L. Higginbotham, D. V. Kosynkin, A. Sinitskii, Z. Sun, and J. M. Tour, "Lower-defect graphene oxide nanoribbons from multiwalled carbon nanotubes," *ACS Nano*, vol. 4, no. 4, pp. 2059–2069, 2010. PMID: 20201538.

[6] D. C. Marcano, D. V. Kosynkin, J. M. Berlin, A. Sinitskii, Z. Sun, A. Slesarev, L. B. Alemany, W. Lu, and J. M. Tour, "Improved synthesis of graphene oxide," *ACS Nano*, vol. 4, no. 8, pp. 4806–4814, 2010. PMID: 20731455.

[7] L. Peng, Z. Xu, Z. Liu, Y. Wei, H. Sun, Z. Li, X. Zhao, and C. Gao, "An iron-based green approach to 1-h production of single-layer graphene oxide," *Nat Commun*, vol. 6, Jan 2015. Article.

[8] S. Huh, *Thermal Reduction of Graphene Oxide*. INTECH Open Access Publisher, 2011.

[9] Y. Qiu, F. Guo, R. Hurt, and I. KÃ$\frac{1}{4}$laots, "Explosive thermal reduction of graphene oxide-based materials: Mechanism and safety implications," *Carbon*, vol. 72, pp. 215 – 223, 2014.

[10] R. Joshi, S. Alwarappan, M. Yoshimura, V. Sahajwalla, and Y. Nishina, "Graphene oxide: the new membrane material," *Applied Materials Today*, vol. 1, no. 1, pp. 1 – 12, 2015.

[11] R. Singh, *Membrane Technology and Engineering for Water Purification: Application, Systems Design and Operation*. Elsevier Science, 2014.

[12] R. Baker, *Membrane Technology and Applications*. Wiley, 2012.

[13] "Membrane classification," 2016. [Online; accessed 16-May-2016].

[14] H. Huang, Y. Ying, and X. Peng, "Graphene oxide nanosheet: an emerging star material for novel separation membranes," *J. Mater. Chem. A*, vol. 2, pp. 13772–13782, 2014.

[15] K. Peinemann and S. Nunes, *Membrane Technology, Volume 4: Membranes for Water Treatment*. Membranes, Wiley, 2010.

[16] N. Li, A. Fane, W. Ho, and T. Matsuura, *Advanced Membrane Technology and Applications*. Wiley, 2011.

[17] E. Sogaard, *Chemistry of Advanced Environmental Purification Processes of Water: Fundamentals and Applications*. Elsevier Science, 2014.

[18] "Titanium dioxide." `https://en.wikipedia.org/wiki/Titanium_dioxide`. Visited: 23/11/2015.

[19] A. Khataee and G. Mansoori, *Nanostructured Titanium Dioxide Materials: Properties, Preparation and Applications*. 2011.

[20] U. Diebold, "The surface science of titanium dioxide," *Surface Science Reports*, vol. 48, no. 5-8, pp. 53–229, 2003.

[21] "Comparison of raman and ir spectroscopy." `http://www.chemvista.org/ramanIR4.html`. Online; accessed 4-June-2016.

[22] "Raman and ftir spectroscopy: Complementary technologies for chemical and explosives identification." `https://tools.thermofisher.com/content/sfs/brochures/Raman-FTIR-TechNote-Final.pdf`. Online; accessed 4-June-2016.

[23] Wikipedia, "Bragg's law — wikipedia, the free encyclopedia," 2016. [Online; accessed 3-May-2016].

[24] T. Cosgrove, *Colloid Science: Principles, Methods and Applications*. Colloid Science: Principles, Methods and Applications, John Wiley & Sons, 2010.

[25] Wikipedia, "Zeta potential — wikipedia, the free encyclopedia," 2016. [Online; accessed 17-May-2016].

[26] C. Rulison, "Two-component surface energy characterization as a predictor of wettability and dispersability,"

[27] Wikipedia, "Scanning electron microscope — wikipedia, the free encyclopedia," 2016. [Online; accessed 6-June-2016].

[28] "How scanning electron microscopes work," 2016. Online; accessed 6-June-2016.

[29] Wikipedia, "Energy-dispersive x-ray spectroscopy — wikipedia, the free encyclopedia," 2016. [Online; accessed 6-June-2016].

[30] "Scanning electron microscope," 2016. [Online; accessed 6-June-2016].

[31] "Chemical and element maps," 2016. [Online; accessed 6-June-2016].

[32] L. B. Paulchamy B, Arthi G, "A simple approach to stepwise synthesis of graphene oxide nanomaterial," *Journal of Nanomedicine and Nanotechnology*, vol. 6, 2015.

A Appendix

In the appendix, supplementary material for the report can be found.

A.1 Tour method detailed

The Tour's method is a further improved synthesis which uses a 9:1 mixture of concentrated H_2SO_4/H_3PO_4 and a 6:1 mixture of $KMnO_4/Graphite$. The synthesis is as follows:

1. Concentrated $H_2SO4/H3PO_4$ (360:40 mL) was added to a 1000 mL volumetric flask containing graphite flakes (3 g) and KMnO4 (18 g), producing a slightly exothermic reaction $(35 - 40°C)$.

2. The solution was then heated to $50°C$ and stirred for 12 hours.

3. The solution was then cooled to room temperature in an ice bath, and 400 mL of water was slowly added to the reaction, keeping the temperature below $60°C$. The synthesis is then terminated using approximately 3 mL H_2O_2 (30%), creating an orange solution when the termination is complete, see figure A.1.

Figure A.1: *Before and after addition of* H_2O_2

4. In order to speed up precipitation, the solution is then divided evenly into two beakers and deionized water is added. When the GO has precipitated, the solutions are decanted, see figure A.2.

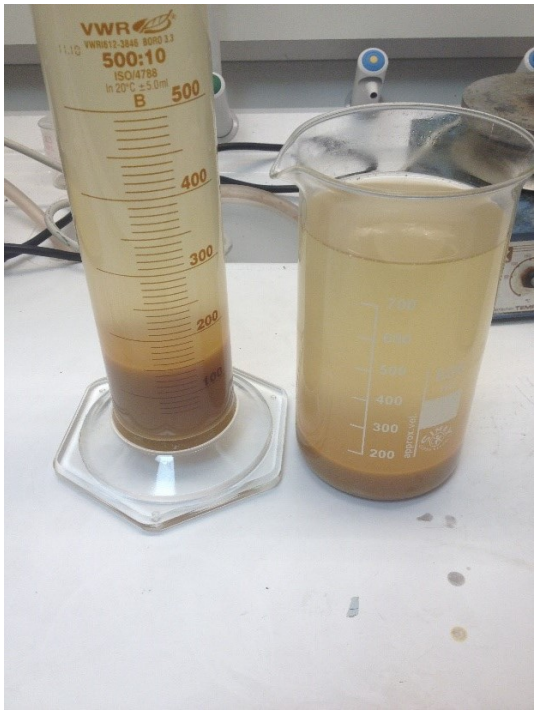

Figure A.2: *GO solutions before decanting.*

5. The GO was then dissolved into 1 M *HCl* using spatulas and centrifuged 3 times at 6000 RPM for 10 minutes each run, see figure A.3.

Figure A.3: *Before and after HCl centrifugation.*

6. Following the HCl wash, the GO was centrifuged 4 times with deionized water at 6000 RPM for at least 4 hours each run. The amount of GO solution will increase as water builds up in the material, see figure A.4.

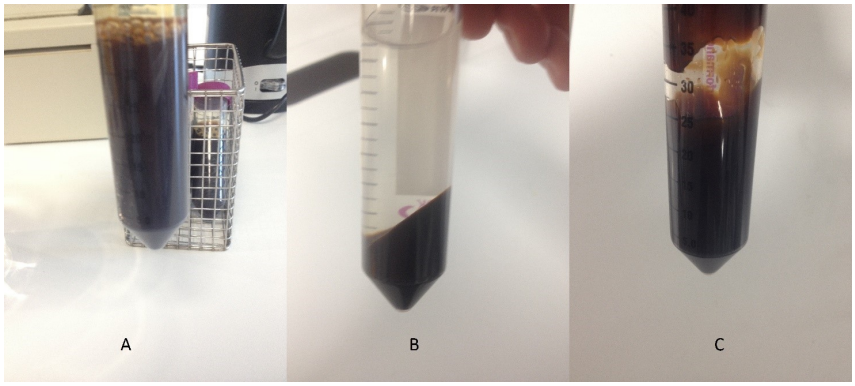

Figure A.4: *Centrifugation with water at different stages; A: Second wash with water before centrifugation, B: Second wash with water after centrifugation, C: After the final wash.*

7. After centrifugation a stock solution was made of the cleansed GO. The stock solution was approximately 200 mL every time.

A.2 XRD Calculations

For this example, the measurement made for pure GO reduced at $140°C$ will be used. The first step is to calculate the distance between layers, d, using Bragg's law:

$$d = \frac{n\lambda}{2 \times \sin\theta}$$

Where n is the first peak (value 1), λ is the wavelength (0,1789 nm), and θ is the angle in radians, corresponding to the highest count. The first step is to convert 2θ from degrees to radians:

$$\theta(rad) = \frac{2\theta(deg) \times \pi}{2 \times 180}$$

$$\theta(rad) = \frac{12.11 \times \pi}{2 \times 180} = 0.105$$

This can now be used in the equation derived from Bragg's law to determine the distance between layers, d:

$$d = \frac{1 \times 0.1789nm}{2 \times \sin 0.105} = 0.848$$

	Water (mN/m)	Diiodomethane (mN/m)
Surface tension	72,8	50,8
Dispersive component	26,4	50,8
Polar Component	46,4	0

The next step is to obtain the thickness of the stacking layers, D, using the Scherrer equation:

$$D_{002} = \frac{K\lambda}{\beta \cos\theta}$$

Where D is the thickness of the layers, K is the Warren shape constant (0.9), λ is the wavelength (0.1789 nm), β is the FWHM, θ is the angle. The FWHM is obtained in degrees and therefore also has to be converted to radians:

$$\beta = \frac{0.7397 \times \pi}{180} = 0.013$$

The thickness of the layers can now be calculated:

$$D = \frac{0.9 \times 0.1789nm}{0.013 \times \cos 0.105} = 12.54nm$$

Now that we have d and D, we can calculate the number of layers using the following equation:

$$N_{layers} = \frac{12.54nm}{0.848nm} = 14.78$$

A.3 DSA Calculations

When calculating the surface energy of a solid material, it is necessary to test the material with at least two different liquids. The Good's equation is used to calculate the polar and dispersive components of the membranes:

$$(\gamma_s^D \gamma_l^D)^{\frac{1}{2}} + (\gamma_s^P \gamma_l^P)^{\frac{1}{2}} = \gamma_l \cos(\theta + 1)/2$$

In these experiments we chose water and diiodomethane, because while water has both a polar and dispersive component to its surface tension, diiodomethane only has a dispersive component:

This way the Good's equation can be reduced to the following:

$$\gamma_s^D = \frac{\gamma_l}{4} \cos(\theta + 1)^2$$

The dispersive component of the membrane can therefore be found and used in Good's equation to find the polar component and thereafter calculate

Water	52,96
Diiodomethane	39,72

the total surface energy. For this example, we will use measurements from a pure GO membrane reduced at $140°C$ with the following contact angles:

The first step is to calculate the dispersive component of the membrane:

$$\gamma_s^D = \left(\frac{50,8\frac{mN}{m}}{4}\right)(\cos(39,72)+1)^2 = 39,75\frac{mN}{m}$$

The Good's equation can now be solved:

$$\left(39,75\frac{mN}{m} \times 26,4\frac{mN}{m}\right)^{\frac{1}{2}} + \left(\gamma_s^P \times 46,4\frac{mN}{m}\right)^{\frac{1}{2}} = 72,8\frac{mN}{m} \times \frac{\cos(52,96)+1}{2}$$

$$\gamma_s^P = 14,49\frac{mN}{m}$$

The total surface energy is then:

$$\gamma_s = \gamma_s^P + \gamma_s^D = 14,49\frac{mN}{m} + 39,75\frac{mN}{m} = 54,24\frac{mN}{m}$$

The surface polarity can then be calculated:

$$\left(\frac{14,49\frac{mN}{m}}{54,24\frac{mN}{m}}\right) \times 100\% = 26,71\%$$

A.4 WVT and Permeability calculations

For this sample calculation, the data from a pure GO membrane reduced at $140°C$ and tested with hexane will be used. The following equation is used to determine the WVT:

$$WVT = \frac{w_0 - w_{48}}{t \times A}$$

Where w_0 is the start weight and w_{48} is the weight at the end of the experiment (95 hours later). T is the elapsed time, and A is the section area of the glas. The glas diameter was measured to be $0,0135m$ and is used to obtain the section area:

$$A = \frac{\pi}{4} \times D^2 = \frac{\pi}{4} \times (0,0135m)^2 = 1,43 \times 10^{-4}m^2$$

The WVT can now be calculated:

$$WVT = \frac{12,78g - 12,7449g}{95 \times 3600 \times 1,43 \times 10^{-4}m^2} = 1,42 \times 10^{-3}\frac{g}{s \times m^2}$$

The permeance can then be calculated using the following equation:

$$Permeance = \frac{WVT}{P_s(R_1 - R_2)}$$

Where P_s is the saturation vapour pressure, R_1 is the relative humidity inside the tube, R_2 is the relative humidity outside the tube. The relative humidity inside the tube is set to 100%, while the humidity outside the tube is set to 35%. The saturation vapour pressure for water was found in thermodynamic tables, Antoine's equation was used to calculate the saturation vapour pressure for hexane and ethanol:

$$P_s = 10^{A-\frac{B}{C+T}}$$

Where A, B and C are Antoine equation parameters and T is the temperature in $°C$. The resulting pressure will be in $mmHg$. Inserting the Antoine equation parameters and temperature we get:

$$P_s = 10^{7,01051-\frac{1246,33}{232,988+35}} = 229mmHg = 30,53kPa$$

Given this information, the permeance can be calculated:

$$Permeance = \frac{1,42 \times 10^{-3}\frac{g}{s \times m^2}}{30,53kPa(1 - 0,35))} = 7,15 \times 10^{-5}\frac{g}{m^2 \times s \times kPa}$$

A140

Titration Source	Solute	Concentration [g/l]	Titration Vol [ml]	Measuring Step Parameter Set	pH	Conductivity [mS/m]	Cell Resistance [KOhm]	ζ [mV]	ζ Stdev	Elapsed Time [min]
TU1	NaOH(aq)	4	0	Z_R300_150_P400I_20	4,9578715	16,252994	88,908549	-24,054071	0,3726236	3,3766333
TU1	NaOH(aq)	4	0,05	Z_R300_150_P400I_20	5,4881166	15,879226	89,709249	-24,023881	0,5418863	6,7280333
TU1	NaOH(aq)	4	0,03	Z_R300_150_P400I_20	6,9522258	16,109238	89,642725	-24,425811	0,6050231	10,062283
TU1	NaOH(aq)	4	0,03	Z_R300_150_P400I_20	8,0968603	16,224281	89,189439	-24,694658	0,1670733	13,396533
TU1	NaOH(aq)	4	0,03	Z_R300_150_P400I_20	8,4347653	16,404566	88,064992	-24,905541	0,1481147	16,730783
TU1	NaOH(aq)	4	0,05	Z_R300_150_P400I_20	8,7502331	16,578157	86,094154	-25,141889	0,6302385	20,065033
TU1	NaOH(aq)	4	0,27	Z_R300_150_P400I_20	9,4907333	17,490368	78,974835	-28,050592	3,5546098	23,45075
TU1	NaOH(aq)	4	0,4	Z_R300_150_P400I_20	9,8985421	19,281668	72,388435	-25,259078	3,0225818	26,853367
TU1	NaOH(aq)	4	0,6	Z_R300_150_P400I_20	10,195123	22,058689	65,74983	-25,177852	3,8853677	30,256517
TU1	NaOH(aq)	4	1,2	Z_R300_150_P400I_20	10,500317	27,711553	56,181285	-28,894534	6,7090434	33,813833
TU1	NaOH(aq)	4	2,2	Z_R300_150_P400I_20						

B140

Titration Source	Solute	Concentration [g/l]	Titration Vol [ml]	Measuring Step Parameter Set	pH	Conductivity [mS/m]	Cell Resistance [KOhm]	ζ [mV]	ζ Stdev	Elapsed Time [min]
TU1	NaOH(aq)	4	0	Z_R300_150_P400I_20	4,7987133	16,848566	92,898385	-35,499008	0,684308	3,3859859
TU1	NaOH(aq)	4	0,08	Z_R300_150_P400I_20	6,1844342	16,666293	96,311214	-35,959395	1,284251	6,7717119
TU1	NaOH(aq)	4	0,03	Z_R300_150_P400I_20	8,5162993	16,789089	96,964383	-35,823759	0,7251345	10,157438
TU1	NaOH(aq)	4	0,1	Z_R300_150_P400I_20	8,9718175	16,49887	95,898843	-36,123379	1,1636905	13,508844
TU1	NaOH(aq)	4	0,4	Z_R300_150_P400I_20	9,7184198	17,87128	87,585523	-41,038806	5,921152	16,92889
TU1	NaOH(aq)	4	0,8	Z_R300_150_P400I_20	10,188773	21,770603	77,838918	-36,707334	9,3038054	20,366096
TU1	NaOH(aq)	4	1,4	Z_R300_150_P400I_20	10,507081	25,14545	68,032355	-33,276748	5,4958142	23,820462
TU1	NaOH(aq)	4	2,4	Z_R300_150_P400I_20	10,812365	35,576087	55,522092	-34,566877	7,8636155	27,377528
TU1	NaOH(aq)	4	4	Z_R300_150_P400I_20						

C140

Titration Source	Solute	Concentration [g/l]	Titration Vol [ml]	Measuring Step Parameter Set	pH	Conductivity [mS/m]	Cell Resistance [KOhm]	ζ [mV]	ζ Stdev	Elapsed Time [min]
TU1	NaOH(aq)	4	0	Z_R300_150_P400I_20	4,628423	16,621335	97,291758	-38,646814	1,4208681	3,3685659
TU1	NaOH(aq)	4	0,2	Z_R300_150_P400I_20	5,8605863	16,452914	104,68978	-39,725127	0,770989	6,7714519
TU1	NaOH(aq)	4	0,02	Z_R300_150_P400I_20	8,5707534	16,620005	106,45919	-40,804436	0,7429218	10,174338
TU1	NaOH(aq)	4	0,13	Z_R300_150_P400I_20	9,0625411	17,069328	105,5907	-40,735316	1,2960023	13,560064
TU1	NaOH(aq)	4	0,4	Z_R300_150_P400I_20	9,7089334	18,519474	94,109273	-47,761598	5,5882535	17,10023
TU1	NaOH(aq)	4	0,6	Z_R300_150_P400I_20	10,088656	20,879583	82,230141	-38,988494	12,59812	20,726196
TU1	NaOH(aq)	4	1,2	Z_R300_150_P400I_20	10,437618	25,951915	71,946985	-34,259453	4,9608789	24,335003
TU1	NaOH(aq)	4	2,4	Z_R300_150_P400I_20	10,769516	35,217706	62,104372	-35,68557	1,0228574	27,995289
TU1	NaOH(aq)	4	4	Z_R300_150_P400I_20	11,056171	52,214382	52,520953	-39,062149	0,6206628	31,766596

A160

Titration Source	Solute	Concentration [g/l]	Titration Vol [ml]	Measuring Step Parameter Set	pH	Conductivity [mS/m]	Cell Resistance [KOhm]	ζ [mV]	ζ Stdev	Elapsed Time [min]
			0		4,47	16,04	60,48	-38,72		3,4
			0,2		5,7	15,83	65,76	-39,71		6,9
			0,02		6,3	15,05	68,74	-40,32		10,4
			0,02		7,3	16,05	70,68	-41,05		13,9
			0,02		7,84	15,31	71,98	-42,13		17,5
			0,03		8,28	16,06	72,67	-42,17		21,2
TU1	NaOH(aq)	4	0	Z_R300_150_P400I_20	8,4560029	16,276751	74,826418	-40,039167	0,287709	3,3514
TU1	NaOH(aq)	4	0,06	Z_R300_150_P400I_20	8,7507549	14,693019	73,991013	-39,933581	0,7279766	6,6853833
TU1	NaOH(aq)	4	0,27	Z_R300_150_P400I_20	9,4567944	15,611928	70,020983	-45,777784	3,5218997	10,13975
TU1	NaOH(aq)	4	0,4	Z_R300_150_P400I_20	9,8630822	18,464598	63,821404	-47,006904	6,9505901	13,594117
TU1	NaOH(aq)	4	0,8	Z_R300_150_P400I_20	10,228354	21,400093	57,183371	-34,180295	2,2982442	17,09945
TU1	NaOH(aq)	4	0,2	Z_R300_150_P400I_20						

B160

Titration Source	Solute	Concentration [g/l]	Titration Vol [ml]	Measuring Step Parameter Set	pH	Conductivity [mS/m]	Cell Resistance [KOhm]	ζ [mV]	ζ Stdev	Elapsed Time [min]
TU1	NaOH(aq)	4	0	Z_R300_150_P400I_20	4,7489093	16,930496	72,729671	-35,271578	2,1468176	3,3857259
TU1	NaOH(aq)	4	0,11	Z_R300_150_P400I_20	5,9089627	16,126606	75,605297	-32,662988	1,4968701	6,7714519
TU1	NaOH(aq)	4	0,02	Z_R300_150_P400I_20	8,4805938	16,644557	77,154989	-32,417272	0,5170741	10,122858
TU1	NaOH(aq)	4	0,1	Z_R300_150_P400I_20	8,9417746	16,891176	77,71603	-30,67915	1,4659134	13,508584
TU1	NaOH(aq)	4	0,41	Z_R300_150_P400I_20	9,6930305	18,346486	74,082657	-37,896178	8,1797935	17,01417
TU1	NaOH(aq)	4	0,6	Z_R300_150_P400I_20	10,084316	20,934621	66,751624	-39,794072	14,847567	20,640136
TU1	NaOH(aq)	4	1,2	Z_R300_150_P400I_20	10,437847	25,914467	59,106142	-18,833051	0,6997074	24,351643
TU1	NaOH(aq)	4	2,2	Z_R300_150_P400I_20						

C160

Titration Source	Solute	Concentration [g/l]	Titration Vol [ml]	Measuring Step Parameter Set	pH	Conductivity [mS/m]	Cell Resistance [KOhm]	ζ [mV]	ζ Stdev	Elapsed Time [min]
TU1	NaOH(aq)	4	0	Z_R300_150_P400I_20	4,6371178	18,167428	76,486113	-43,483034	5,0828294	3,428366
TU1	NaOH(aq)	4	0,18	Z_R300_150_P400I_20	5,643427	17,556109	83,001852	-40,017943	0,9063881	6,8653121
TU1	NaOH(aq)	4	0,02	Z_R300_150_P400I_20	8,5647484	17,289932	85,906257	-41,634773	0,7994178	10,388318
TU1	NaOH(aq)	4	0,11	Z_R300_150_P400I_20	9,041134	17,516383	87,613785	-46,230134	2,7201226	13,979965
TU1	NaOH(aq)	4	0	Z_R300_150_P400I_20	9,7767634	18,971444	72,500495	-53,354502	10,416888	3,3857259
TU1	NaOH(aq)	4	0,8	Z_R300_150_P400I_20	10,189543	21,562422	67,239163	-43,20566	8,0496327	6,805772
TU1	NaOH(aq)	4	1,4	Z_R300_150_P400I_20	10,545033	28,092868	61,89158	-38,481855	2,8502718	10,260138
TU1	NaOH(aq)	4	2,4	Z_R300_150_P400I_20	10,843774	38,535921	56,944203	-40,62141	1,3162504	13,765984
TU1	NaOH(aq)	4	4	Z_R300_150_P400I_20	11,110586	55,811788	52,269365	-45,727889	1,565049	17,35763

A140UV

Titration Source	Solute	Concentration [g/l]	Titration Vol [ml]	Measuring Step Parameter Set	pH	Conductivity [mS/m]	Cell Resistance [KOhm]	ζ [mV]	ζ Stdev	Elapsed Time [min]
TU1	NaOH(aq)	4	0	Z_R300_150_P400I_20	4,6209278	15,563743	62,7456	-34,918294	3,0523123	3,4543661
TU1	NaOH(aq)	4	0,2	Z_R300_150_P400I_20	5,2418203	16,533648	70,924604	-35,597588	1,4297294	6,8744121
TU1	NaOH(aq)	4	0,03	Z_R300_150_P400I_20	8,3906138	16,55504	74,187702	-36,008711	1,3232519	10,259878
TU1	NaOH(aq)	4	0,12	Z_R300_150_P400I_20	8,9396588	16,819976	75,934608	-35,955863	0,3682365	13,645604
TU1	NaOH(aq)	4	0,4	Z_R300_150_P400I_20	9,6085611	17,585356	72,096437	-43,396634	3,0981113	17,13403
TU1	NaOH(aq)	4	0,8	Z_R300_150_P400I_20	10,060037	21,749143	65,261315	-34,451564	9,3359923	20,622716
TU1	NaOH(aq)	4	0,6	Z_R300_150_P400I_20						

B140UV

Titration Source	Solute	Concentration [g/l]	Titration Vol [ml]	Measuring Step Parameter Set	pH	Conductivity [mS/m]	Cell Resistance [KOhm]	ζ [mV]	ζ Stdev	Elapsed Time [min]
TU1	NaOH(aq)	4	0	Z_R300_150_P400I_20	4,5713068	16,845746	86,958952	-48,962956	0,7485645	3,420566
TU1	NaOH(aq)	4	0,07	Z_R300_150_P400I_20	4,8659691	16,333591	96,119018	-51,539448	1,2894111	6,823452
TU1	NaOH(aq)	4	0,05	Z_R300_150_P400I_20	5,1841267	16,726611	101,67125	-51,793477	1,0706034	10,192018
TU1	NaOH(aq)	4	0,04	Z_R300_150_P400I_20	5,6191991	15,310254	104,73508	-51,086679	0,3913722	13,577744
TU1	NaOH(aq)	4	0,04	Z_R300_150_P400I_20	6,0571444	16,757139	106,68896	-51,842327	0,4262749	16,96347
TU1	NaOH(aq)	4	0,04	Z_R300_150_P400I_20	6,5894085	16,859472	107,79043	-52,507388	0,4629427	20,348936
TU1	NaOH(aq)	4	0,04	Z_R300_150_P400I_20	7,2531456	17,107385	107,94319	-52,077065	0,3385359	23,768982
TU1	NaOH(aq)	4	0,04	Z_R300_150_P400I_20	7,7830624	16,371768	108,40721	-51,523852	0,4288277	27,257408
TU1	NaOH(aq)	4	0,03	Z_R300_150_P400I_20	7,9539785	17,459147	105,22788	-51,123709	0,2652455	30,711514
TU1	NaOH(aq)	4	0,03	Z_R300_150_P400I_20	8,7968633	17,78578	103,95319	-51,38942	0,5793775	34,16588
TU1	NaOH(aq)	4	0,27	Z_R300_150_P400I_20	9,4075293	16,750768	93,827817	-56,126307	2,1709072	37,706046
TU1	NaOH(aq)	4	0,4	Z_R300_150_P400I_20	9,7708135	20,276958	84,067426	-51,445726	3,1074277	41,263372
TU1	NaOH(aq)	4	0,8	Z_R300_150_P400I_20	10,421993	29,100891	74,458178	-42,253246	5,9511524	44,906499

C140UV

Titration Source	Solute	Concentration [g/l]	Titration Vol [ml]	Measuring Step Parameter Set	pH	Conductivity [mS/m]	Cell Resistance [KOhm]	ζ [mV]	ζ Stdev	Elapsed Time [min]
TU1	NaOH(aq)	4	0	Z_R300_150_P400I_20	4,706379	16,864692	65,239085	-47,228626	1,4474421	3,437206
TU1	NaOH(aq)	4	0,2	Z_R300_150_P400I_20	6,1416724	16,213092	74,012285	-46,342267	1,5170872	6,840092
TU1	NaOH(aq)	4	0,03	Z_R300_150_P400I_20	8,6178125	16,535128	77,637071	-47,54561	0,4582183	10,225818
TU1	NaOH(aq)	4	0,2	Z_R300_150_P400I_20	9,202861	16,785678	79,561369	-49,03068	0,5139497	13,645864
TU1	NaOH(aq)	4	0,6	Z_R300_150_P400I_20	9,7832319	18,627022	72,631711	-58,606056	8,0763676	17,16887
TU1	NaOH(aq)	4	1	Z_R300_150_P400I_20	10,148658	21,350364	64,247481	-44,006129	8,0752819	20,777416
TU1	NaOH(aq)	4	2	Z_R300_150_P400I_20	10,488933	28,198041	55,350733	-34,854089	6,5218416	24,506083

A160UV

Titration Source	Solute	Concentration [g/l]	Titration Vol [ml]	Measuring Step Parameter Set	pH	Conductivity [mS/m]	Cell Resistance [KOhm]	ζ [mV]	ζ Stdev	Elapsed Time [min]
TU1	NaOH(aq)	4	0	Z_R300_150_P400I_20	4,4562692	16,745974	86,552503	-57,567261	2,7425351	3,436946
TU1	NaOH(aq)	4	0,2	Z_R300_150_P400I_20	6,0998753	16,209842	94,774161	-58,376913	0,8983005	6,805252
TU1	NaOH(aq)	4	0,04	Z_R300_150_P400I_20	7,0180989	16,225038	99,540359	-59,165721	0,4403624	10,208138
TU1	NaOH(aq)	4	0,04	Z_R300_150_P400I_20	7,8227058	16,305628	102,27554	-59,302039	0,7551408	13,593864
TU1	NaOH(aq)	4	0,04	Z_R300_150_P400I_20	8,0670629	16,361626	103,95403	-59,115491	0,5450113	16,97933
TU1	NaOH(aq)	4	0,05	Z_R300_150_P400I_20	8,43304	16,497013	104,40105	-58,44606	0,552408	20,399116
TU1	NaOH(aq)	4	0,09	Z_R300_150_P400I_20	8,7778871	16,689827	103,72546	-57,748794	0,7048701	23,853482
TU1	NaOH(aq)	4	0,31	Z_R300_150_P400I_20	9,4424089	17,58817	96,250416	-62,867549	0,5090504	27,393388
TU1	NaOH(aq)	4	0,4	Z_R300_150_P400I_20	9,881834	19,560579	84,139139	-62,987881	5,9198871	31,053155

B160UV

Titration Source	Solute	Concentration [g/l]	Titration Vol [ml]	Measuring Step Parameter Set	pH	Conductivity [mS/m]	Cell Resistance [KOhm]	ζ [mV]	ζ Stdev	Elapsed Time [min]
TU1	NaOH(aq)	4	0		4,61	16,22	95,03	-45,45		3,4
TU1	NaOH(aq)	4	0,2		6,37	15,46	110,38	-46,01		6,9
TU1	NaOH(aq)	4	0,03		8,59	15,76	114,89	-47,4		10,2
TU1	NaOH(aq)	4	0,16		9,13	16,04	115,81	-48,22		13,7
TU1	NaOH(aq)	4	0,6		9,8	17,9	98,65	-56,18		17,3
			1		10,17	21,45	84,43	-38,49		19,3

C160UV

Titration Source	Solute	Concentration [g/l]	Titration Vol [ml]	Measuring Step Parameter Set	pH	Conductivity [mS/m]	Cell Resistance [KOhm]	ζ [mV]	ζ Stdev	Elapsed Time [min]
TU1	NaOH(aq)	4	0	Z_R300_150_P400I_20	4,5060596	17,030232	69,94578	-49,004245	7,6957887	3,402886
TU1	NaOH(aq)	4	0,2	Z_R300_150_P400I_20	5,1427442	16,970075	79,064406	-51,295328	5,8854405	6,9084721
TU1	NaOH(aq)	4	0,04	Z_R300_150_P400I_20	8,1038784	17,038961	84,247679	-51,333093	2,9934193	10,517278
TU1	NaOH(aq)	4	0	Z_R300_150_P400I_20	9,0097152	17,599668	85,114558	-49,776572	1,565803	3,3857259
TU1	NaOH(aq)	4	0,6	Z_R300_150_P400I_20	9,6822786	19,373316	78,005913	-58,629635	6,9444128	6,857252
TU1	NaOH(aq)	4	0,8	Z_R300_150_P400I_20	10,058424	22,358753	68,815883	-49,31843	6,6921046	10,448638
TU1	NaOH(aq)	4	1,6	Z_R300_150_P400I_20	10,407067	27,928567	60,231566	-28,761573	6,7501203	14,177565

Tour140

Titration Source	Solute	Concentration [g/l]	Titration Vol [ml]	Measuring Step Parameter Set	pH	Conductivity [mS/m]	Cell Resistance [KOhm]	ζ [mV]	ζ Stdev	Elapsed Time [min]
			0		4,31	16,86	48,51	-27,77		3,4
			0,2		5,42	16	53,3	-26,2		6,9
			0,03		6,44	15,97	56,08	-26,74		10,4
			0,03		7,95	15,85	57,86	-25,77		13,9
			0,03		8,38	15,93	58,9	-26,72		17,5
			0,05		8,79	16,07	59,42	-24,99		21,1
			0,26		9,49	16,74	58,33	-27,02		24,8
			0		9,87	19,14	53,95	-35,63		3,5
			0,8		10,21	21,25	51,13	-37,11		7,1
			1,4		10,52	25,31	45,08	-36,9		9

Tour160

Titration Source	Solute	Concentration [g/l]	Titration Vol [ml]	Measuring Step Parameter Set	pH	Conductivity [mS/m]	Cell Resistance [KOhm]	ζ [mV]	ζ Stdev	Elapsed Time [min]
			0,2		4,43	13,29	53,45	-35,96		3,5
			0,02		5,91	14,44	58,25	-32		7,3
TU1	NaOH(aq)	4	0	Z_R300_150_P400I_20	6,4633391	14,188777	68,640767	-33,591743	2,3927714	3,4457833
TU1	NaOH(aq)	4	0,02	Z_R300_150_P400I_20	7,0458738	13,243733	69,810678	-35,06793	0,5381501	6,8309833
TU1	NaOH(aq)	4	0,02	Z_R300_150_P400I_20	7,5076047	15,208218	70,995146	-35,438306	0,7552429	10,2167
TU1	NaOH(aq)	4	0,02	Z_R300_150_P400I_20	7,8229548	14,505041	71,788957	-36,030593	0,5828397	13,6019
TU1	NaOH(aq)	4	0,02	Z_R300_150_P400I_20	8,0303474	15,012637	72,362693	-36,294719	0,9534067	17,02195
TU1	NaOH(aq)	4	0,03	Z_R300_150_P400I_20	8,3191052	15,619148	72,715195	-35,911323	0,8324872	20,45915
TU1	NaOH(aq)	4	0,04	Z_R300_150_P400I_20	8,5826254	14,544515	72,72794	-36,125736	1,4182215	23,913517
TU1	NaOH(aq)	4	0,06	Z_R300_150_P400I_20	8,8416858	15,129787	72,127045	-36,491566	2,0544997	27,385033
TU1	NaOH(aq)	4	0,24	Z_R300_150_P400I_20	9,4527978	16,038716	68,645094	-40,846956	3,017643	30,959517
TU1	NaOH(aq)	4	0,2	Z_R300_150_P400I_20	9,6663235	17,241797	63,290484	-44,785045	5,2884386	34,5509
TU1	NaOH(aq)	4	0,6	Z_R300_150_P400I_20	10,109438	19,747683	57,188559	-30,332177	5,8323421	38,194033
TU1	NaOH(aq)	4	1,4	Z_R300_150_P400I_20	10,471554	24,917413	50,777017	-22,478608	5,7509026	41,85405

C140 Full pH range

Titration Source	Solute	Concentration [g/l]	Titration Vol [ml]	Measuring Step Parameter Set	pH	Conductivity [mS/m]	Cell Resistance [KOhm]	ζ [mV]	ζ Stdev	Elapsed Time [min]
TU2	HCl(aq)	1,823	0,8	Z_R300_150_P400I_20	0,9084169	4990,8666	2,3517976	-585,7996	55,51742	23,751817
TU2	HCl(aq)	1,823	0,4	Z_R300_150_P400I_20	1,4203148	1606,3588	5,8191378	-145,7349	17,542835	20,366083
TU2	HCl(aq)	1,823	0,2	Z_R300_150_P400I_20	1,9746908	444,00676	12,555365	-48,465834	23,613275	16,945267
TU2	HCl(aq)	1,823	0,4	Z_R300_150_P400I_20	2,6989738	89,782309	26,503467	-31,318156	16,082423	13,542383
TU2	HCl(aq)	1,823	0,6	Z_R300_150_P400I_20	3,0451898	47,028055	35,562169	-28,763432	20,829216	10,15665
TU2	HCl(aq)	1,823	0,4	Z_R300_150_P400I_20	3,9663211	17,965226	51,366292	-35,230084	1,0641342	6,7368667
TU2	HCl(aq)	1,823	0	Z_R300_150_P400I_20	4,299379	16,406739	48,484377	-35,062145	2,5327141	3,3857333
					5,1			-48,32		
					9,06			-42,93		
					10,36			-39,58		
					10,77			-26,32		
					11,31			-31,63		
					12,02			-57,01		
TU1	NaOH(aq)	4	0	Z_R300_150_P400I_20	12,96556	3414,9333	2,4291385	365,16333	134,83114	3,4026167

Alfa Laval NF99HF

Titration Source	Solute	Concentration [g/l]	Titration Vol [ml]	Measuring Step Parameter Set	pH	Conductivity [mS/m]	Cell Resistance [KOhm]	ζ [mV]	ζ Stdev	Elapsed Time [min]
TU2	HCl(aq)	1,823	0,2	Z_R300_150_P400I_20	0,8697655	5512,2998	3,5435961	-665,84875	163,1888	23,826915
TU2	HCl(aq)	1,823	0,6	Z_R300_150_P400I_20	2,0715681	369,41393	43,693713	-3,5436811	7,9556675	20,390536
TU2	HCl(aq)	1,823	0,4	Z_R300_150_P400I_20	2,6967129	99,246645	154,56692	0,3401947	5,9755931	16,94501
TU2	HCl(aq)	1,823	0,6	Z_R300_150_P400I_20	3,397096	30,553257	428,22826	-19,963366	0,5822486	13,499484
TU2	HCl(aq)	1,823	0,6	Z_R300_150_P400I_20	3,8684446	20,223157	597,36208	-36,862079	0,203183	10,088278
TU2	HCl(aq)	1,823	0,28	Z_R300_150_P400I_20	4,2246864	17,062109	647,68127	-50,146105	0,1957572	6,7371318
TU1	NaOH(aq)	4	0	Z_R300_150_P400I_20	4,7830316	15,470886	823,48061	-57,176141	0,2604234	3,3859859
TU1	NaOH(aq)	4	0,05	Z_R300_150_P400I_20	5,1059426	14,884616	857,71815	-62,771089	0,6148471	6,814612
TU1	NaOH(aq)	4	0,03	Z_R300_150_P400I_20	5,6688994	14,762602	875,29788	-71,093507	0,8152278	10,217498
TU1	NaOH(aq)	4	0,03	Z_R300_150_P400I_20	7,6441045	15,365103	876,42337	-86,790625	0,1858399	13,620384
TU1	NaOH(aq)	4	0,03	Z_R300_150_P400I_20	8,3128927	14,833795	869,49642	-89,204184	0,3139015	16,98895
TU1	NaOH(aq)	4	0,04	Z_R300_150_P400I_20	8,6435823	14,734481	866,5611	-90,039389	0,388363	20,357516
TU1	NaOH(aq)	4	0,07	Z_R300_150_P400I_20	8,9586698	14,663621	858,62442	-90,672594	0,592727	23,708922
TU1	NaOH(aq)	4	0,23	Z_R300_150_P400I_20	10,328989	23,491378	655,93528	-89,831982	0,5214202	27,120388
TU1	NaOH(aq)	4	0,4	Z_R300_150_P400I_20	10,823185	40,82993	425,91719	-84,857275	0,9850325	30,540174
TU1	NaOH(aq)	4	1,2	Z_R300_150_P400I_20	11,362975	87,447658	209,43011	-75,42527	2,3105024	33,95974
TU1	NaOH(aq)	4	0,8	Z_R300_150_P400I_20	12,008508	318,77718	65,888267	-58,133004	5,9467453	37,396946

Alfa Laval NFT50

Titration Source	Solute	Concentration [g/l]	Titration Vol [ml]	Measuring Step Parameter Set	pH	Conductivity [mS/m]	Cell Resistance [KOhm]	ζ [mV]	ζ Stdev	Elapsed Time [min]
TU2	HCl(aq)	1,823	0,4	Z_R300_150_P400I_20	0,9266534	4836,1613	3,7175155	-446,55869	19,889328	27,428228
TU2	HCl(aq)	1,823	0,4	Z_R300_150_P400I_20	1,7315265	819,34538	18,632761	-30,577994	12,771054	23,965542
TU2	HCl(aq)	1,823	1,2	Z_R300_150_P400I_20	2,2986357	227,01938	60,320415	-6,7647293	14,259422	20,485436
TU2	HCl(aq)	1,823	0,02	Z_R300_150_P400I_20	3,1533718	42,435814	259,80342	-13,866485	3,7466165	17,01391
TU2	HCl(aq)	1,823	0,04	Z_R300_150_P400I_20	5,2108888	15,626433	582,59788	-23,09753	0,7322163	13,534064
TU2	HCl(aq)	1,823	0,04	Z_R300_150_P400I_20	5,8578275	15,444583	567,00245	-23,834857	0,5281404	10,131178
TU2	HCl(aq)	1,823	0,05	Z_R300_150_P400I_20	7,0418426	15,342852	541,39942	-24,094821	0,4399035	6,7626119
TU2	HCl(aq)	1,823	0	Z_R300_150_P400I_20	8,3175495	15,411974	516,47055	-23,510339	0,6973967	3,411206
TU1	NaOH(aq)	4	0,07	Z_R300_150_P400I_20	8,5970138	14,501606	534,97337	-29,631859	0,4582606	6,7714519
TU1	NaOH(aq)	4	0,05	Z_R300_150_P400I_20	8,8897787	13,159386	529,51205	-30,252183	0,4282937	10,122858
TU1	NaOH(aq)	4	0,23	Z_R300_150_P400I_20	9,439816	11,50556	512,00848	-30,543111	0,5099736	13,508584
TU1	NaOH(aq)	4	0,4	Z_R300_150_P400I_20	9,7929531	10,711672	484,67748	-30,777921	0,337353	16,95437
TU1	NaOH(aq)	4	0,8	Z_R300_150_P400I_20	10,101385	16,770353	441,79297	-30,951953	0,4075507	20,382996
TU1	NaOH(aq)	4	0,8	Z_R300_150_P400I_20	10,698468	23,06948	314,78522	-29,845773	0,6269553	23,820202
TU1	NaOH(aq)	4	0,4	Z_R300_150_P400I_20	11,268297	73,858237	162,30906	-26,927548	2,6806621	27,257408
TU1	NaOH(aq)	4	0,6	Z_R300_150_P400I_20	12,048084	309,87058	57,67225	7,7078354	33,178551	30,754414

Permeance test 1

	Measurement:	1	2	3	4	5	6	7	8
	Performed:	13-05-16 23:30	14-05-16 11:40	15-05-16 11:40	15-05-16 23:15	16-05-16 11:35	16-05-16 23:15	17-05-16 11:40	17-05-16 23:15
1	T	8,8504	8,78	8,623	8,5537	8,4576	8,4059	8,3357	8,274
2	T 2	8,2234	8,1584	8,0211	7,9554	7,8564	7,7981	7,7254	7,6647
3	T 140	8,3847	8,317	8,1796	8,1206	8,0466	7,9904	7,9263	7,8723
4	T 140 2	8,9803	8,9144	8,7435	8,6622	8,5554	8,4761	8,3938	8,3764
5	T 160	8,4624	8,371	8,2145	8,1446	8,0614	7,9969	7,9257	7,8665
6	T 160 2	8,9434	8,8667	8,7069	8,6387	8,5504	8,4805	8,4053	8,3432
7	A 140	8,5774	8,5015	8,3107	8,2407	8,1547	8,0898	8,0163	7,9595
8	A 140 2	8,74	8,6666	8,5159	8,4455	8,367	8,301	8,2287	8,164
9	A 160	9,0954	9,0246	8,8662	8,7857	8,6917	8,6212	8,547	8,4794
10	A 160 2	9,2928	9,2163	9,0395	8,9613	8,8651	8,7868	8,6872	8,6219
11	B 140	9,636	9,5643	9,4019	9,3261	9,2255	9,1446	9,0473	8,984
12	B 140 2	9,3553	9,2444	9,0291	8,9592	8,8746	8,8006	8,7274	8,6624
13	B 160	8,8848	8,8077	8,6484	8,5722	8,4912	8,438	8,382	8,316
14	B 160 2	9,2812	9,2006	9,0296	8,9446	8,852	8,7752	8,6951	8,6267
15	C 140	8,6605	8,59	8,4484	8,3758	8,3012	8,2407	8,1722	8,1112
16	C 140 2	9,1597	9,0753	8,8999	8,8156	8,7298	8,6567	8,5671	8,4965
17	C 160	9,0175	8,9473	8,7973	8,7154	8,6056	8,5206	8,4253	8,3537
18	C160 2	9,5388	9,4286	9,1605	9,066	8,9657	8,8786	8,7727	8,6848
19	Open 1	8,8567	8,7737	8,6038	8,5225	8,4412	8,3675	8,2873	8,2234
20	Open 2	9,4366	9,3371	9,1343	9,0424	8,9472	8,8668	8,7734	8,6967

Permeance test 2

		Measurement	Start (20/5 21:30)	21-05-2016 10:45	21-05-2016 21:40	22-05-2016 13:00	22-05-2016 21:30
		Substance	0	13,25	24,1667	39,5	48
1	C140	Ethanol	15,4261	15,2416	15,0872	14,8756	14,7595
2	Tour 140	Ethanol	14,5525	14,3852	14,25	14,0645	13,9637
3	Tour	Ethanol	13,3918	13,2558	13,1391	12,9748	12,8864
4	Open 1	Ethanol	15,3728	14,9081	14,5268	14,0352	13,7684
5	C140	Hexan	13,0226	12,9204	12,8043	12,678	12,5981
6	Tour 140	Hexan	12,78	12,7696	12,7546	12,7418	12,7449
7	Tour	Hexan	12,9672	12,847	12,7138	12,5772	12,4822
8	Open 2	Hexan	13,15	11,6764	10,6767	9,4017	8,7664

Permeance test 3:

		Measurement:	1	2	3	4	5	6	7	8	9
		Date:	29-05	30-05	31-05	01-06	01-06	02-06	02-06	03-06	04-06
		Time:	21:40	19:35	13:05	00:07	14:25	00:10	15:00	13:37	20:15
Water	1	NF99HF	19,8738	19,7776	19,6986	19,6371	19,5571	19,5047	19,4225	19,2961	19,1082
Water	2	NFT50	19,2894	19,1791	19,0822	19,0286	18,952	18,9001	18,8217	18,6983	18,5263
Water	3	A140	19,9253	19,751	19,6041	19,5097	19,3951	19,3081	19,1857	19,0067	18,7351
Water	4	Open	20,3586	20,1238	19,91391	19,7961	19,624	19,5094	19,3469	19,1249	18,7779
Ethanol	5	NF99HF	17,7782	17,1603	16,6429	16,4631	16,1963	16,0237	15,7748	15,4108	14,9312
Ethanol	6	NFT50	17,5696	17,1446	16,8285	16,6266	16,3866	16,2437	16,0049	15,695	15,3355
Ethanol	7	A140	17,3576	17,1129	16,9534	16,8397	16,7316	16,6624	16,5522	16,4051	16,2176
Ethanol	8	Open	18,1596	16,993	16,2116	15,7782	15,2124	14,8805	14,3694	13,7784	13,0104
Hexane	9	NF99HF	16,9079	16,187	15,6148	15,2316	14,782	14,4524	13,952	13,254	12,2602
Hexane	10	NFT50	16,1211	15,9666	15,858	15,7176	15,6445	15,5572	15,4707	15,3577	15,1989
Hexane	11	A140	16,1866	16,0548	15,8644	15,6978	15,574	15,4779	15,401	15,209	14,9446
Hexane	12	Open	15,5215	13,2179	11,7999	11,0445					

A.7 DSA measurements

A140

Water	Diiodom.
52,8	26,5
50,9	28,7
44,5	23,8
45,5	27,6
46,8	31,8

Water UV Measurements

UV-A 1h	UV-C 5m.	UV-C 10m.	UV-C 15m.	UV-C 30m.
58	36,8	28,1	22,9	21,5
57	32	23,8	23,6	18,2
55,5	33,5	26,5	23,5	19,8
	33,1	25,8	20,8	20,9
	35,3	27,4	24,1	18,5

B140

Water	Diiodom.
49	31,6
48,8	29,1
54,3	35,9
55,7	30,6
52,1	32,2

Water UV Measurements

UV-A 1h	UV-C 5m.	UV-C 10m.	UV-C 15m.	UV-C 30m.
	40,2	32,4	26,7	21,8
	41,7	29,2	25,2	22,2
	38,1	27,7	22,5	23,7
	36,9	28,5	24,4	21,3
	39,9	29,7	25,8	20,9

C140

Water	Diiodom.
58,5	29,2
57,7	25,9
56,7	23,2
54,9	22,1
53,2	27,6

Water UV Measurements

UV-A 1h	UV-C 5m.	UV-C 10m.	UV-C 15m.	UV-C 30m.
67,1	54,6	48,1	37	25,9
64,4	55,8	51	36,4	23,6
63,4	55,9	46	35,1	19,9
66,3	55,6	48,9	29,5	18,9
	53,4	46,1	28,8	20,8

NF99HF

Water	Diiodom.
20,2	64,4
18,8	62,2
20,1	65,8
20,2	61,4
19,8	64,7

NFT50

Water	Diiodom.
24,4	62,7
23,2	61,1
24,1	57,9
26,8	62,1
26,5	60,4

Tour 160

Water	Diiodom.
90,2	39,2
89,1	37,7
87,8	34,3
86,8	39,2
90,1	35,7

Tour 140

Water	Diiodom.
58,6	39,6
53,2	40,4
56,2	34,9
49,6	38,6
47,2	39,7

A 160

Water	Diiodom.
82,3	34,6
77,6	26,7
80,6	28,5
79,9	29,7
73,9	24,9

Water UV Measurements

UV-C 5m.	UV-C 10m.	UV-C 15m.	UV-C 30m.
62	24,1	22,1	20,9
64,3	25,1	20,9	24,1
62,8	26,7	26,2	19,2
60,9	22,4	22,7	18,9
63,1	21,7	23,5	21,1

B 160

Water	Diiodom.
78	27,3
80,6	29,2
81,8	27,6
82,6	31,3
80,9	30,1

Water UV Measurements

UV-C 5m.	UV-C 10m.	UV-C 15m.	UV-C 30m.
77,6	64,9	57,1	36,4
78	67,6	56,2	40
76,1	66,3	59,8	36,4
78,3	64,6	61,4	35,4
79,1	65,5	61,3	33,1

C 160

Water	Diiodom.
89,9	27,3
83,3	29,2
87,6	27,6
86,3	31,3
86,3	30,1

Water UV Measurements

UV-C 5m.	UV-C 10m.	UV-C 15m.	UV-C 30m.
78,8	47,3	40,7	40
77,9	50,1	39,5	39,6
77,1	50,5	45,1	43,5
76,8	56,8	44,4	46,9
79,1	57,6	44,6	42,3

B140 Ramp after UV

5 min	10 min	15 min	30 min	45 min	60 min
30,2	47,4	43,6	46,1	46,8	49,2
34,6	42,9	45,7	44,8	47,1	48,9
38,8	46,8	44,9	46,3	46,4	51
37,4	42,5	47,1	47,1	48,6	52,2
35,2	45,4	45	48,4	48,9	50,4